UNIVERSITÀ
DEGLI STUDI
FIRENZE

DOTTORATO DI RICERCA IN
Ingegneria Industriale

CICLO XXX

Andrea Guerrini

Protein-based multifunctional magnetic nanoparticles for theranostic applications

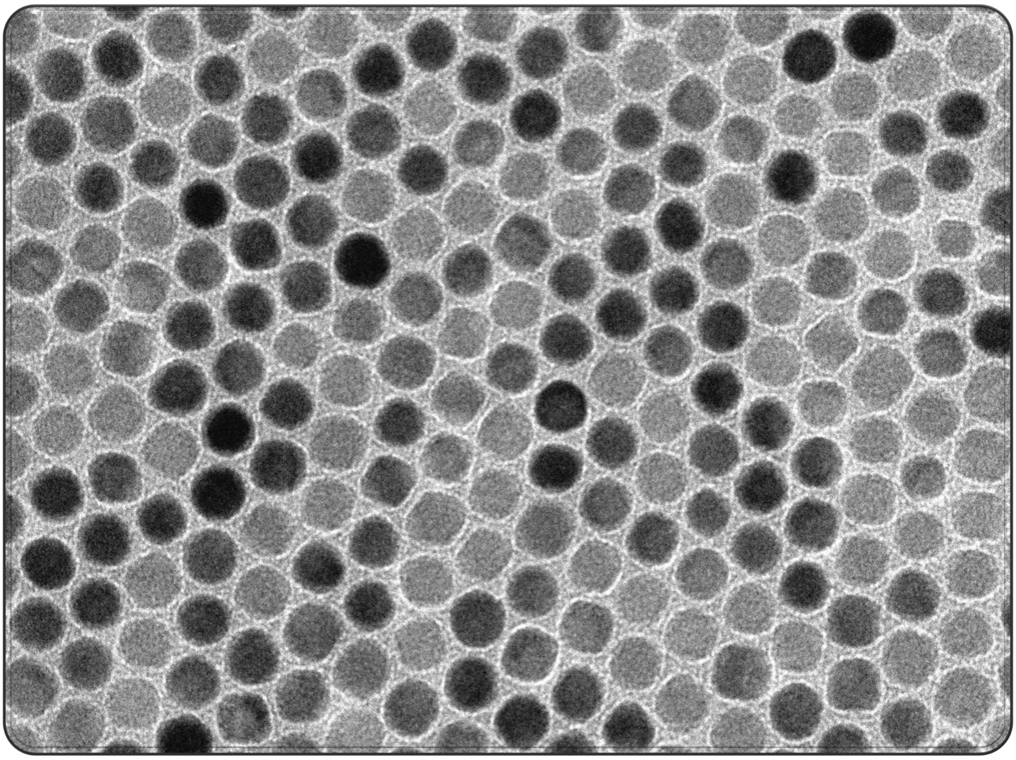

UNIVERSITÀ
DEGLI STUDI
FIRENZE

DOTTORATO DI RICERCA IN
Ingegneria Industriale

CICLO XXX

COORDINATORE Prof. Maurizio De Lucia

Protein-based multifunctional magnetic nanoparticles for theranostic applications

Settore Scientifico Disciplinare CHIM/03

Dottorando
Dott. *Guerrini Andrea*

(firma)

Tutore
Prof. Caneschi *Andrea*

(firma)

Co-Tutore
Dr. *Sangregorio Claudio*

(firma)

Coordinatore
Prof. *De Lucia Maurizio*

(firma)

Anni 2014/2017

“Gli uomini sono artefici del proprio destino:
possono commettere sempre gli stessi errori,
possono fuggire costantemente da ciò che
desiderano, e che magari la vita offre loro in modo
generoso; oppure possono abbandonarsi al destino
e lottare per i propri sogni accettando il fatto che si
presentano sempre nel momento giusto.”

1. Introduction

In recent decades nano-sciences have polarized the attention of researchers, thanks to their potential of innovation that can be applied in many scientific and technological field of knowledge[1–6]. Particles with at least one dimension less than 100 nm in the form of nanoparticles (NPs), nanofibers and nanocomposites, indeed find application in electronics, biotechnology, medical sciences and many other technological fields. Products of this innovation are already available on the market or shortly will be, improving the quality of our life. When reduced to the nano-scale, indeed, materials may reveal attractive and unexpected properties, different from those of the bulk counterparts, which can be exploited to realize new or better materials[7]; in particular, in medical science nanomaterials are expected to have a large potential to create products able to increase specificity, accuracy and efficacy of diagnosis and treatment of diseases[8].

In particular, among the others, magnetic nanoparticles (MNPs) represent one of the most promising materials for biomedical application, thanks to their unique properties[9]. First of all, they share in common with all the NPs two important characteristics: they have a size comparable to that of many biological entities of interest as protein, DNA, and cell organelles; they have high surface area and large surface-to-volume ratio due to their nanometric size, which assure the possibility to maximize the interaction with other elements. However unlike other kind of nanometric materials, MNPs possess the unique properties of superparamagnetic behaviour[10]. When the size of ferro- or ferrimagnetic particles is lower than a critical size $\mathrm{d_c}$ which depending on the type of material varies between tens to few hundreds of nanometers, they become single domain, i.e. the formation of magnetic domains is no longer energetically favoured, so that they are characterized by a single magnetic moment given by the sum of all the spins included in the NP. This magnetic moment will freely fluctuate like in a paramagnet (superparamagnetism) or will be blocked along certain favoured crystallographic directions (ferromagnetic-like behaviour) depending on whether the thermal energy is larger or smaller than the energy barrier separating these directions. This energy barrier is determined by the magnetic anisotropy of the material itself and, as a first approximation, is proportional to the volume of the MNPs.

MNPs find[11] application in biomedicine both in the diagnosis, as magnetic resonance imaging contrast enhancement agent[12], and in the therapy as drug delivery (DD) carrier[13] as heat mediator in magnetic fluid hyperthermia (MFH)[8,14]. They also find large application in biotechnology where thanks to their properties they are used in high efficiency detection and removal devices, in immunoassay tests, for cells or proteins purification and separation, water or biological fluids detoxification[13,15–19]. Since applications in medicine requires that the use of a biocompatible materials, iron oxides are to the date the mostly investigated MNPs; in particular, in the family of iron oxide magnetite, $\mathrm{Fe_3O_4}$ and maghemite, $\gamma \cdot \mathrm{Fe_2O_3}$, which can potentially follow endogenous pathways of degradation and be reused by the body, have the best magnetic properties.

The most fascinating characteristic of MNPs for application in biomedicine is the unique combination of the moving, sensing and heating capabilities in a single element. Indeed, MNPs offer:

- the possibility to control remotely the MNPs using a static magnetic field (SMF) gradient;
- the ability of the magnetic moment of MNPs to interact with nearby nuclear spin of water protons, modifying their relaxation rate in magnetic resonance imaging (MRI) analysis;
- the capability to release heat when exposed to an Alternating Magnetic Field (AMF) of the right frequency and intensity.

The first characteristic allows the separation from a biological fluid of an element (protein, DNA, heavy metal, pathogen, bacteria, etc.) bound to the MNPs, by simple application of a permanent magnet, for analytical tests or for blood purification. The surface of the MNPs indeed can be functionalized to react specifically with an element, for instance a bacterial antibody, so that MNPs they can selectively bind only this pathogen, allowing its separation from the rest of the mixture by means of an SMF as described in Figure 1.1. Furthermore, as shown in Figure 1.2, using a specific SMF gradient it is possible to concentrate MNPs in a target area near the surface of a body and, for example, transport a drug bound to the nano-device with greater precision than common systemic drug administration, reducing the amount of drugs required for the treatment. In the same way it is possible to deliver bioengineered magnetic scaffolds for tissue repair[20].

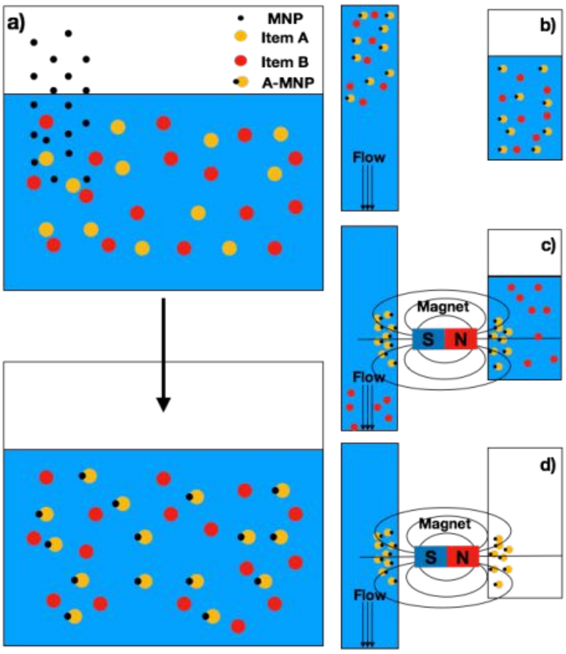

Figure 1.1: a) MNPs mixed into a solution bind specifically one of the component; b) the mixture reacted can be put into a becker or in a continuos flow; c) a strong SMF gradient attracts the MNPs, d) separation from the mixture.

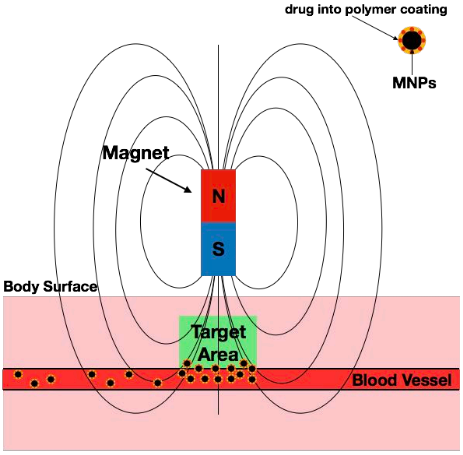

Figure 1.2: MNPs with drug bound onto their surface coating, flows into the blood vessels and concentrate into a target area where a strong SMF gradient is applied.

The second feature can be used to overcome one of the limits associated with the use of MRI technique. Indeed, even if MRI is widely used in medical clinic to investigate the anatomy and physiology of the body, often a contrast agent (CA) is needed to increase the natural contrast between healthy and pathological tissues, like tumour lesions, oedema, soft tissue damages and so on. As a matter of fact, MRI provides images of the density distribution of protons or other nuclei through the application of appropriate magnetic field gradients and radiofrequency pulse sequences[21]. When the pulse is applied the proton spin magnetization, *m* rotates and then relaxes back to the equilibrium values with two typical relaxation times, called T_1 and T_2, as shown in Figure 1.3. MRI exploits the contrast created by different nuclear spin-lattice (T_1) and spin-spin (T_2) relaxation times which characterizes water protons of molecules contained in different tissues to visualize the interior of the body. When the natural image contrast is not enough to highlight the presence of the diseased tissue, it is necessary to use a CA that induces variation of either T_1 or T_2 or both. CA are usually classified into two groups: those that increase the longitudinal relaxation rate, $\mathrm{R}_1 = 1 / \mathrm{T}_1$ and those that increase the transverse relaxation rate, $R_2 = 1 / T_2$. T_1 agents are called positive CAs since their effect leads to an increase of the intensity of the signal (brighter region) in the areas where they are located. Conversely, T_2 agents are defined as negative CAs, as they cause a reduction in the intensity of the signal (darker region) in areas where they accumulate, Figure 1.4. The paramagnetic metal complexes belonging to the lanthanide family (Gd, Dy, Tb) are the principal representatives of T_1 agents, while superparamagnetic iron oxide MNPs are the best example of T_2 agents.

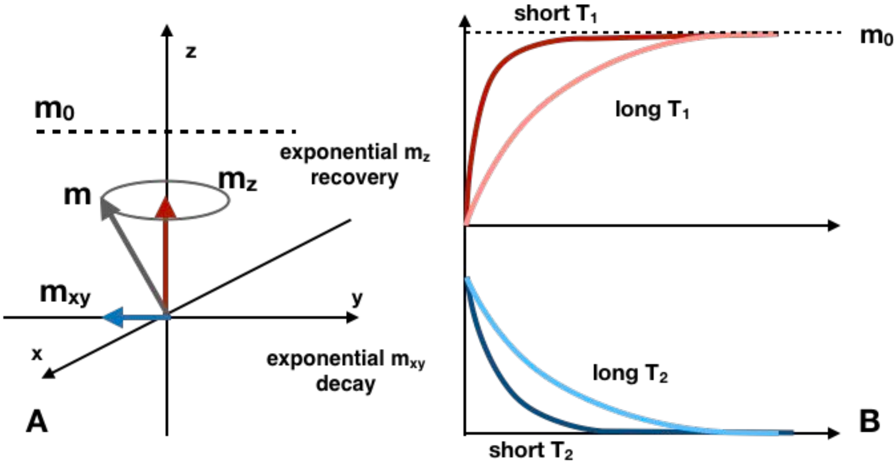

Figure 1.3: a) Relaxation of a magnetic moment, m, of a proton nuclear spin after a RF pulse; The in plane component, m_{xy}, vanishes with a characteristic time T_2, while m recovers its initial value along the static filed, m_z with a characteristic time T_1 b) Relaxation time of longitudinal (upper panel) and transversal (lower panel) magnetizations after the RF pulse, different local environments influence the time at which the magnetization recover the initial value. The darker lines show the effect of a paramagnetic or superparamagnetic centre on the water proton spins (shortening of the relaxation times).

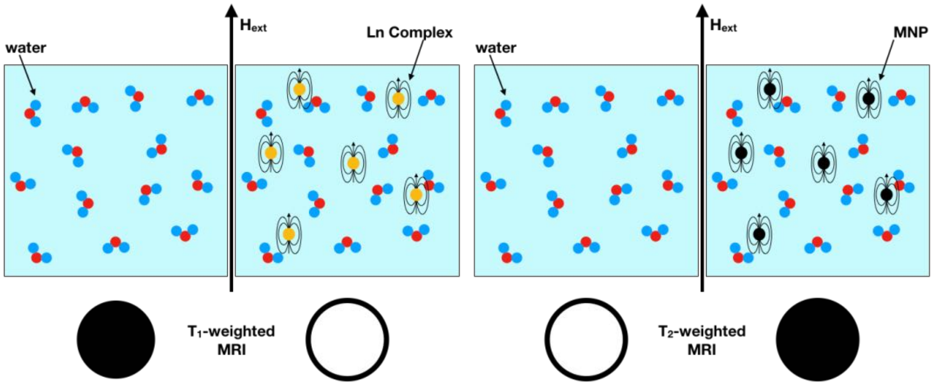

Figure 1.4: Different action of positive (left) and negative (right) CAs on T1 and T2 weighted MRI.

CAs based on dextran coated assembly of superparamagnetic Iron Oxides nanoparticles with a total average diameter between 20 and 150 nm are also commercially available. In Table 1.1, some examples of clinically approved CA for MRI are reported[22].

Commercial name	Generic Name	MRI Target
Feridex® *, Endorem®	Ferumoxides	Liver, Spleen
Resovist®	Ferucarbotran	Liver
Sinerem™, Combidex® *	Ferumoxtran-10	Limph node methastases
Lumirem®, GastroMARK® *	Ferumoxil	Bowel
Feraheme® *	Ferumoxitol	Vasculature

Table 1.1: Iron Oxide (Fe_2O_3) based MNPs available as CAs in MRI; (*Approved by FDA)[23,24]

Last but not least MNPs can be used as heat mediators in hyperthermic treatments of tumours, i.e. when irradiated by an AMF of proper frequency and amplitude dissipate the energy accumulated in the reversal of the magnetization as heat. Hyperthermia treatments take inspiration from ancient wisdom of empirical evidences about fever hyperthermia[25], while it is ca. 150 years ago that Busch first reported experimental evidences that tumours cease to grow when subjected to temperature above 42 °C whilst healthy tissues are not affected by such temperatures[26].

In order to better understand the principle of hyperthermia treatment, we must point out that unlike healthy tissues, the neoplastic ones are characterized by an irregular and chaotic vasculature. Tumour cells overexpress growth factors that stimulate the creation of new blood vessels, preventing the organization of a bloodstream as ordered as in healthy tissues, which often induces stagnation of blood. This pathological condition causes is tumours hypoxia, low pH and inability of dissipating heat efficiently, making them more susceptible to thermal damages[25]. As a further consequence, the endothelial cells of pathological blood vessels do not form tight junction but have fenestrations that allow plasma to invade and be restrained in the extracellular matrix. As a consequence objects with size less than 200 nm can cross the vascular fenestrations and accumulate at the tumour site, thus allowing a natural passive targeting of the MNPs. This effect is referred as Enhanced permeability and Retention effect (EPR).

Hyperthermic treatment are commonly based on the local application of microwaves, radio-waves either with or without magnetic needles implanted into the target site, often associate with therapies involving ionizing radiation[27]. Disadvantages of these strategies are the undesired side-effects such as ionization of genetic material (radiation), lack of selectiveness (microwaves and radio-waves), that affect the surrounding healthy tissues and invasiveness (use of antennas). Although they have successfully been applied to destroy malignant tissues effectiveness of treatments is rather limited.

MFH in principle allow selective heating by localization of the heating source (MNPs) into the tumour tissue and induction of heat release by application of an external AMF. In MFH therapy, MNPs are delivered near or inside the tumor cells and, depending on the temperature reached, it is possible to cause an irreversible cell damage without tissue necrosis (41-46°C) or the complete necrosis of the tumor by thermoablation (more than 46°C, up to 56°C)[28,29]. It has been also demonstrated that, in the case of moderate temperature increase (41-43°C), the hyperthermia treatment enhances the effect of conventional therapies, as chemotherapy or radiotherapy[30]. This represents a significant improvement of tumour therapy compared to the previously described heating techniques. The first application of MFH dates back to 70 years ago when Gilchrist et al.[31] presented an experimental work on MFH: they resected lymph nodes of a dog and heated up *ex vivo* by application of an AMF to iron oxide micro-particles injected into the tumour. More recently, Jordan et al. demonstrated the feasibility of MFH in clinical *in vivo* trials of MFH treatment in patient suffering glioblastoma[32] and prostate cancer[33,34]. They used a combination of radiotherapy and heating produced by 12 nm amino-silane coated Fe_3O_4 MNPs directly injected into the tumour mass at high doses (ca. 50 mg/cm^3); as major result they found no systemic toxicity, long and high MNPs retention into the tumour tissues and small but significant increase of the expectation of life with slightly and temporally morbidity.[33,35]

The attractiveness of MFH treatment relies in its potential for greater selectivity and effectiveness and reduced side-effects compared to common hyperthermia techniques. An additional advantage of using MNPs is the possibility to exploit them as diagnostic and therapeutic agents simultaneously, with a theranostic approach. Nevertheless, there are still several issues that need to be addressed to exploit all the potentialities offered by this approach.

On one hand, MNPs used to date have poor magnetic properties and, consequently, also poor ability to release heat and to enhance contrast in MRI images. However, nowadays chemists have developed different techniques which allow the production of MNPs with much improved characteristic. On the other hand, a major drawback is represented by the stability of MNPs in the human body. In this context, as well described by M. Ferrari in the review "Cancer nanotechnology: opportunities and challenges"[36], and in his following works[37], one of the open issues is the understanding of the bio-distribution mechanisms of MNPs, in order to develop effective strategies to overcome the many physiological barriers to reach the target. For efficiently designing and realizing a nano-device with the best performance and multiple features, it is in fact important to be able to deliver it to the specific place of interest.

In particular, some of main barriers to be overcome are:

- the biological filters such liver, spleen and kidney;
- the reticulo-endothelial system;
- the abnormal flow of blood, which can hamper MPNs to reach the target;
- the increased osmotic pressure within cancer lesion;
- the extracellular matrix;
- the membranes of cells and nuclei.

A crucial element for approaching all the limitations imposed by the human physiology is the surface coating of MNPs. Indeed, the coating determines the interaction of MNPs with the cell and all the elements of the physiological environment, and, at end, it is the mean to equip the MNPs with multiple functionalities. The main goal of the surface coating is to protect the magnetic core from degradation while preserving its properties over time. At the same time, it must allow overcoming the physiological barriers and disguising from the immune system defences. Poly Ethylene Glycol (PEG), for instance, is well known significantly increasing the half-life circulation time by shielding MNPs from RES captures[38,39].

As shown in Figure 1.5, a medical nano-device based on MNPs is designed to be firstly covered by a polymer or molecule to isolate it from the outer environment. As a second step, a wide variety of molecules and polymers, that enrich MNP's ability and functionality, can be grafted on the coating layer. To track bio-diffusion and nano-device's fate, many different tracers can be linked to the coating, such as radioactive atoms, fluorescent dye, CAs molecule for Positron Emission Tomography (PET), or Single Photon Computed Tomography (SPECT)[40,41]. Targeting agent as peptide, aptamer, antibody and protein can also be added to selectively target the diseased tissue[40], while pH-sensitive polymer can modify the MNPs stability once in the acid environment of tumour tissues[42]. Drugs can be loaded into the polymer coating or grafted onto it, and delivered to the target[13,40]; while nucleic acid, Tumour-Associated Antigens, and Tumour-Associated Carbohydrate Antigens can be released for immunotherapy treatment[43].

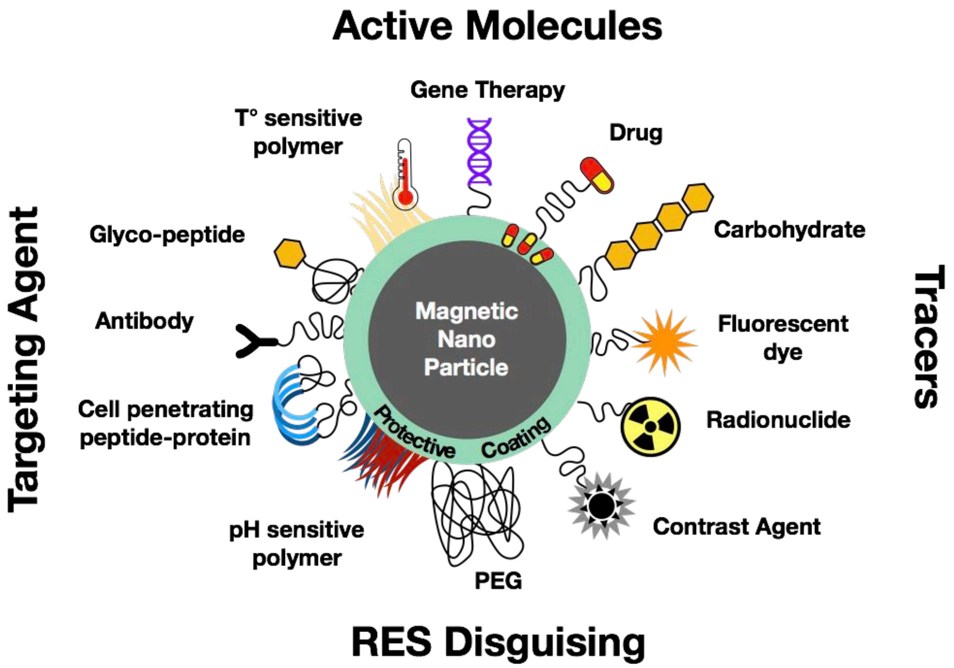

Figure 1.5: Sketch of different functionalities that can be implemented into a MNP-based device

This thesis moves in this complex scenario, the main target being the synthesis and characterization of a protein-based multifunctional MNPs for simultaneous early diagnosis and therapy of cancer (theranostic approach[44]). To realize this goal we coupled a MNP with tailored physical properties for use as heating agent in magnetic fluid hyperthermia and contrast agent for diagnostic imaging, to the shell of human ferritins (Fn), in order to exploit the multiple advantages provided by this endogenous protein, included the possibility of using it as selective drug carrier towards tumor cells.

Human ferritin is a highly symmetrical ubiquitary protein consisting of 24 subunits that self-assemble into a shell-like sphere, with external and internal diameters of 12 and 8 nm, respectively, enclosing a hollow cavity used for storing iron. The choice of Fn to build up a nano-system for theranostic applications is based on the many appealing features this endogenous protein possesses. First Fn is fully biocompatible and it does not activate the immune-inflammatory response, avoiding many of the physiological barrier previously cited. Furthermore HFn can provide a targeting function, as many cancer cell lines over-express the transferrin membrane receptor TfR1. TfR1 recognizes the H ferritin sub-unit causing its internalization within the tumour cell. Moreover, the external surface of ferritin can be easily functionalized with specific targeting agent or drugs, both by genetic recombination and chemical reaction on the numerous thiol and amine residues of cysteine, lysine and glycine. Finally, the hollow cavity of HFn can be filled with drugs, such as doxorubicin by simple self-assembly techniques.

For the realization of the MNP – HFn system we first synthesized magnetite MNPs by thermal decomposition of a metal-organic precursor, iron acetylacetonate, in high boiling solvent. Several attempts were performed in order to obtain highly crystalline, pure magnetite MNPs with a size in the 12-15 nm range. This particular size corresponds to the best compromise between a large heating efficiency in magnetic fluid hyperthermia and colloidal stability. HFns were then conjugated to the inorganic nanoparticles through a heterobifunctional linker, properly chosen to react selectively with thiol functional groups.

In vitro and preliminary *in vivo* studies were carried out on selected tumor cell lines (MDA-MB231, PC3) to assess bio-distribution, toxicity and genotoxicity of the nano-system. Antitumor hyperthermic efficacy was also evaluated by checking cancer cell viability after incubation with MNP-HFn and application of an alternating magnetic field of frequency and amplitude similar to those used in clinical treatment. The relaxometric properties were also measured to verify the capability of the nano-system to act as CA in MRI analysis. Finally, we investigated the possibility of using the HFn cavity as carrier for a cytotoxic drug, doxorubicin. Overall, the obtained results show that the MNP-HFn system is a highly promising platform for theranostic application. In fact, we demonstrated that MNP-HFn has a very good biocompatibility and high stability in physiological media, and, most importantly, it is an efficient heat mediator for MFH both in vitro and in vivo and it enhances the contrast in MRI images.

This thesis is organized as follows: in the first chapter the synthesis by thermal decomposition of MNPs and their characterization is presented. This part of the work was aimed at identifying the synthesis conditions to obtain MNPs with optimal physical and chemical characteristic for use in nanomedicine. In Chapter 3 we will present the investigation on the efficiency of MNP-HFn in releasing heat under the AMF action, and in increasing the relaxation rate of nuclear spin in MRI. The synthesis and characterization of the protein-inorganic hybrid system is described in Chapter 4. The antitumor efficacy of MNP-HFn in MFH therapies will be addressed in Chapter 5 in both in vitro and in vivo experiments. Chapter 6 describes a preliminary study on the drug carrier potential of MNP-HFn. In fact, we have verified the possibility of increasing its antitumor activity including a chemotherapeutic drug, doxorubicin, into the ferritin cavity. The analysis of the results obtained, the future perspectives and the issues to be overcome for utilization of MNP-HFn in clinic are presented in Chapter 7. Finally in Chapter 8, the experimental procedures and the instrumentation used in this work are described.

1. Menini, L. Pereira, M. C.; Parreira, L. A.; Fabris, J. D.; Gusevskaya, E. V. J. Catal. 254, 355 (2008).
2. Santos, P. T. A.; Costa, A. C. F. M.; Kiminami, R. H. G. A.; Andrade, H. M. C.; Lira, H. L.; Gama, L. . J. Alloy. Compd. 483, 399 (2009).
3. Maier-Hauff, K. Ulrich, F.; Nestler, D.; Niehoff, H.; Wust, P.; Thiesen, B.; Orawa, H.; Budach, V.; Jordan, A. J. Oncol. 103, 317 (2011).
4. Lekshmi, I. C. Buonsanti, R.; Nobile, C.; Rinaldi, R.; Cozzoli, P. D.; Maruccio, G. ,. ACSNano 5, 1731 (2011).
5. Challa, S. S. R. K. . Faruq, M. Adv. Drug Deliv. Rev. 63, 789 (2011).
6. Takafuji, M. Ide, S.; Ihara, H.; Xu, Z. Chem. Mater. 16, 1997 (2014).
7. Cao, G. Nanostructures & Nanomaterials. (2003).
8. Pankhurst, Q. A., Connolly, J., Jones, S. K. & Dobson, J. Applications of magnetic nanoparticles in biomedicine. 36, (2003).
9. Cole, A. J., Yang, V. C. & David, A. E. Cancer theranostics: The rise of targeted magnetic nanoparticles. Trends Biotechnol. 29, 323–332 (2011).
10. Cullity, B. D. & Graham, C. D. Introduction to magnetic Materials. (2009).
11. Frodsham, G. & Pankhurst, Q. A. Biomedical applications of high gradient magnetic separation: progress towards therapeutic haeomofiltration. Biomed. Eng. / Biomed. Tech. 60, 393–404 (2015).
12. Hilger, I. & Kaiser, W. A. Iron oxide-based nanostructures for MRI and magnetic hyperthermia. Nanomedicine 7, 1443–1459 (2012).
13. Pérez-Herrero, E. & Fernández-Medarde, A. Advanced targeted therapies in cancer: Drug nanocarriers, the future of chemotherapy. Eur. J. Pharm. Biopharm. 93, 52–79 (2015).
14. Pankhurst, Q. a, Thanh, N. T. K., Jones, S. K. & Dobson, J. Progress in applications of magnetic nanoparticles in biomedicine. J. Phys. D. Appl. Phys. 42, 224001 (2009).
15. Herrmann, I. K., Schlegel, A. A., Graf, R., Stark, W. J. & Beck-Schimmer, B. Magnetic separation-based blood purification: a promising new approach for the removal of disease-causing compounds? J. Nanobiotechnology 13, 49 (2015).

16. Assa, F. et al. A biotechnological perspective on the application of iron oxide nanoparticles. Nano Res. 9, 2203–2225 (2016).

17. Karwowska, E. Antibacterial potential of nanocomposite-based materials - a short review. Nanotechnol. Rev. 6, 243–254 (2017).

18. Lattuada, M. et al. Theranostic body fluid cleansing: rationally designed magnetic particles enable capturing and detection of bacterial pathogens. J. Mater. Chem. B 4, 7080–7086 (2016).

19. DeNardo, S. J. et al. Development of tumor targeting bioprobes ((111)In-chimeric L6 monoclonal antibody nanoparticles) for alternating magnetic field cancer therapy. Clin. Cancer Res. 11, 7087s–7092s (2005).

20. Sprio, S. et al. Biomimesis and biomorphic transformations: New concepts applied to bone regeneration. J. Biotechnol. 156, 347–355 (2010).

21. Guy, C. & Ffytche, D. An Introduction to The Principles of Medical Imaging.

22. Singh, A. & Sahoo, S. K. Magnetic nanoparticles: a novel platform for cancer theranostics. Drug Discov. Today 19, 474–81 (2013).

23. Mittal, S., Chowhan, R. K. & Singh, L. R. Macromolecular crowding : Macromolecules friend or foe. BBA - Gen. Subj. 1850, 1822–1831 (2015).

24. http://www.mr-tip.com.

25. Nielsen, O. S., Horsman, M. & Overgaard, J. A future for hyperthermia in cancer treatment? Eur. J. Cancer 37, 1587–9 (2001).

26. Busch, C. in Verhandlungen Des Naturhistorischen Vereins Der PreussischenRheinlande und Westphalens (ed. Andrä, C. J.) 28–33 (Max Cohen und Sohn, 1866).

27. Maier-Hauff, K. et al. No Intracranial thermotherapy using magnetic nanoparticles combined with external beam radiotherapy: results of a feasibility study on patients with glioblastoma multiforme. J. Oncol. 81, 53–60 (2007).

28. Mornet, S., Vasseur, S., Grasset, F. & Duguet, E. Magnetic nanoparticle design for medical diagnosis and therapy. J. Mater. Chem. 14, 2161–

2175 (2004).

29. Garaio, E. et al. Specific absorption rate dependence on temperature in magnetic field hyperthermia measured by dynamic hysteresis losses (ac magnetometry). Nanotechnology 26, 15704 (2015).

30. Mohamed, F., Marchettini, P., Stuart, O., Urano, M. & Sugarbaker, P. Thermal enhancement of new chemotherapeutic agents at moderate hyperthermia. Ann Surg Oncol. 10, 463–8 (2003).

31. Gilchrist, R. K. et al. Selective Inductive Heating of Lymph Nodes. Ann. Surg. 146, 596–606 (1957).

32. Maier-Hauff, K. et al. Efficacy and safety of intratumoral thermotherapy using magnetic iron-oxide nanoparticles combined with external beam radiotherapy on patients with recurrent glioblastoma multiforme. J. Neurooncol. 103, 317–324 (2010).

33. Johansen, M. et al. Morbidity and quality of life during thermotherapy using magnetic nanoparticles in locally recurrent prostate cancer : Results of a prospective phase I trial. 23, 315–323 (2007).

34. Thiesen, B. & Jordan, A. Clinical applications of magnetic nanoparticles for hyperthermia. Int. J. Hyperth. 24, 467–474 (2008).

35. Johannsen M, Gneveckow U, Taymoorian K, Thiesen B, Waldöfner N, Scholz R, Jung K, Jordan A, Wust P, L. S. Morbidity and quality of life during thermotherapy using magnetic nanoparticles in locally recurrent prostate cancer: Results of a prospective phase I trial. Int. J. Hyperth. 23, 315–323 (2007).

36. Ferrari, M. Cancer nanotechnology: opportunities and challenges. Nat. Rev. Cancer 5, 161–171 (2005).

37. Sanhai, W. R., Sakamoto, J. H., Canady, R. & Ferrari, M. Seven challenges for nanomedicine. Nat. Nanotechnol. 3, 242–244 (2008).

38. Mirsadeghi, S., Shanehsazzadeh, S., Atyabi, F. & Dinarvand, R. Effect of PEGylated superparamagnetic iron oxide nanoparticles (SPIONs) under magnetic field on amyloid beta fibrillation process. Mater. Sci. Eng. C 59, 390–397 (2016).

39. Riehemann, K. et al. Nanomedicine - Challenge and perspectives. Angew. Chemie - Int. Ed. 48, 872–897 (2009).

40. Ulbrich, K. et al. Targeted Drug Delivery with Polymers and Magnetic Nanoparticles: Covalent and Noncovalent Approaches, Release Control, and Clinical Studies. Chem. Rev. 116, 5338–5431 (2016).
41. Lima-tenório, M. K., Gómez, E. A., Ahmad, N. M., Fessi, H. & Elaissari, A. Magnetic nanoparticles : In vivo cancer diagnosis and therapy. Int. J. Pharm. 493, 313–327 (2015).
42. Brazel, C. S. Magnetothermally-responsive nanomaterials: Combining magnetic nanostructures and thermally-sensitive polymers for triggered drug release. Pharm. Res. 26, 644–656 (2009).
43. Wang, C. et al. Dual-purpose magnetic micelles for MRI and gene delivery. J. Control. Release 163, 82–92 (2012).
44. Ho, D. O. N., Sun, X. & Sun, S. Theranostic Applications. XXX, (2011).

2. Synthesis and characterization of magnetite nanoparticles

Nowadays, there is a great interest in the production of MNPs with magnetic properties tailored for biomedical applications, through reproducible, efficient and economically sustainable techniques. But even though the chemistry underlying the production of MNPs is virtually known, the critical dependence of their physical properties on the particle size, shape and structure, if on one hand allows for a fine tuning of their behaviour, on the other requires a tight control at the synthetic level. A wealth of methods of synthesis has been developed to answer to the different needs arising from the various applications meanwhile granting a fine control on the morphological properties. In the literature many procedures are described concerning the bottom-up approach and most of them are focused on the thermal decomposition of a precursor (metal-organic or inorganic salts) in the presence of surfactants in high boiling solvents[1–3]. It is worth to note that the thermal decomposition method is one of the best in terms of crystallinity, size distribution and magnetic properties of the final product, particularly if compared with the co-precipitation method, the sol-gel processes or the synthesis in reverse micelles. Thanks to these advantages thermal decomposition has rapidly gained a large popularity, becoming one of the most common method for the production of MNPs[4]. However, despite of its large popularity, this technique is still suffering some drawbacks in terms of reproducibility and size or composition control. The main hurdle found by each "nanoparticle-chemist" is indeed to reproduce in his laboratory the procedure illustrated in a paper. This is mainly due to the great number of experimental variables that must be simultaneously controlled in the reaction set-up, like the temperature increasing rate, the stirring rate, the nitrogen flow and many others. Each one of them, indeed, affects the nature and the quality of the final product, thus it is essential to finely control all the synthesis parameters in order to obtain the desired product[5].

In this work, the thermal decomposition of iron acetylacetonate has been chosen as the method to obtain good quality magnetite MNPs in the range of $12 - 16\,nm$ exploitable for our purpose.

In the next paragraph, the optimization of the MNP synthesis in order to obtain a material with the desired properties and with a good yield for the realization of all chemical-physical, magnetic and in vitro and in vivo tests, will be described, while in the following paragraphs we will report the synthesis and characterization of the MNP-HFn hybrid nano-system.

2.1 Synthesis of magnetite nanoparticles

Thermal decomposition of Iron(III) acetylacetonate ($Fe(acac)_3$), is a common route to prepare MNPs of magnetite with excellent structural and physical properties. Unfortunately, a major drawback is represented by the difficulty to obtain MNPs in the 12-16nm range which, as will be discussed in the next chapter, is the best for their use in hyperthermia. In an attempt to overcome this limit, we modified the thermal decomposition procedure of $Fe(acac)_3$ described by Sun and Zeng[3,6], changing the composition of the reaction mix and the heating ramp. In fact, in our synthesis the reaction mix was typically composed by an amount of $Fe(acac)_3$, oleic acid (OA) and oleylamine (OAm), in molar proportion 1:5:5 (typically $8{:}\,40{:}\,40\,mmol$) mixed in c.a $100\,mL$ of benzylether with a typical yield of $\approx 700\,mg$ of dry powder of MNPs. Unlike the synthesis proposed by Sun and Zeng we did not use the 1,2 hexadecandiol (HDD), and we used a different heating ramp, as described in scheme 2.1, modulating t_1 and t_2. The role of HDD is much discussed in the literature: some studies find that the absence of HDD does not influence the iron oxide stoichiometry, i.e. the Fe^{2+}:Fe^{3+} ratio, but slightly reduces the size of the nanoparticles[7]. Therefore, also considering the high cost of HDD, we did not use it but we used the other synthetic parameters, as the volume of solvent, concentration of reagent and reaction time, to tune the characteristic of MNPs. Briefly, in a typical synthesis the mix was magnetically stirred for $30\ min$ under a flow of nitrogen at room temperature, then, once reduced the flux of nitrogen, it was heated to $200\ °C$ in $15\ min$, kept at this temperature for some time, t_1 (nucleation), heated in $10\ min$ to reflux, at c.a 295 °C, and kept there for t_2 (growth).

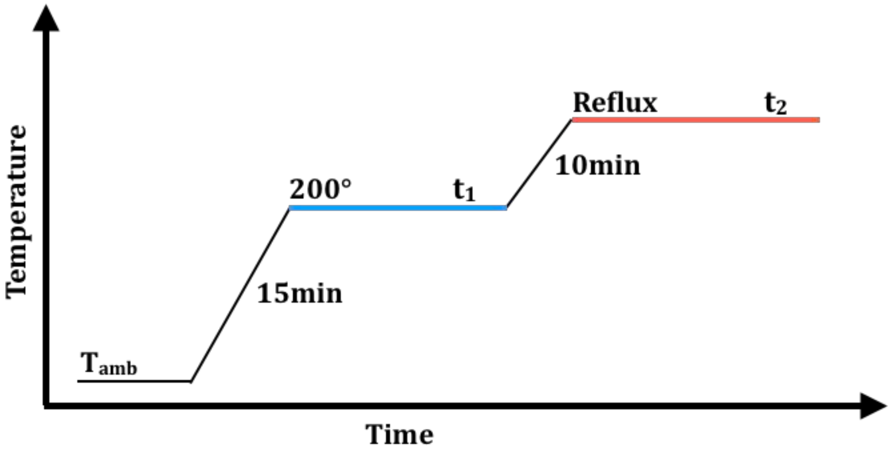

Scheme 2.1: Heating ramp for the synthesis of MNP by thermal decomposition of Fe(acac)$_3$; the first step at t_1 and T_1 ($200\ °C$ in our case,), represented by the blue line corresponds to the nucleation of MNP seeds, the second step at t_2 at the reflux of solvent T_2 represent by the red line, corresponds the growth of the nuclei.

Sample	t_1(min)	t_2(h)	Volume (mL)
MNP-1	30	1	125
MNP-2	30	1	110
MNP-3	30	1,5	110
MNP-4	30	1,5	110
MNP-5	30	1,5	100

Table 2.1 Synthesis parameters used to produce MNPs. t_2 and the volume of benzylether were changed to tune the size of the MNPs.

Several preliminary syntheses were initially performed varying the various parameters (t1, t2, T1 and T2), with the aim of investigating their effect on the morphological characteristics of the final product. These studies, not reported here, showed that keeping $t_1 = 30\ min$ and $T_1 = 200\ °C$ and changing t_2 and the volume of solvent, we were able to synthesize monodisperse MNP with controlled size in the range of interest. Indeed, using nucleation times t_1 longer than $30\ minutes$, independently of the value of the other parameters, we obtained MNPs of size lower than 10 nm, which is not suitable for application as heat mediator in MFH. At the same time, it is necessary reduce the solvent volume to increase the size to the desired ones. Indeed, at reflux the reaction mix is instable, and is hard to have the desired control over the T increasing t_2 over $2\ h$. Thus, a set of samples was prepared varying the solvent volume with $t_2 < 2\ h$, and fixing $t_1 = 30\ min$; the conditions used are reported in table 2.1. Samples MNP-4 and MNP-5 differ from previous samples in the cooling procedure of the reaction mixture. While MNP-1, -2, -3, were quenched to room temperature MNP-4 and MNP-5 were allowed to cool down spontaneously. This shrewdness has allowed us to produce MNPs with narrower size distribution.

The analysis by the Rietveld method of the diffraction patterns of the dried powder confirmed that all the MNPs produced with this synthesis have the cubic spinel crystalline structure of magnetite (PDF 65-3107), Figure 2.1. The XRD data also evidence the absence of traces of wüstite or hematite, which, being antiferromagnetic, would have had a negative effect on the magnetic properties of the MNPs. The Pawley analysis method carried on the XRD patterns (Table 2.2)[8], was used to estimate the size of the crystallite and the lattice parameter of the crystalline cell. Again, this analysis confirms the good quality of the samples as the lattice parameter a were extremely close to that of magnetite ($a = 8{,}3970Å$) than to the maghemite one ($a = 8{,}3515Å$). Indeed, magnetite is the desired iron oxide spinel phase, since it has a better hyperthermic efficiency than maghemite. As it can be seen in table 2.2 the crystal sizes obtained from the Pawley method suggest that we were able to modulate the dimension of MNPs in the $9 - 15\ nm$ range.

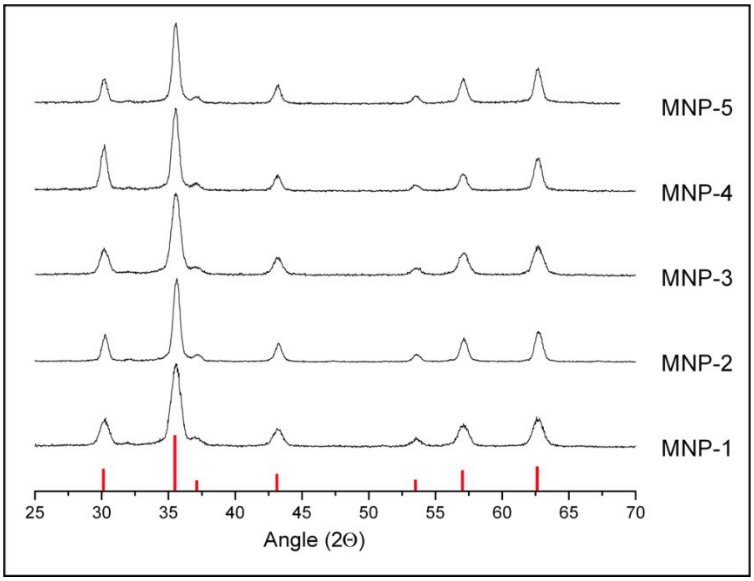

Figure 2.1: XRD Patterns of samples MNP-1, MNP-2, MNP-3, MNP-4 and MNP-5. The red bars correspond to the reference pattern of magnetite (PDF 65-3107).

Sample	Crystal size (nm)	Lattice Parameter Å	$d_{TEM}\ (nm)$	$d_{LN}\ (nm)$	σ_{LN}
MNP-1	$9{,}3$	$8{,}407(3)$	$8{,}0 \pm 0{,}9$	$8{,}0 \pm 0{,}8$	$0{,}102$
MNP-2	$10{,}9$	$8.401(0)$	$10{,}6 \pm 1{,}2$	$10{,}8 \pm 1{,}1$	$0{,}101$
MNP-3	$12{,}1$	$8{,}396(3)$	$13{,}5 \pm 1{,}9$	$13{,}7 \pm 1{,}7$	$0{,}125$
MNP-4	$12{,}8$	$8{,}391(1)$	$12{,}7 \pm 0{,}7$	$12{,}7 \pm 0{,}8$	$0{,}065$
MNP-5	$15{,}2$	$8{,}398(1)$	$15{,}8 \pm 1{,}1$	$15{,}8 \pm 1{,}3$	$0{,}079$

Table 2.2: Crystal size and lattice parameter obtained from the XDR patter fit with Pawley method using T.O.P.A.S.® software, for MNP-1, MNP-2, MNP-3, MNP-4 and MNP-5; Mean diameter from statistical analysis of the size measured on TEM micrograph; $\boldsymbol{d_{LN}}$ Mean Diameter of Log Normal Fit, and σ_{LN}, standard deviation of the Log Normal equation.

For each sample electron micrographs were acquired with a Transmission Electron Microscope (TEM), to reveal the MNP size and evaluate the size distribution. Sample MNP-1 was characterized by a narrow population of, irregular, tiny MNPs, with mean diameter, $d_{TEM} = 8{,}0 \pm 0{,}9\ nm$, which is too small for deliver heat by magnetic fluid hyperthermia (Figure 2.2), while sample MNP-2 comprises bigger nanocrystals with average size $d_{TEM} = 10{,}6 \pm 1{,}2\ nm$, which, unlike the previous case have a more regular octahedral shape.

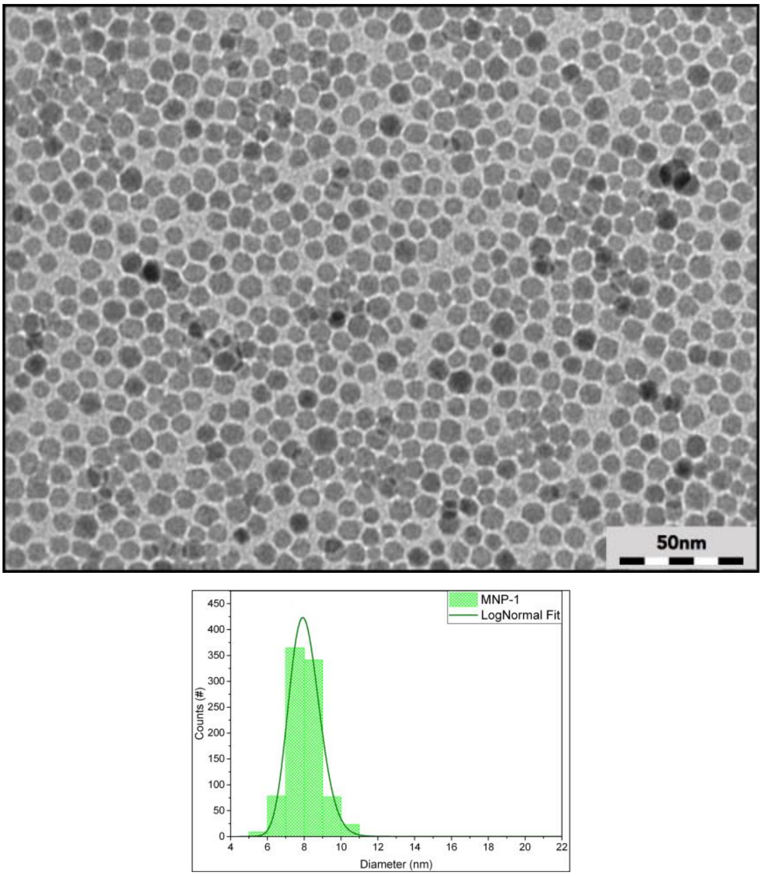

Figure 2.2: A selected TEM micrograph of MNP-1, and the corresponding size distribution of diameter obtained by a statistic over several images; the average diameter is $d_{TEM} = 8{,}0 \pm 0{,}9\ nm$; the green thick line is the fitting to a log normal function with $d_{LN} = 8{,}0 \pm 0{,}8\ nm$.

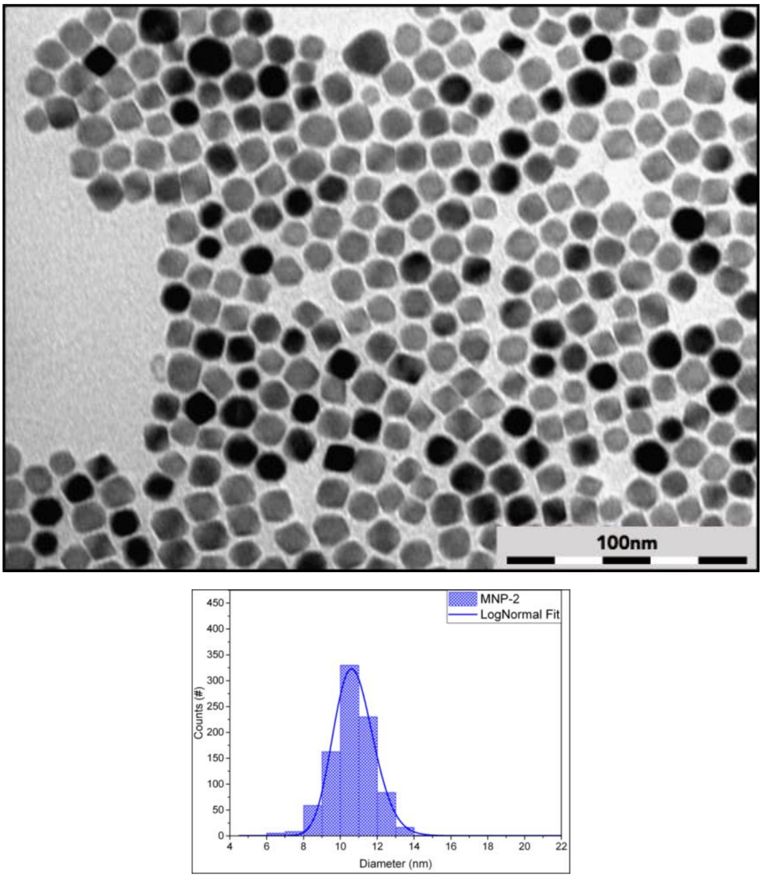

Figure 2.3: A selected TEM micrograph of MNP-2, and the corresponding size distribution of diameter obtained by a statistic over several images; the average diameter is $d_{TEM} = 10,6 \pm 1,2\ nm$; the blue thick line is the fitting to a log normal function with $d_{LN} = 10,7 \pm 1,1\ nm$.

The MNPS of samples obtained increasing t_2, MNP-3-4-5 have a bigger average size, as shown in Figures 2.4, 2.5 and 2.6. In particular, MNP-3 presented a broader size distribution centred at $d_{TEM} = 13,5 \pm 1,9\ nm$ with MNPs of octahedral shape. MNP-4 instead was composed by more uniform and smaller MNPs, with $d_{TEM} = 12,7 \pm 0,7\ nm$, extremely regular in shape. MNP-5 was composed by MNPs larger in size, $d_{TEM} = 15,8 \pm 1,2\ nm$ MNPs, which even in this case have a regular octahedral shape. As previously mentioned the different cooling procedure used in the synthesis of MNP-4 and MNP-5, had given narrower size distribution compared to MNP-3.

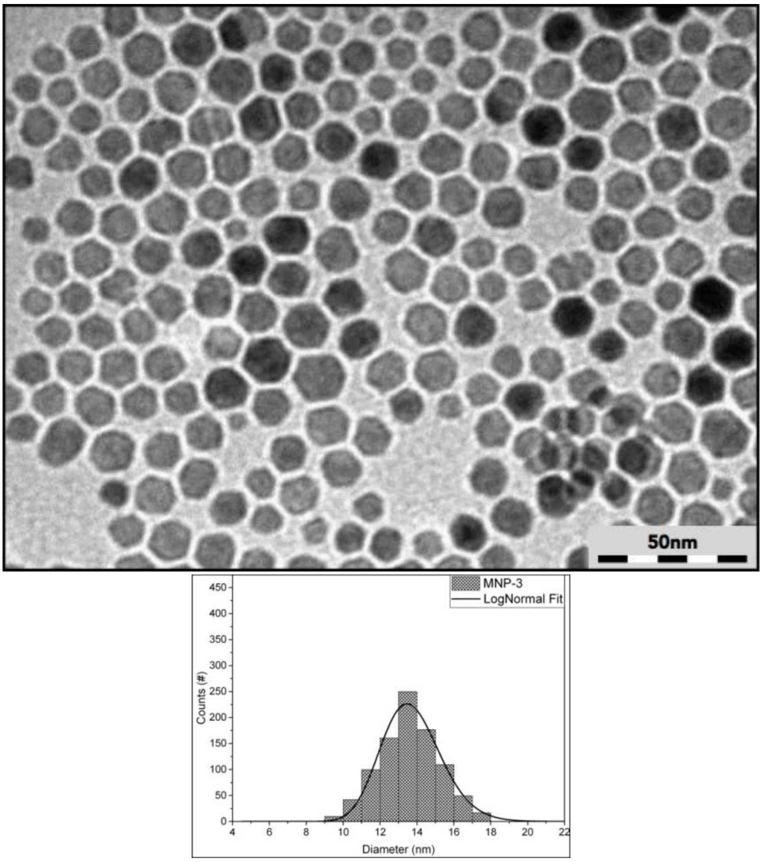

Figure 2.4: A selected TEM micrograph of MNP-3, and the corresponding size distribution of diameter obtained by a statistic over several images; the average diameter is $d_{TEM} = 13{,}5 \pm 1{,}9\ nm$; the black thick line is the fitting to a log normal function with $d_{LN} = 13{,}6 \pm 1{,}7\ nm$.

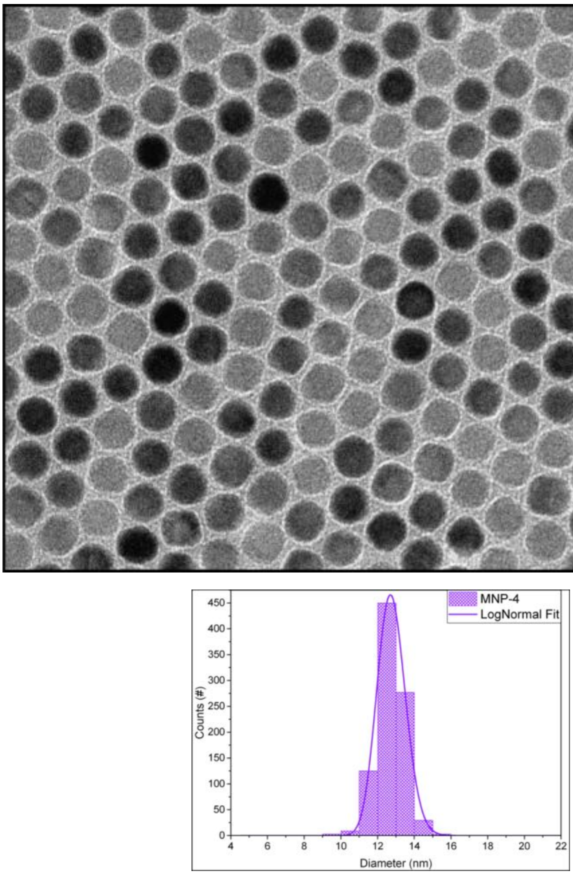

Figure 2.5: A selected TEM micrograph of MNP-1, and the corresponding size distribution of diameter obtained by a statistic over several images; the average diameter is $d_{TEM} = 12{,}7 \pm 0{,}7\ nm$; the purple thick line is the fitting to a log normal function with $d_{LN} = 12{,}7 \pm 0{,}8\ nm$.

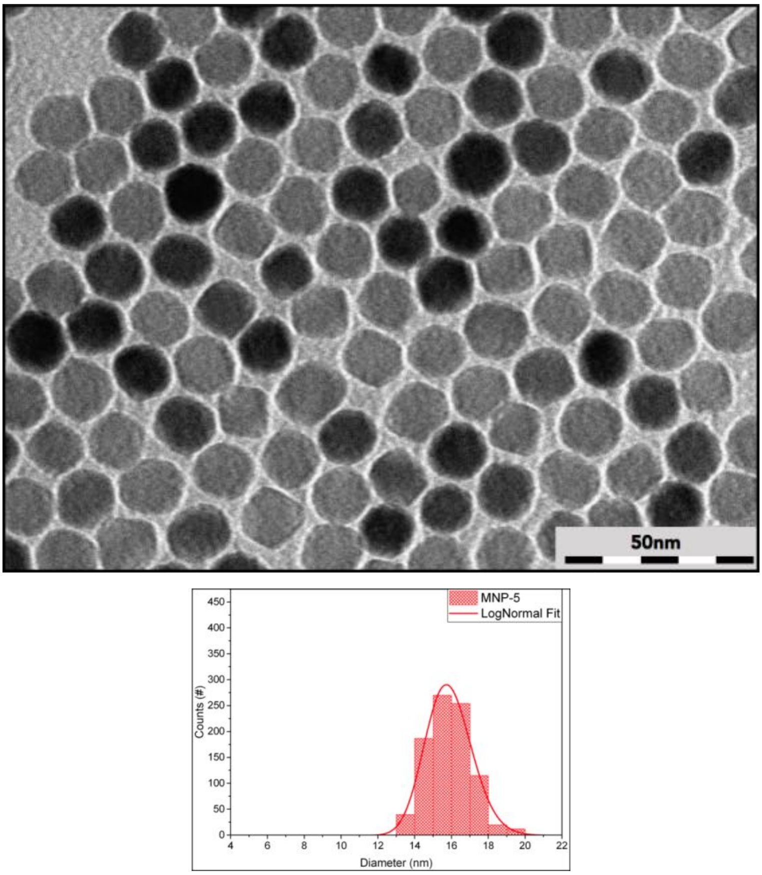

Figure 2.6: A selected TEM micrograph of MNP-1, and the corresponding size distribution of diameter obtained by a statistic over several images; the average diameter is $d_{TEM} = 15{,}8 \pm 1{,}1\ nm$; the red thick line is the fitting to a log normal function with $d_{LN} = 15{,}8 \pm 1{,}3\ nm$.

TEM micrographs and XRD data confirm that this procedure allowed us to obtain samples with high purity of the crystalline phase, and remarkable control over the size distribution. Among the samples we selected those which size falls in the range of our interest, $12 - 16\ nm$. We can thus conclude that the experimental conditions used in this work for the synthesis of MNP-3, -4 and-5, are suited to obtain magnetite MNPs which are efficient heat mediators for magnetic fluid hyperthermia.

2.2 Magnetic Characterization of magnetite nanoparticles

Magnetic properties, clearly, define the ability of the MNPs for the nanomedicine applications of our interest. Therefore, the magnetization of the samples was deeply characterized both as a function of temperature and magnetic field. In particular, since particles with size below 11 nm have very low hyperthermic application in the following will be discussed only the properties of the most promising samples: MNP-3, MNP-4, MNP-5.

All samples were firstly investigated by studying the temperature dependence of the magnetization recorded after zero-field cooling (ZFC) and field-cooling (FC) procedures; in Figure 2.7 are reported the ZFC-FC magnetizations of samples MNP-3, MNP-4 and MNP-5. The three ZFC-FC curves do not show the behaviour expected for not interacting single domain MNPs of size below 15 nm. Actually, the dipole-dipole interactions master the variation of magnetization when this is measured on strongly interacting compact powders, producing an increase of the blocking temperature, T_B, which, as it is our case, falls above the investigated temperature range. Remarkably, in all samples, around $100\ K$ it is visible a kink which can be ascribed to the Verwey transition, a transition typical of bulk magnetite occurring at $120\ K$ and due to a structural rearrangement, with a variation of crystal cell from orthorhombic at low temperature to cubic for temperature above $120\ K$[9].

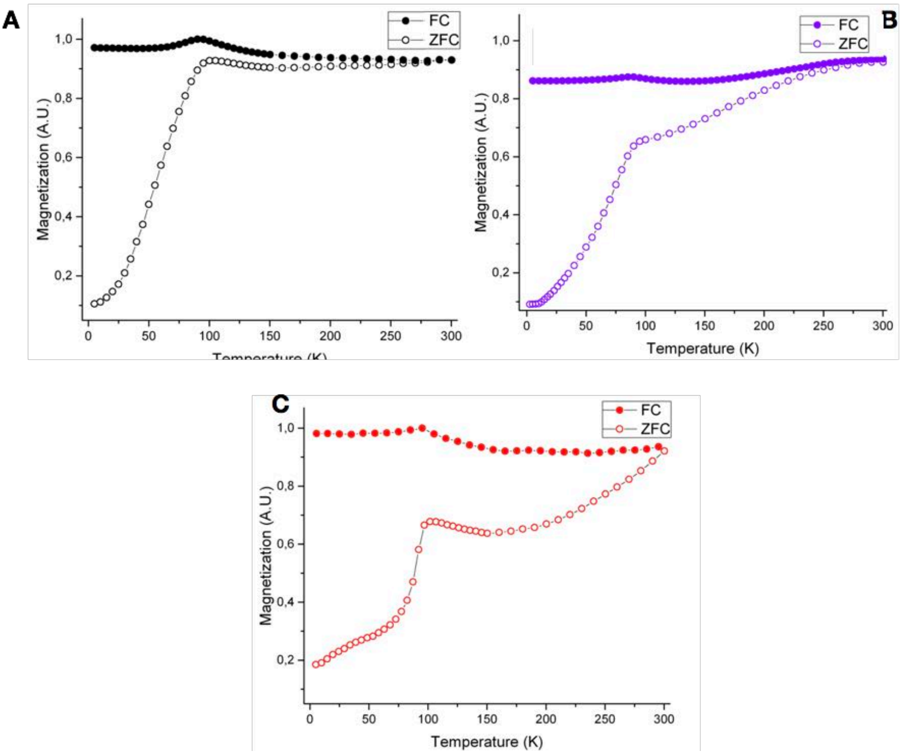

Figure 2.7: Temperature dependence of the ZFC-FC magnetizations of: A) MNP-3(black line); B) MNP-4 (purple line); C) MNP-5 (red line). Empty and full dots refer to ZFC and FC magnetization, respectively.

Figures 2.8 and 2.10 show the magnetization as a function of the applied field, at low temperature ($2{,}5K$) and room temperature($300K$), respectively. At both temperatures the magnetization of all samples, was almost saturated at the highest measuring field of $5\,T$; indeed, the difference between the values measured at $5\,T$ and those extrapolated from the fit of the high field data point to the empirical law $M = M_S + a/H + b/H^2$ is always lower than $1{,}2\,\%$. Such a small difference indicates that the MNPs have a highly ordered magnetic structure, which, in turns reflects the high crystallinity and low defectivity evidence by XRD data.

At low temperature the saturation magnetization, M_S were for all the samples higher than $80\,emu/g$; these value are close to the literature value of the corresponding bulk materials ($95\,emu/g$ magnetite, and $82\,emu/g$ maghemite),

[10] confirming the single crystal nature and the high crystallinity of the inorganic cores.

In figure 2.9 are shown the enlargement of the low field region of the curves recorded at $2.5\ K$. All samples show, as expected, an open hysteresis loop. The characteristic parameter of the hysteresis, coercive field H_C, and reduced remnant magnetization M_{0T}/M_{5T} are reported with the M_S values in table 2.3

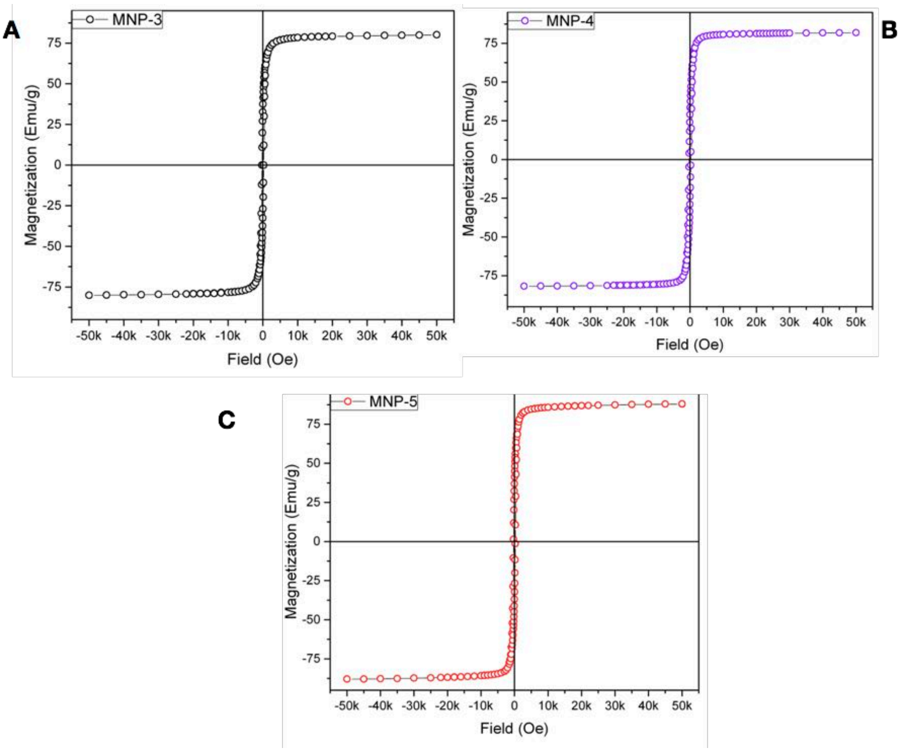

Figure 2.8: Hysteresis loop recorded at $2{,}5\ K$. A) MNP-3 (black symbols); B) MNP-4 (purple circles); C) MNP-5 (red circles).

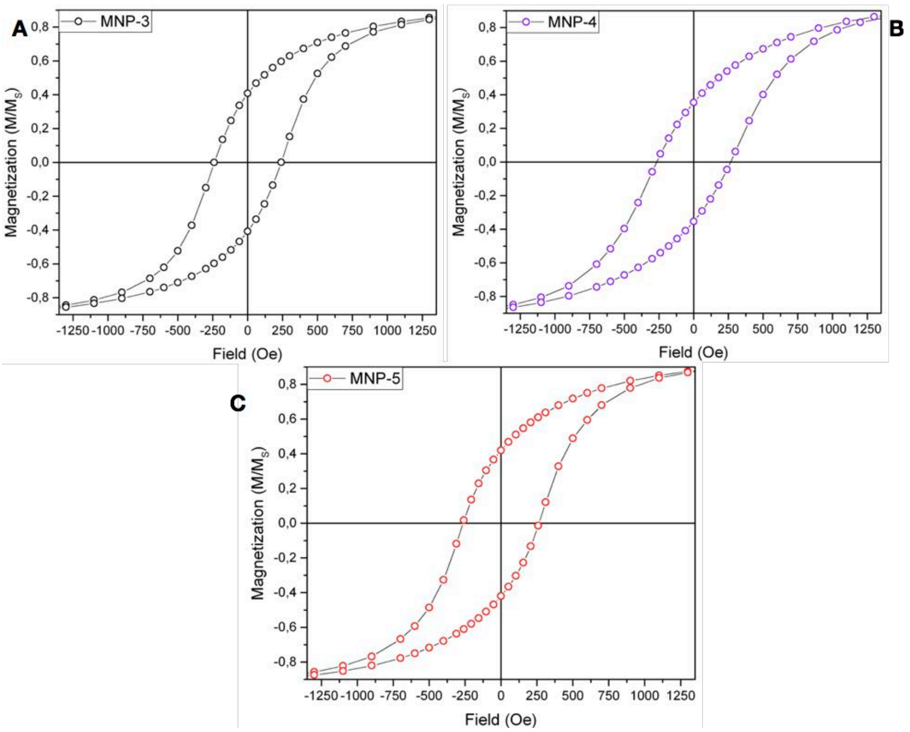

Figure 2.9: Details of the hysteresis loop in the low field region. A) MNP-3 (black symbols); B) MNP-4 (purple symbols); C) MNP-5 (red symbols).

The coercive fields, H_C, are slightly lower with respect to the value reported in the literature for MNP of magnetite of these dimension[11], indicating that magnetic anisotropy, K, is not very high. An approximate estimate of the anisotropy constant can be obtained assuming the coercive field at low temperature is equal to the anisotropy field, H$_{An}$, i.e. $H_C = H_{An} = 2k/\mu_0 M_S$. Under this assumption we obtained for our samples $k = 1{,}05 \cdot 10^5\ erg/cm^3$cm for MNP-3, $k = 1{,}20 \cdot 10^5\ erg/cm^3$for MNP-4, and $k = 1{,}34 \cdot 10^5\ erg/cm^3$for MNP-5. These value are rather lower than the term of magneto-crystalline anisotropy of maghemite and magnetite[12]. However, it should be taken into account that k values obtained in this way could be underestimated due to the reduction of the effective field for the reversal of the magnetization caused by inter-particles interactions, which, as we had seen before, are extremely relevant in powder samples.

Sample	M_S 300K (emu/g)	M_S 2,5K (emu/g)	H_C (Oe)	M_{0T}/M_{5T}
MNP-3	72	81	237	0,41
MNP-4	74	83	265	0,35
MNP-5	78	89	273	0,42

Table 2.3: Magnetic saturation, M_S extrapolated from magnetization curves at room temperature (300 K) ad low temperature(2,5 K); Coercive Field, H_C, and remnant magnetization M_{0T}/M_{5T} obtained from the hysteresis loop. M_S were given as emu per g of magnetc material.

In the room temperature loops, no magnetic irreversibility is observed, as shown in Figure 2.11, indicating on this time scale, the MNPS are in the superparamagnetic state for all the samples, as expected for magnetite MNPs of this dimension. The saturation magnetization calculated from the fit of the high field data are reported in table 2.3.

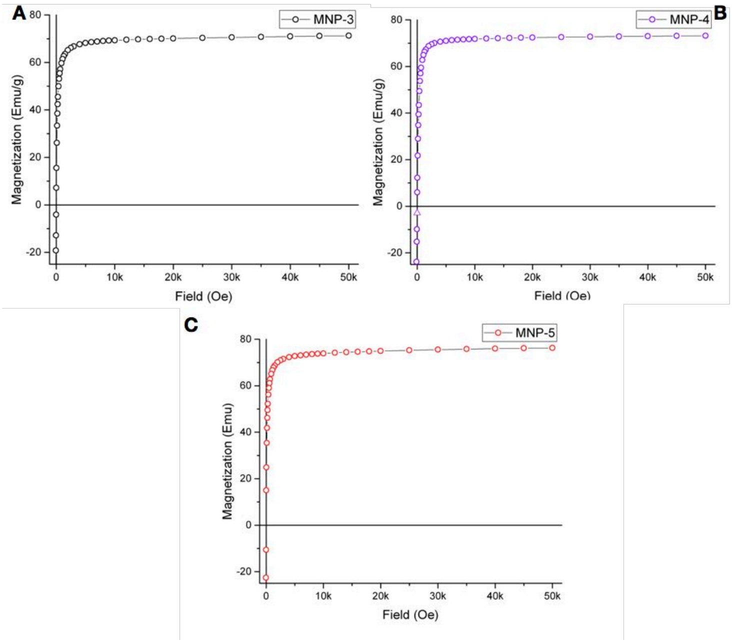

Figure 2.10: Magnetization recorded at room temperature. A) MNP-3 (black line); B) MNP-4 (purple line); C) MNP-5 (red line).

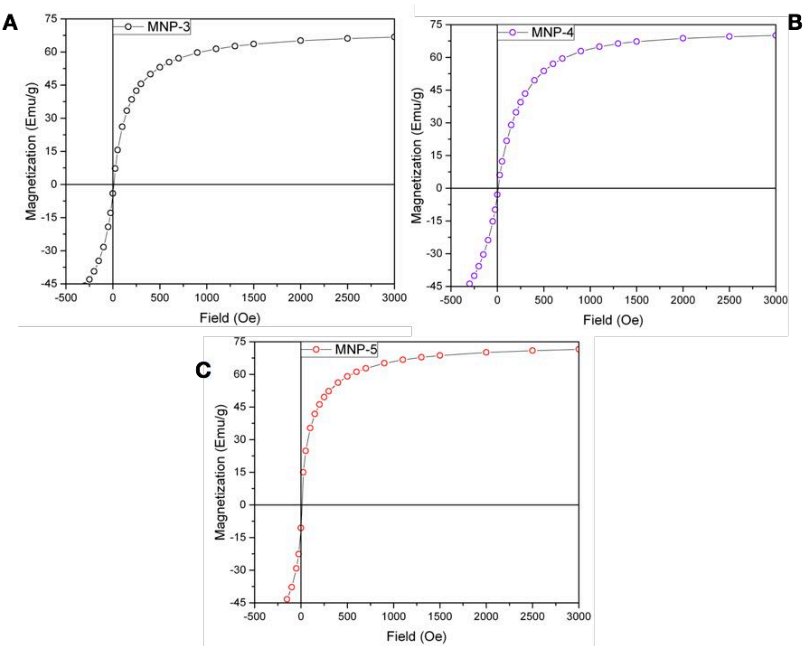

Figure 2.11: Details of the magnetization recorded at room temperature in the low field region. A) MNP-3 (black circles); B) MNP-4 (purple circles); C) MNP-5 (red circles).

2.3 Functionalization of MNPs with hydrophilic ligand

The synthesized MNPs are covered by a layer of Oleic Acid (OA) which makes them soluble in apolar solvents. As a pre requisite, for their subsequent functionalization with ferritins, it is necessary to replace the surfactant with a ligand that allows the dispersion in water and exposes on the surface functional groups suitable for the following grafting of the protein. The strategy adopted was based on the ligand exchange, i.e. treating a MNP suspension with a high excess of a bifunctional molecules containing at one end a functional group with high affinity for the surface of the inorganic nucleus and at the other a functional group suitable for the linkage of HFn. To this purpose, we chose 3-AminoPropylPhosphonic Acid (APPA). This ligand has high affinity for iron oxide, conferred by the phosphonate group forming stable covalent bonds on the surface of the MNP[13]. In addition, it possesses a primary amine (-NH2) that ensures the necessary hydrophilicity, and at the same time it is available for subsequent functionalization with HFn. Indeed, amino groups can easily react with activated acyl groups forming an amide, a reaction which has been exploited n our case, to connect the MNP with an ethero-bifunctional linker. as will be described later.

The toluene suspension of MNPs (10mg/mL Fe_3O_4) was mixed with an equal volume of a dichloromethane solution of APPA (10mg/mL) and Tetramethylammonium hydroxide (TMAOH, 10mg/mL) and sonicated for one hour. Then, MNPs were separated with a permanent magnet, washed with ethanol and suspended in water.

After the reaction the samples appear as a limpid, dark brown water suspension, which remains stable over long time, usually at least 6 months. The high hydrophilicity of the product, nicely suggests the complete realization of the ligand exchange, which was further also confirmed by CHN analysis and by the Z-potential values $\approx -24\ mV$ of the water suspensions.

The magnetic properties of the MNPs were controlled after the ligand exchange with APPA, in order to verify if the coordination modification of the iron ions located at the surface could affect the behaviour of the core.

From the field dependence of the magnetization at low (2.5 K) and room temperature, shown in figures 2.12, 2.13, and 2.14, for MNP-3, MNP-4 and MNP-5, respectively; we can note that in all cases the saturation magnetizations does not change, although a clear variation in the approach to saturation is observed. Indeed. After the ligand exchange the MNPs require a larger field to saturate. Moreover, after coating with APPA an increase of the coercivity from about 250 to about 500 is observed. For the sake of clarity, the values of the main magnetic parameters extracted from these curves are summarized in Table 2.4.

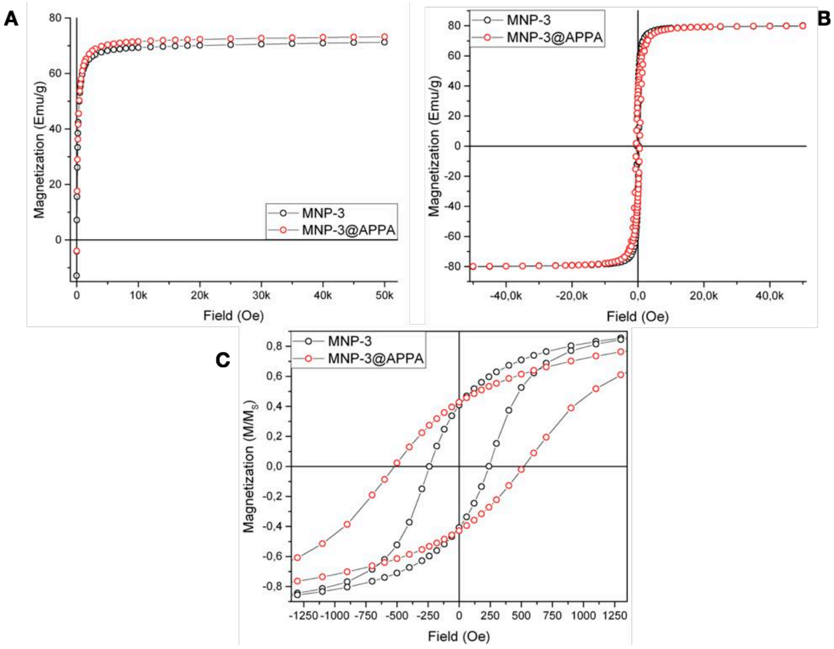

Figure 2.12: Field dependence of the magnetization for MNP-3 (black circles) and MNP-3@APPA (red circles) recorded at: A) room temperature; B) low temperature; C) detail of the low field region.

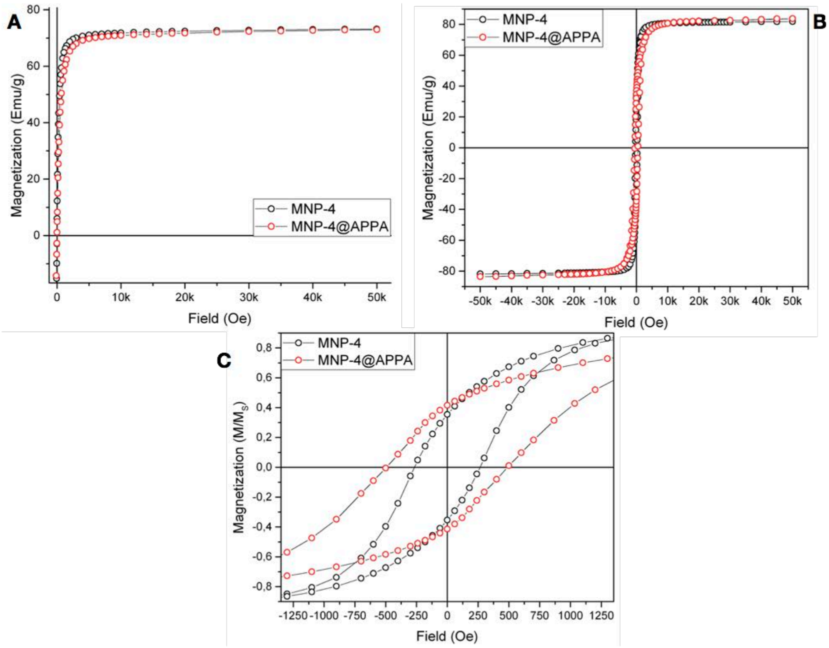

Figure 2.13: Field dependence of the magnetization for MNP-4 (black circles) and MNP-4@APPA (red circles) recorded at: A) room temperature; B) low temperature; C) detail of the low field region.

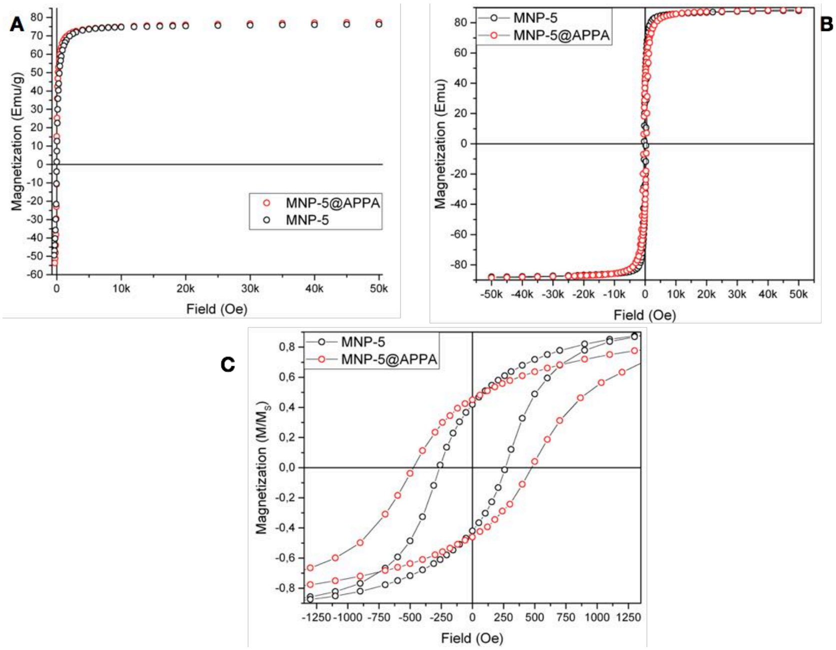

Figure 2.14: Field dependence of the magnetization for MNP-5 (black circles) and MNP-5@APPA (red circles) recorded at: A) room temperature; B) low temperature; C) detail of the low field region.

	MNP-3	MNP-3 @APPA	MNP-4	MNP-4 @APPA	MNP-5	MNP-5 @APPA
$\boldsymbol{M_S}$ $\mathbf{300K}$ $(\boldsymbol{emu/g})$	72	75	74	74	78	79
$\boldsymbol{M_S}$ $\mathbf{2,5K}$ $(\boldsymbol{emu/g})$	81	83	83	86	89	91
$\boldsymbol{H_C}$ $(\boldsymbol{Oe})$	237	525	265	500	273	480
$\boldsymbol{M_{0T}/M_{5T}}$	0,41	0,42	0,35	0,41	0,45	0,45

Table 2.4: Magnetic parameters of samples before and after the ligand exchange. Magnetization saturation, M_S was extrapolated from the high field data; Coercive Field, H_C, and remnant magnetization M_{0T}/M_{5T} obtained from the hysteresis loop. M_S were given as emu per g of magnetc material.

The variation of these parameters is coherent with an increase in spin disorder at the surface occurred after the change of functionalization. The coordination of the carboxyl group of OA to the surface metal ions is known to reduce the surface spin disorder[14]. On the other hand, the coordination of the phosphonate of APPA may produce a lower degree of spin alignment at the surface increasing the spin disorder which often characterize small MNPs. The increased spin disorder reverberates on the magnetic properties of the MNPs on two levels, on the one hand it makes the saturation more difficult, on the other hand, it makes larger the energy barrier to be overcome to reverse the magnetization, causing an increase in the coercive field.

In this Chapter we have seen how the thermal decomposition synthesis can be successfully used to prepare MNPs of controlled size by simply tuning some synthesis parameters, such as t_2 times and the reaction volumes. The analyses performed confirmed that all the samples contain only one crystalline phase, with no defects, exhibit superparamagnetic behaviour at room temperature and bulk-like magnetic saturation. In conclusion, we can claim that the chosen synthesis permitted to produce inorganic magnetic cores with characteristic suitable for the realization of a nano-device for biomedical applications.

1. Saravanan, P., Gopalan, R. & Chandrasekaran, V. Synthesis and characterisation of nanomaterials. Def. Sci. J. 58, 504–516 (2008).
2. Ho, D. O. N., Sun, X. & Sun, S. Theranostic Applications. XXX, (2011).
3. Sun, S. & Zeng, H. Size-Controlled Synthesis of Magnetite Nanoparticles. 8204–8205 (2002). doi:10.1021/ja026501x
4. Effenberger, F. B. et al. Economically attractive route for the preparation of high quality magnetic nanoparticles by the thermal decomposition of iron(III) acetylacetonate. Nanotechnology 28, 115603 (2017).
5. Calero, V., Gonzalez, A. M. & Rinaldi, C. A Statistical Anlaysis to control the Growth of cobalt Ferrite Nanoparticles Synthesized by the thermodecomposition Metod. J. Manuf. Sci. engeineering 132, 30914-1-7 (2010).
6. Sun, S. et al. Monodisperse MFe2O4 (M= Fe, Co, Mn) Nanoparticles. J. Am. Chem. Soc. 4, 126–132 (2004).
7. Guardia, P., Labarta, A. & Batlle, X. Tuning the Size, the Shape, and the Magnetic Properties of Iron Oxide Nanoparticles. J. Phys. Chem. C 115, 390–396 (2011).
8. Total Pattern Analysis Solution T.O.P.A.S. Available at: https://www.bruker.com/fileadmin/user_upload/8-PDF-Docs/X-rayDiffraction_ElementalAnalysis/XRD/Flyers/TOPAS_Flyer_DOC-H88-EXS013_V2_en_high.pdf.
9. Mertens, D. The Verwey Transition in Magnetite. Available at: http://guava.physics.uiuc.edu/~nigel/courses/569/Essays_Spring2006/files/Mertens.pdf.
10. Schieber, M. Experimenta Magnetochemistry, nonmetallic magnetic material.
11. Lartigue, L. et al. Water-Dispersible Sugar-Coated Iron Oxide Nanoparticles. An Evaluation of their Relaxometric and Magnetic Hyperthermia Properties. J. Am. Chem. Soc. 133, 10459–10472 (2011).
12. Cornell, R.M., Schwertmann, U. The iron oxides: structure, properties, reactions, occurrence and uses. Mineral. Mag. 61, 741 (2003).
13. Sahoo, Y. et al. Alkyl Phosphonate / Phosphate Coating on Magnetite Nanoparticles : A Comparison with Fatty Acids. 7907–7911 (2001).

14. Guardia, P. et al. Surfactant effects in magnetite nanoparticles of controlled size. J. Magn. Magn. Mater. 316, 756–759 (2007).

3. Magnetic properties applied to nanomedicine

As previously described the main goal of this work is to exploit the properties of MNPs with superparamagnetic behaviour for both therapeutic and diagnostic applications. In this chapter, after a brief introduction on the mechanisms responsible for the heating capability of MNPs, we will discuss the efficiency in magnetic hyperthermia and magnetic resonance imaging of the MNPs and MNP-HFn systems prepared in this work.

3.1 Magnetic Hyperthermia

3.1.1 MNPs heat releasing: mechanism and efficiency

The heating efficiency of a given material under the application of an alternating magnetic field, is quantified by the Specific Absorption Rate (SAR), defined as the amount of energy converted into heat per unit of time and mass. The main mechanisms responsible for the heat dissipation process are:

- the development of parasitic currents (eddy currents);
- The irreversible reversal of the magnetization, (hysteresis cycle).

For particles in the nanometric scale, the first contribution can be neglected because the size is are too small for eddy currents to be induced.

When a magnetic field of frequency $\nu$and amplitude $H_0$is applied to a dispersion of MNPs in water, the amount of magnetic energy converted into heat is proportional to the hysteresis cycle area:

$$SAR = \mu_0 \nu \oint M(H) dH \qquad (1)$$

where μ_0 is the magnetic permeability of free space.

To assess the cycle area and to describe the mechanism by which heat is developed, we can adopt different models, whose applicability depends on the size of the MNPs. For mono-dispersed MNPs, the heat development mechanism can be described by the linear response theory (LRT). The main assumption of this model is that the magnetization varies linearly with the oscillating magnetic field:

$$H(t) = H_0 \, cos \, 2\pi\nu t = R_e H_0 e^{i2\pi\nu t} \qquad (2)$$

so that

$$M(t) = \chi \cdot H(t) = \chi \cdot R_e H_0 e^{i2\pi\nu t} = H_0(\chi' \, cos \, 2\pi\nu t + \chi'' \, sin \, 2\pi\nu t) \qquad (3)$$

Where t is the time of oscillation of the AMF and χ' and χ'' represent the in-phase and out-of-phase part of the magnetic susceptibility, respectively. This hypothesis is valid if we assume that the magnetic anisotropy barrier and the field oscillations are small compared to thermal energy, ${}^{KV}/_{k_B T} \ll 1$ and $\mu_0 \, {}^{\mu H}/_{k_B T} \ll 1$; where K is the anisotropy constant, V is the volume of the MNP, k_B is the Boltzmann costant, μ the magnetic moment and, H the external magnetic field. When these conditions are met, the dissipated power is given by:

$$SAR = \frac{\pi\nu\mu_0 H_0^2}{\rho} \cdot \chi'' = \frac{\pi\nu\mu_0^2 H_0^2 M_S^2 V}{3\rho k_B T} \cdot \frac{2\pi\nu\tau_{eff}}{1+(2\pi\nu\tau_{eff})^2} \qquad (4)$$

where ρ is the density of the material, and τ_{eff} is the effective relaxation time of the magnetization. Considering a MNP system suspended in a fluid matrix, then τ_{eff} is due to two competing mechanisms: Néel relaxation, described as $\tau_N = \tau_0 e^{\frac{E_a}{K_B T}}$, which depends on the intrinsic magnetic characteristics of MNPs and Brown relaxation, $\tau_B = \frac{3\eta V_H}{k_B T}$, corresponding to the physical rotation of MNPs in the fluid in which they are suspended. Brown's relaxation therefore depends on the hydrodynamic characteristics of the fluid as the viscosity, η and the hydrodynamic volume V_H of the MNPs. Then τ_{eff} will be determined by the fastest process:

$$\frac{1}{\tau_{eff}} = \frac{1}{\tau_N} + \frac{1}{\tau_B} \tag{5}$$

From Eq. 4 two main considerations follow. The first is that maximization of the SAR occurs when $2\pi\nu\tau_{\text{eff}} = \omega\tau_{\text{eff}} = 1$, namely when the relaxation time is equal to the characteristic time of the measurement (in this case the inverse of the applied field frequency). These condition corresponds to the blocking of magnetization at the times scale of the experiment. Secondly, for in vivo application of hyperthermia, it is always better to have Néel relaxation as a dominant process. In fact, in this way, the dissipated power depends solely on the intrinsic properties of the inorganic nucleus (size and anisotropy), and remains independent of environmental conditions that are not always easily controllable.

From eq. 4 it is even clear that many parameters influence the heat power dissipation. In figure 3.1 is represented the SAR dependence on the magnetization of saturation, on the anisotropy and on the dimension evaluated using Eq. 4. Figure 3.1A shows that for magnetite MNPs ($K = 15\ kJm^{-3}$, $\mathrm{M_S} = 450\ KAm^{-1}$) the SAR has a well pronounced, sharp maximum at a definite value, arising from the sum of the contribution of Néel and Brown relaxation. Figure 3.1b and 3.1c demonstrate that the maximum of SAR grows as the magnetization saturation increases and as the crystalline energy decreases, and, in the latter case, it shift to lower diameters.

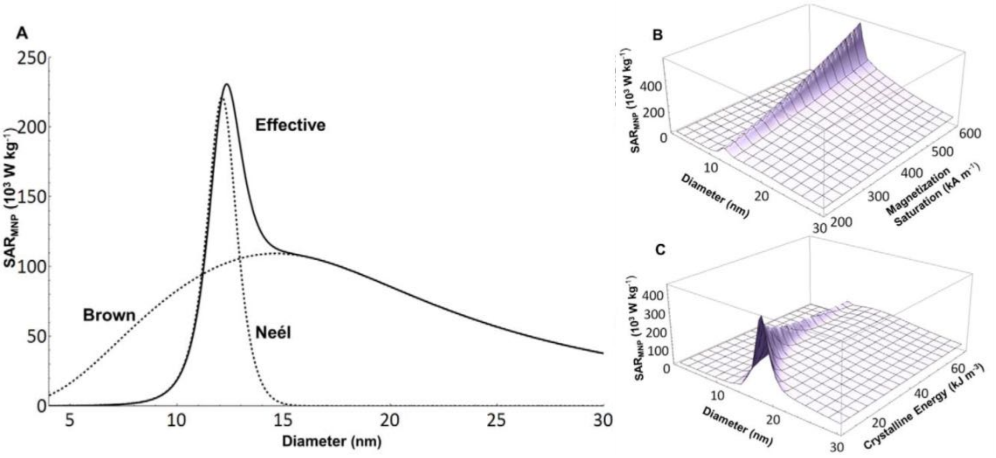

Figure 3. 1 Dependence of SAR evaluated from Eq. 4 on A) Size, B) magnetization saturation and C) magnetic anysotropy (crystalline energy). All the calculation were performed for a magnetite MNPs, $K = 15\ kJm^{-3}$, $M_S = 450\ KAm^{-1}$, $H_0 = 10kAm^{-1}$and $f = 500kHz$.

Typically for MNPs of magnetite the dimension that maxime SAR according to theoretical evaluation fall in the $12 - 18\ nm$ windowrange, and in $15 - 23nm$ range for maghemite[1]. However, for a real system, we should always consider the polydispersity of the sample. Size distribution of MNPs can be usually described by a log-normal distribution function:

$$f(d) = \frac{1}{\sigma_{LN} d\sqrt{2\pi}} \cdot exp\left[-\frac{(\ln(d/d_{LN}))^2}{2\sigma_{LN}^2}\right] \tag{6}$$

where $\ln\ d_{LN}$ is the expectation value of the log-normal distribution and σ_{LN} is the standard deviation of $ln(d)$. Then the SAR of the polydispersed sample becomes:

$$SAR_{tot} = \int_0^{\infty} \frac{\pi \nu \mu_0 {H_0}^2}{\rho} \cdot \chi'' \cdot f(d)\, \mathrm{d}d \tag{7}$$

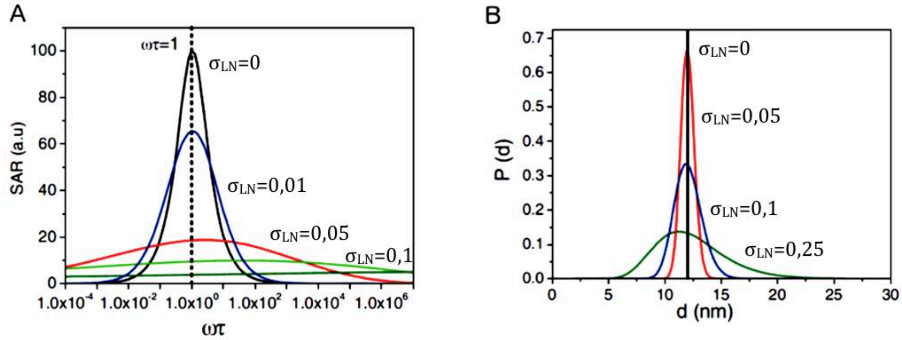

Figure 3. 2 Variation of SAR as a function of $\omega\tau$*, for MNPs distributions with* $d = 12nm$ *and* $\sigma_{LN} = 0/0,1/0,05/0,001.$ *B) Distribution Functions Used to Calculate SAR with Eq. 6.*

In Figure 3.2, left panel, the variation of SAR as a function of $\omega\tau$ for the size distribution reported in the right panel, are shown. The Figures show that proper size and narrow dimensional distribution are the fundamental requirements to maximize heat dispersion efficiency for a given material.

3.1.2 Heating power, limits and evaluation

As mentioned in the previous paragraph, SAR depends directly on the square of the applied field amplitude, H_0, and on the operating frequency ν. Taking a sample of MNPs it might be thought that the simplest way to increase SAR is to increase the parameters of the applied AMF. However, only a narrow window of H_0 and ν are allowed for *in-vivo* application. Figure 3.3 shows AMF exposure limit values, obtained from theoretical evaluations, beyond which eddy currents are generated in the tissues, and peripheral nerves and heart tissue are stimulated[2]. The grey area between the dotted lines represents the safety area in terms of frequency and strength in which it is possible to operate without major side effects. These values, obtained by theoretical modelling[2,3] have not been experimentally verified on human being, yet. In the Figure are reported also the field values used in clinical trials carried out by Jordan et al[4,5], (red arrow), which partially exceed the theoretical limit. As a matter of fact, in the absence of a thorough clinical study on safety limits and regulations about human body exposure to AMF, currently are considered as safe operating condition in which $H_0 \times \nu$ does not exceed $5 \cdot 10^9\ Am^{-1}s^{-1}$. This values have been obtained by monitoring side effects on humans directly exposed to the AMF. Based on this limit, the commonly accepted field parameters are H_0, below$18\ kAm^{-1}$ and frequencies between $100 - 300\ kHz$.

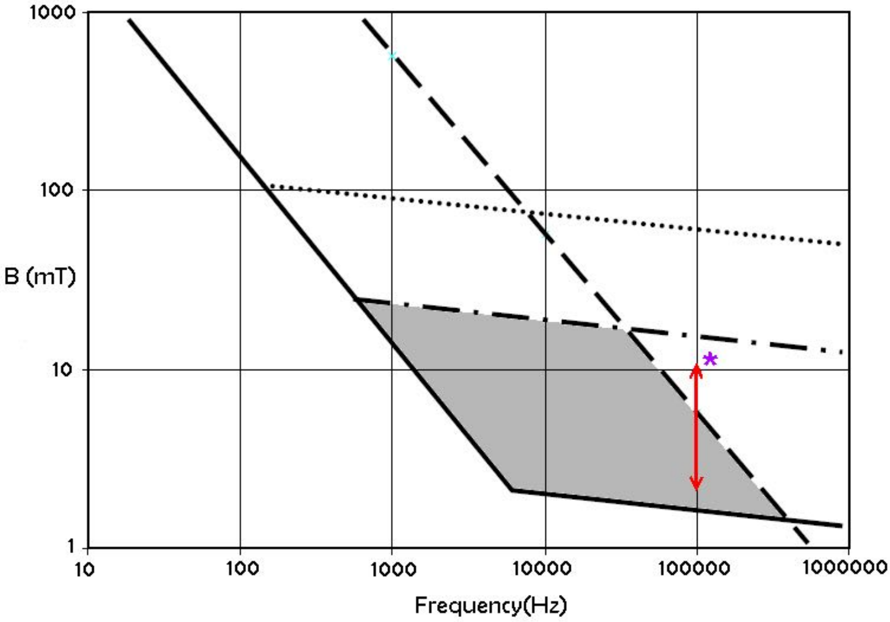

Figure 3. 3: Stimulus thresholds of peripheral nerves and heart tissue under the action of an AMF for an average adult. The dotted line represents the threshold for cardiac tissues, the dot-dashed line the peripheral nerves while the dashed line the threshold beyond which eddy current are generated. Red arrow represents experimental conditions in MFH trials; the violet star corresponds to the value used for the most of experiments performed in this work.

In all the experiments carried out in this experimental work we chose an AMF of $17\ kAm^{-1}$and $183\ kHz$, below the above mentioned threshold.

The simplest way to experimentally evaluate the SAR is to perform a calorimetric measurement of MNPs suspended in a fluid and exposed to an AMF. The SAR can in fact be obtained by measuring the total heat released by the system divided by the mass of the heating material and the time of action of the AMF:

$$SAR = \frac{\sum_i m_i C_{pi}}{m_{Me}} \cdot \frac{\Delta T}{\Delta t} \; (Wg^{-1}) \qquad (8)$$

where $\sum_i m_i C_{pi} \Delta T$ is the sum of the amount of heat released by all the components i of the system, m_{Me} is the total mass of the magnetic material and Δt is the time of action of the AMF.

Experimentally, the SAR evaluation is performed by measuring the temperature variation during the AMF application under adiabatic conditions, from which $\frac{\Delta T}{\Delta t}$ is obtained; then, if the composition of the system is known the SAR can be calculated through Eq. 8. If the measuring system were perfectly adiabatic, the variation of temperature during the time of measurement would be linear, and the SAR could be simply calculated from the final $\frac{\Delta T}{\Delta t}$. However, most of the measuring devices are not perfectly adiabatic and the temperature kinetics are therefore affected by the heat exchange of the sample with the environment. Due to this instrumental limit, the most commonly procedure consists in extrapolating the initial slope of the curve $T(t)$, to obtain a $\frac{dT}{dt}$ value where the heat dissipation is minimal. Figure 3.4 shows a typical elaboration of the experimental data, with the linear fit of the temperature kinetic of a sample of MNPs exposed to an AMF.

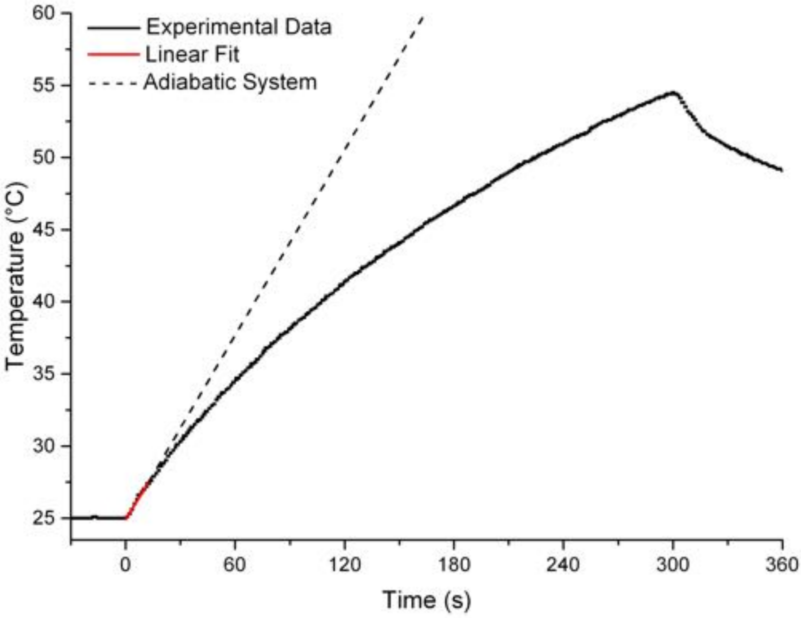

Figure 3. 4: Example of the elaboration of the kinetic evolution of temperature to extrapolete the initial slope. Black line is the experimental data, red line the linear fit of $\Delta t = 15\ s$, dotted line the evolution of an adiabatic system

3.1.3 Hyperthermic efficiency analysis

As mentioned in Chapter 2, samples with most suitable dimension for biomedical applications are MNP-3-4-5. Here we analyse and discuss the hyperthermic behaviour of these three samples. The hyperthermic properties were measured suspending the MNP in different media: toluene, water and agarose gel. Such an in-depth study of the hyperthermic behaviour of MNPs is aimed at verifying that the hyperthermic efficiency is not adversely affected by the environment in which they are suspended. Indeed, as previously mentioned, SAR is influenced by both intrinsic and external parameters, whose *a priori* evaluation from magnetic data is not simple.

3.1.3.1 Hyperthermic efficiency in organic suspension

To investigate the hyperthermic efficiency of toluene suspension of the three MNP samples coated with oleic acid, aliquots of 1mL at a concentration of $5\,mg/mL$ of each samples were exposed to a AMF of $183\ kHz$ frequency and $17\ kAm^{-1}$ amplitude, while recording the temperature variation during the time of the action of the field by a optic fiber probe dipped into the sample.

The temperature increase was evaluated by a linear fit of the initial slope, as previously described, taking at least $10\ s$ as Δt. For every sample many different measurements were repeated to verify the reproducibility of the experiment. In figure 3.5 are shown the heating kinetics of MNP-3, MNP-4 and MNP-5.

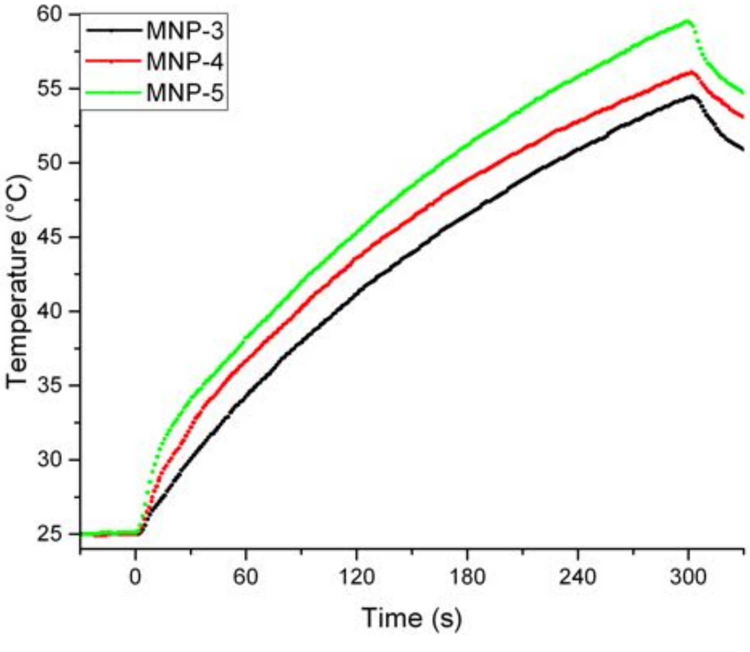

Figure 3. 5: kinetic evolution of temperature of $5\,mg/mL$ toluene suspension of MNPs. MNP-3, black line; MNP-4, red line; MNP-5, green line.

The SAR evaluated for the samples are reported in table 3.1. Sample MNP-5 ($15{,}8\,nm$) shown as expected, the highest value, $81{,}2\,Wg^{-1}$, while MNP-4

($12{,}7\ nm$) and MNP-3 ($13{,}5\ nm$), although of comparable size display significant different SAR.

Sample	$SAR\ (Wg_{MNP}^{-1})$
$MNP-3$	33,5
$MNP-4$	55,8
$MNP-5$	81,2

Table 3. 1 SAR values obtained for MNPs suspension in toluene, $5\ mg/mL$ of concentration of iron oxide, applied field of $183\ kHz$ frequency and $17\ kAm^{-1}$ intensity for $\Delta t = 300s$.

3.1.3.2 Hyperthermic efficiency in water suspension

The value of SAR measured in toluene is not necessary representative of the intrinsic SAR of the sample. Indeed, MNPs suspended in different media can experience different interactions and can also have different stability, two factors which can influence the final heating efficiency.

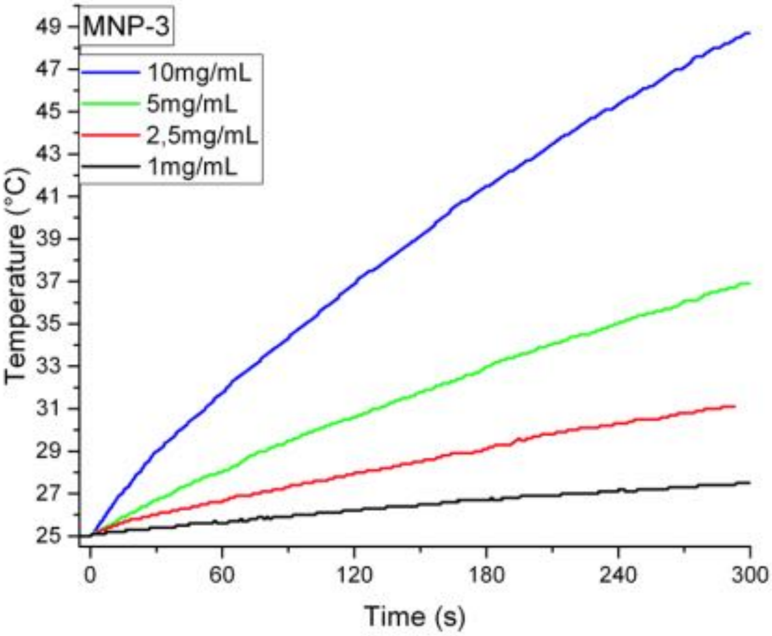

Figure 3. 6: Kinetic evolution of temperature of a MNP-3 water suspension with increasing concentration $1, 2{,}5, 5$ *and* $10\ mg/mL$.

The hyperthermic efficiency of water dispersion of MNPs samples was investigated after the ligand exchange with APPA. Aliquots of MNPs suspension with different concentration in the range $10\ mg/mL - 1\ mg/mL$ were exposed to an AMF using the same field parameters. In Figure 3.6 the kinetic curves recorded for MNP-3 are shown. As expected the SAR values reported in table 3.2, are almost double compared to the ones evaluated in toluene.

$\boldsymbol{MNP-3}$	$\boldsymbol{SAR\ (Wg_{MNP}^{-1})}$
$\boldsymbol{10mg/mL}$	$65{,}8 \pm 5{,}1$
$\boldsymbol{5mg/mL}$	$58{,}3 \pm 4{,}7$
$\boldsymbol{2{,}5mg/mL}$	$69{,}0 \pm 6{,}0$
$\boldsymbol{1mg/mL}$	$58{,}6 \pm 4{,}1$

Table 3. 2 SAR values obtained for MNP-3 sample suspended at different concentration in $1\ mL$ *of water and exposed for* $300\ s$ *to a AMF (*$183\ kHz, 17\ kAm^{-1}$*); mean values are obtained averaging over 5 data.*

Even in water suspension SAR is independent on the concentration, the observed oscillations being within the uncertainty of measurement. Comparing curves recorded in water and toluene suspensions at same concentration (5 mg/mL) the total ΔT is larger in toluene due to the much higher specific heat of water.

Interestingly, SAR value for MNP-4 and MNP-5 were closer each other and significantly much higher than MNP-3. In figure 3.7 are shown the kinetic curves recorded for sample MNP-4 at different concentration while in table 3.3 are reported the mean SAR evaluated at each concentration.

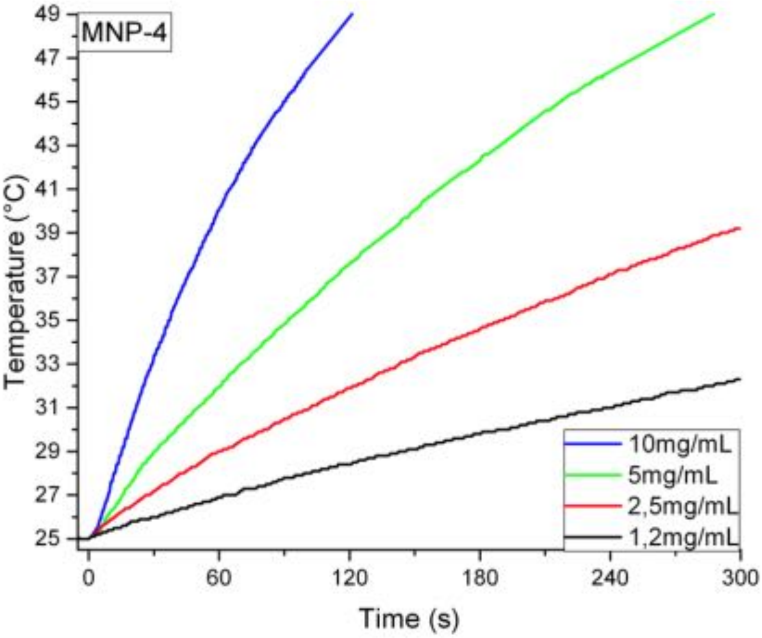

Figure 3. 7: Kinetic evolution of temperature of a MNP-4 water suspension with increasing concentration $1, 2{,}5, 5 \ and \ 10 \ mg/mL$.

$MNP-4$	$SAR\ (Wg_{MNP}^{-1})$
$10mg/mL$	$146{,}8 \pm 5{,}5$
$5mg/mL$	$148{,}5 \pm 8{,}5$
$2{,}5mg/mL$	$152{,}1 \pm 8{,}6$
$1{,}2mg/mL$	$139{,}9 \pm 4{,}8$

Table 3. 3 SAR values obtained for MNP-4 sample suspended at different concentration in $1\ mL$ *of water and exposed for* $300\ s$ *to a AMF (*$183\ kHz, 17\ kAm^{-1}$*); mean values are obtained averaging over 5 data.*

It deserves to be mentioned that MNP-4 has a SAR more than double than MNP-3, a results which confirms the theoretical model discussed above, for which MNPs of same dimension but narrower distribution posses higher SAR. In this case, indeed, MNP-3 and MNP-4 had similar size ≈13nm but slightly different skewness 0,12 and 0,06, respectively, which, as demonstrated figure 3.1 A by the comparison of the 0,05 and 0,01 curves, should produces a difference in SAR comparable to that observed in our case.

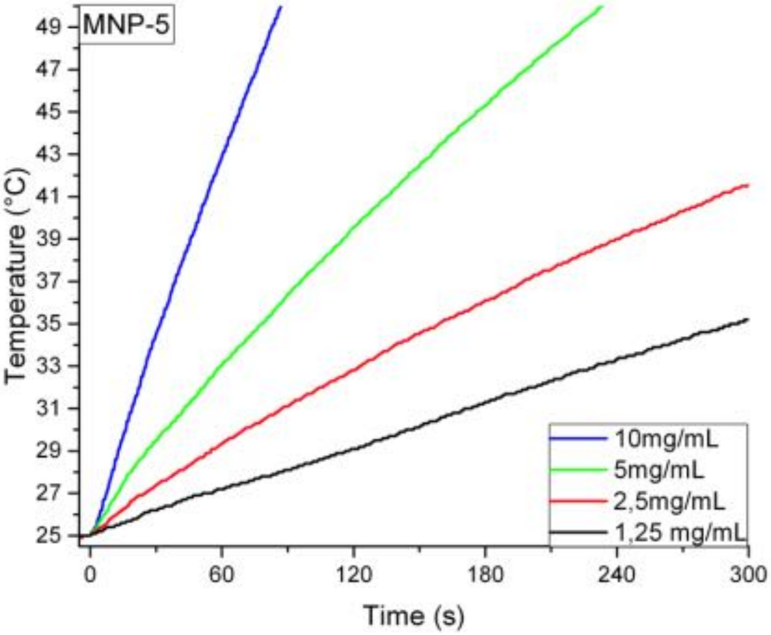

Figure 3. 8: Kinetic evolution of temperature of a MNP-5 water suspension with increasing concentration $(1, 2{,}5, 5\ and 10\ mg/mL)$*.*

MNP-5 exhibits the highest SAR among the three samples, $158{,}6 \pm 4{,}2\mathrm{W/g}$. This result can be ascribed to its higher diameter. In Figure 3.8 are displayed the curves recorded as a function of the concentration, while in table 3.4 the mean value of SAR evaluated at different concentrations are reported.

$\boldsymbol{MNP-5}$	$\boldsymbol{SAR\ (Wg_{MNP}^{-1})}$
$\boldsymbol{10mg/mL}$	$157{,}6 \pm 1{,}7$
$\boldsymbol{5mg/mL}$	$157{,}3 \pm 3{,}9$
$\boldsymbol{2,5mg/mL}$	$161{,}7 \pm 5{,}1$
$\boldsymbol{1,2mg/mL}$	$158{,}2 \pm 5{,}1$

Table 3. 4 SAR values obtained for a MNP-5 sample suspended at different concentration in $1\ mL$ *of water and exposed for* $300\ s$ *to a AMF* $(183\ kHz, 17\ kAm^{-1})$*; mean values are obtained averaging over 5 data.*

In figure 3.9 is shown a comparison of suspensions of the 3 samples at the same concentration ($5\ mg/ml$) to better appreciate their different hyperthermic efficiency.

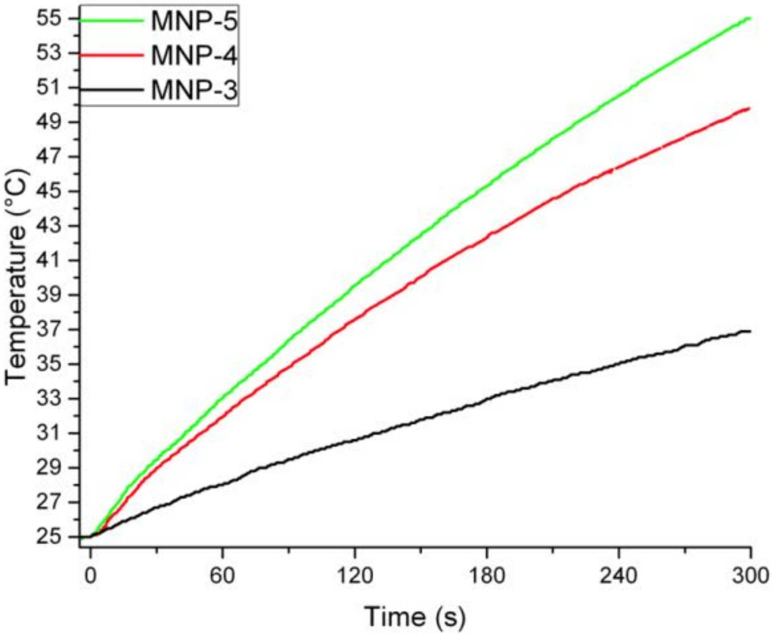

Figure 3. 9: Kinetic evolution of temperature of a $5\ mg/mL$ water suspension of MNPs. MNP-3, black line; MNP-4, red line; MNP-5, green line.

All samples show good SAR values, comparable with those reported in the literature for MNPs used in nanomedicine applications[6,7]. A better comparison with data reported in the literature can be obtained by evaluating the Intrinsic Loss Power (ILP). The ILP parameter is simply the SAR parameter normalized to H^2f and it can be easily derived from heat loss data as $ILP = SAR/H^2f$ (nHm^2kg^{-1})[3,8].

In table 3.5 are reported the ILP values of the three samples at $5\ mg/ml$. They are among the highest ILP values reported in the literature for magnetite MNPs of this size range, as well demonstrated by the comparison with experimental data reported in the literature and theoretical estimation, shown in Figure 3.10[3].

Sample	$ILP\ (nHm^{2}kg^{-1})$
$MNP-3$	1,7
$MNP-4$	3,7
$MNP-5$	4,0

Table 3. 5: ILP values of MNPs calculated normalizing SAR values (W/kg of Iron) by H^2f;$H = 17kAm^{-1}$ *and*$f = 183kHz$.

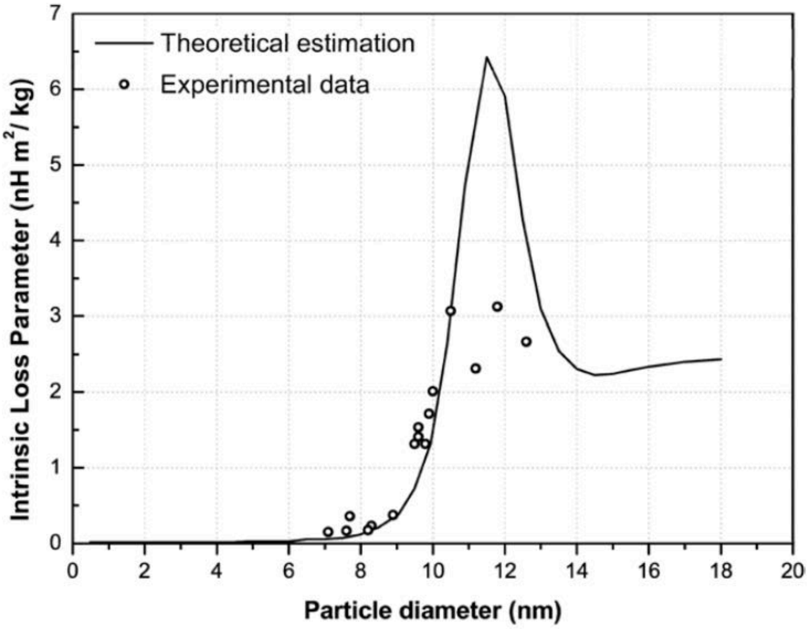

Figure 3. 10: Comparison between theoretical predictions and experimental data on the size-dependent heating efficacy of magnetic fluids, expressed in terms of the intrinsic loss parameter, ILP (nHm^2/kg *of Iron). Image taken from Pankhurst et al.* [3]

3.1.3.3 Hyperthermic efficiency in agarose gel

For MNPs that have to be used for *in vivo* MFH application it is mandatory that hyperthermic properties do not change when they arrive *in situ* inside the tissues and cells. Therefore, as previously mentioned, the reversal of magnetization should be a process mainly governed by Néel relaxation, and should not be affected by environment variables as it would be the case if Brownian relaxation would be the dominant one. To investigate the two relaxation processes separately, we studied the hyperthermic properties of MNPs suspended in agarose gel. By varying the percentage w/w of agarose from $0{,}0\%$ to 4%, we can shift from a medium where the particle are free to rotate (water) to a completely blocked system. At very low percentage (0.25%) the agarose polymer forms a gel which mimes soft tissue, at higher percentage the gel has a density and stiffness similar to human tissues, while around 5% to bones and cartilages.

We choose to suspend the samples in the agarose gel at a concentration that induce significant increase of T, thus reducing the error on SAR evaluation, but that at same time does not overcome the gelling temperature of the agarose gel $(\approx 40 - 52°C)$. This corresponded to $3\, mg/mL$ of magnetic core for MNP-3, while for MNP-4 and MNP-5 to $1\, mg/mL$. The kinetic curves recorded for the agarose samples of MNP-3 are shown in Figure 3.11. They reveal that only at the higher agarose percentage there is a significant change in the hyperthermic efficiency of the MNPs.

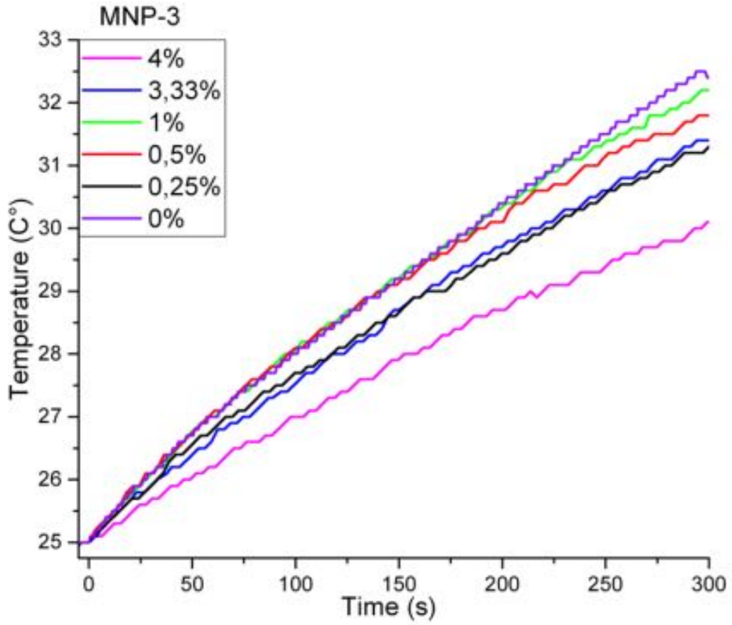

Figure 3. 11: kinetic evolution of temperature of a dispersion of MNP-3 in gel (3 mg/mL), varying the agarose percentage: $\% = 0 - 0{,}25 - 0{,}5 - 1 - 3{,}3\ and\ 4.$

In table 3.6, are reported the mean values of SAR obtained for each samples compared to the ones obtained for the water suspension. Except for the 4% sample, all the others have similar SAR, within the uncertainty of the evaluation. In this case we can conclude that the reversal of the magnetization was mainly not affected by the gel environment at least at concentration lower than 4%.

$MNP-3\ Agar$	$SAR\ (Wg_{MNP}^{-1})$
$\mathbf{0\%}$	$62{,}9 \pm 6{,}1$
$\mathbf{0,25\%}$	$54{,}7 \pm 4{,}8$
$\mathbf{0,50\%}$	$60{,}2 \pm 5{,}4$
$\mathbf{1\%}$	$59{,}9 \pm 6{,}2$
$\mathbf{3,3\%}$	$55{,}4 \pm 1{,}4$
$\mathbf{4\%}$	$34{,}6 \pm 2{,}2$

Table 3. 6: SAR of a a dispersion of MNP-3 in agarose gel (3 mg/mL) at different concentration and exposed for $300\ s$ to an AMF ($183\ kHz, 17\ kAm^{-1}$); mean values are obtained averaging over 5 data.

Same considerations can be drawn from the kinetic curves of sample MNP-4 in agarose gel, shown in figure 3.12. In this case in fact the initial slope for all the sample, and accordingly the SAR values, are the same. However, unlike MNP-3samples, the evolution of temperature changes among the various samples after 60 s of AMF action. Probably, this behaviour is an experimental artefact and can be ascribed to a different positioning of the optic fiber probe inside the volume gel.

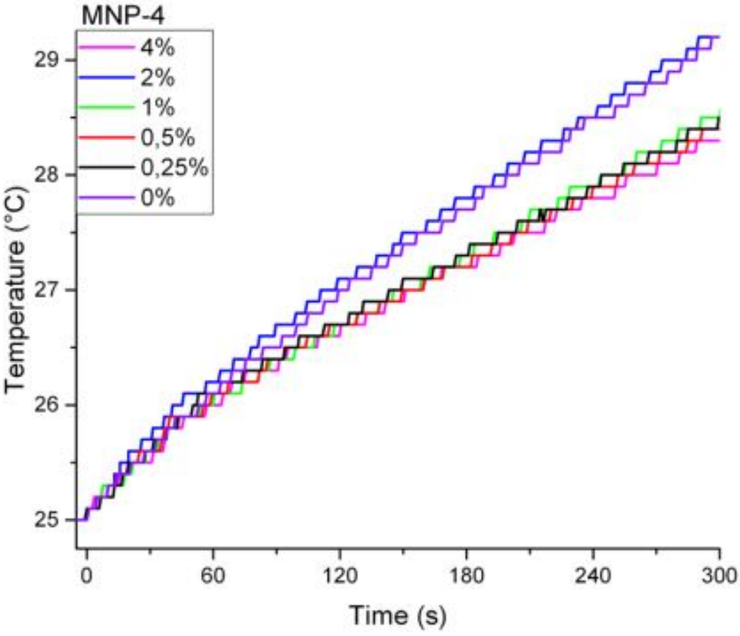

Figure 3. 12: kinetic evolution of temperature of a dispersion of MNP-4 in gel (1 mg/mL), varying the agarose percentage$\% = 0 - 0{,}25 - 0{,}5 - 1 - 2\ and\ 4$

In Table 3.7, is reported the SAR for MNP-4. Again, SAR values are almost the same for all the agarose gel concentrations. Also for this sample the heat efficiency does not vary when the MNPs were blocked in the gel, being hypothesized that a Néel relaxation drives the reversal of the magnetization.

$MNP - 4\ Agar$	$SAR\ (Wg_{MNP}^{-1})$
$\mathbf{0\%}$	$148{,}6 \pm 4{,}2$
$\mathbf{0,25\%}$	$135{,}5 \pm 7{,}5$
$\mathbf{0,50\%}$	$140{,}9 \pm 3{,}3$
$\mathbf{1\%}$	$141{,}7 \pm 4{,}5$
$\mathbf{2\%}$	$147{,}1 \pm 3{,}6$
$\mathbf{4\%}$	$132{,}2 \pm 6{,}6$

Table 3. 7: SAR values obtained for MNP-4 dispersed in agarose gel (1 mg/mL) at different concentrations and exposed for $300\ s$ *to an AMF (*$183\ kHz, 17\ kAm^{-1}$*); mean values are obtained averaging over 5 data.*

Last sample, MNP-5, differs from the previous two, as shown in figure 3.13, where the temperature kinetic curves at different concentration are shown. All the samples in gel have an initial slope significantly reduced compared to that recorded in water at the same concentration. All samples where MNPs are mechanically blocked show a similar behaviour, with no evident dependence on the percentage of agarose used.

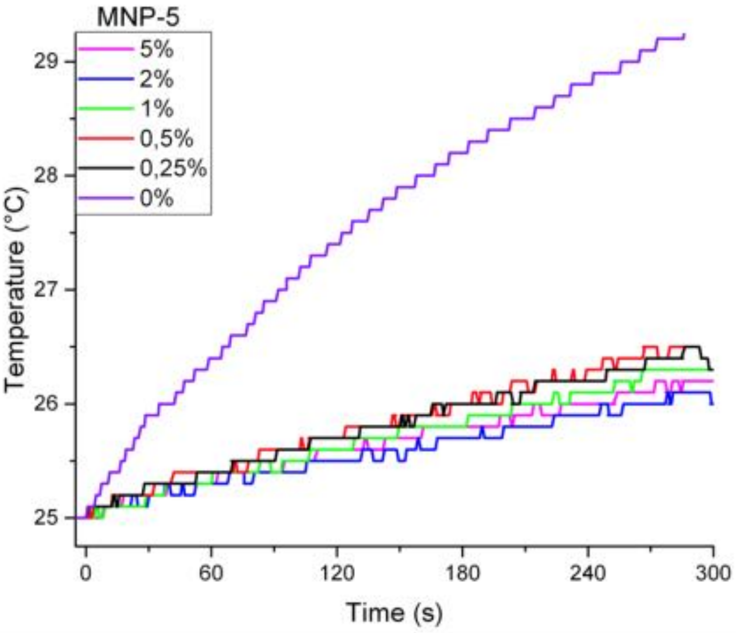

Figure 3. 13: kinetic evolution of temperature of a dispersion of MNP-5 in gel (1 mg/mL), varying the agarose percentage $\% = 0 - 0{,}25 - 0{,}5 - 1 - 3{,}3\ and\ 4$

Accordingly, the SAR of gel dispersions, reported in Table 3.8, are dramatically reduced, by a factor seven, revealing that for MNP-5 the reversal of magnetization in water is dominated by a Brownian relaxation process. This process is indeed hampered by the gel, thus reducing the efficiency of heat release when MNPs are embedded in this medium.

$\boldsymbol{MNP-5\ Agar}$	$\boldsymbol{SAR\ (Wg_{MNP}^{-1})}$
$\boldsymbol{0\%}$	$154{,}7 \pm 7{,}7$
$\boldsymbol{0,25\%}$	$24{,}5 \pm 1{,}8$
$\boldsymbol{0,50\%}$	$26{,}6 \pm 3{,}8$
$\boldsymbol{1\%}$	$22{,}7 \pm 3{,}4$
$\boldsymbol{2\%}$	$17{,}2 \pm 1{,}4$
$\boldsymbol{5\%}$	$20{,}7 \pm 2{,}3$

Table 3. 8 SAR values obtained for MNP-5 dispersed in agarose gel (1 mg/mL) at different concentrations and exposed for $300\ s$ to a AMF ($183\ kHz, 17\ kAm^{-1}$); mean values are obtained averaging over 5 data.

In Figure 3.14 are plotted the SAR for all the samples against the percentages of agarose used, making the different behaviour in agarose gel more explicit. This result is crucial since in the final *in vivo* application the MNPs will be embedded in a strongly viscous environment where no mechanical rotation is allowed. Therefore, although MNP-5 possesses the best hyperthermic efficiency in water suspension MNP-3 and MNP-4 more suited for the functionalization with HFn.

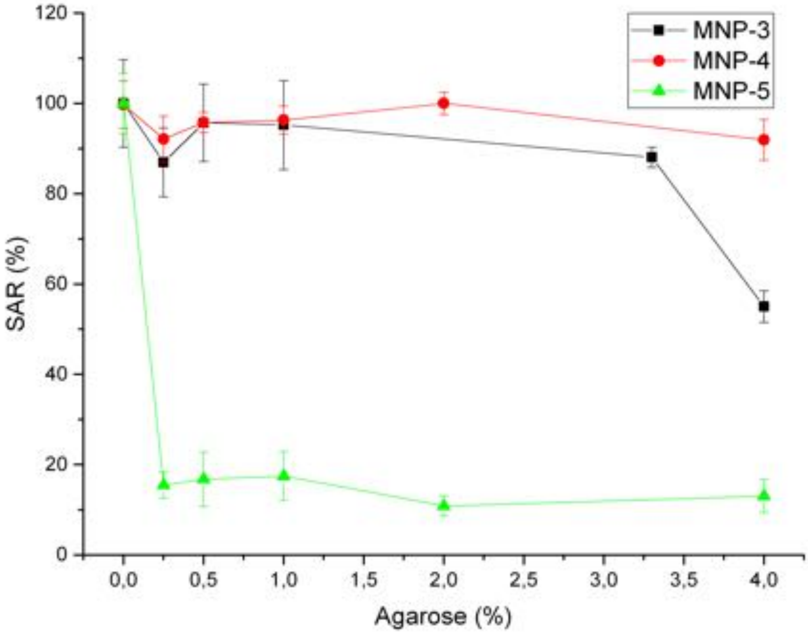

Figure 3. 14: Dependence of SAR on the % of agarose. MNP-3, black symbols; MNP-4, red symbols; MNP-5, green symbols.

3.2 Magnetic Resonance Imaging

3.2.1 Basic principle of Magnetic Resonance Imaging

In a typical Magnetic Resonance Imaging, MRI, experiment the recovery of the magnetization of water ^{1}H nuclei to its equilibrium value, after a perturbation, is used to map the anatomy and physiological process of the body. In a typical NMR experiment a stationary field, B_0, is applied along the direction z, so that the nuclear magnetic moments will precess along the field direction. The macroscopic effect is a non-zero magnetization along z, as the resultant of the sum of the two populations of spins oriented along the two opposing orientations, as shown in Figure 3.15.

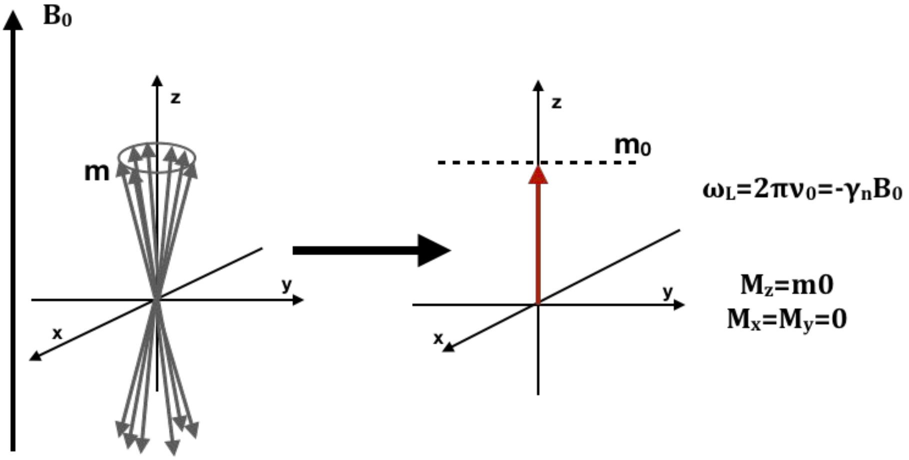

Figure 3. 15: Orientation of a set of spins along the direction of the field, z. The spins rotate at the Larmor frequency ω_L. At the equilibrium, the vector sum of nuclear magnetic moments of protons result in a net magnetization of the sample along the z axis, with $\boldsymbol{M} = \boldsymbol{M}_z$ and $\boldsymbol{M}_x = \boldsymbol{M}_y = \boldsymbol{0}$

Therefore, a set of protons, with nuclear gyromagnetic ratio $\gamma_n = 2{,}67 \cdot 10^8\, rad s^{-1} T^{-1}$, in a field $B_0 = 1\,T$ oscillates with precession motion at frequency $\nu_0 = \omega_L \,/\, 2\pi = 42{,}57\; MHz$. To perturb this system it is necessary to apply an electromagnetic pulse, usually a radiofrequency pulse, perpendicular to B_0 oscillating at the same frequency of proton Larmor precession, ν_0. By means of characteristic sequences of radiofrequency pulse, a coherent rotation of the nuclear spins is induced with the rotation of the magnetization in the plane and the vanishing of the magnetization along z ($\pi/2$ impulse).

When the perturbation is switched off, the system spontaneously recovers the initial equilibrium. The recovery of magnetization along z and the decay in the xy plane are described by the Bloch equations (Figure 3.16):

$$M_z(t) = M_0(1 - e^{-\frac{t}{T_1}}) \tag{9}$$

$$M_{x,y}(t) = M_0(e^{-\frac{t}{T_2}}) \tag{10}$$

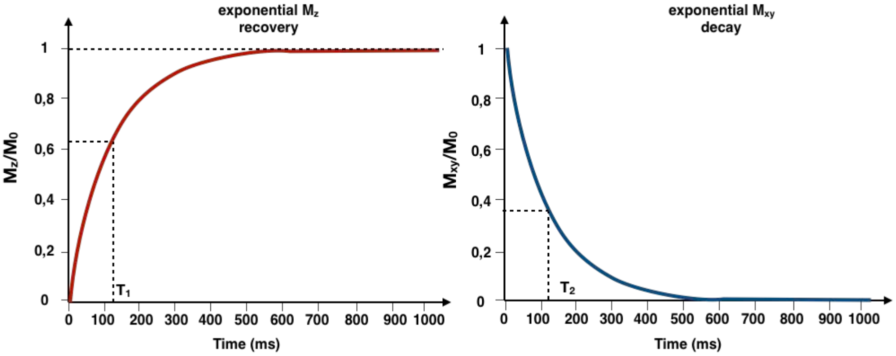

Figure 3. 16: Temporal evolution of the magnetization along the z direction and in the xy plane after a 90° pulse has been applied.

The temporal evolution of the magnetization in z and xy is described by two distinct characteristic relaxation times, T_1 and T_2. T_1, called spin-lattice relaxation time or longitudinal relaxation time, measures how the magnetization M_z comes back to the initial value M_0 and depends on the energy exchange between the spin system and the lattice. When magnetization recovers along z, magnetization in xy plane decays and the evolution of M_{xy} is described by the characteristic time T_2, called spin-spin relaxation time or transverse relaxation time. The relaxation in the xy plane can be faster than the recovery of M_z and is driven by phase coherence loss in the proton precession motions due to magnetic interactions with other protons or with fluctuating magnetic fields generated in their environment (Figure 3.17).

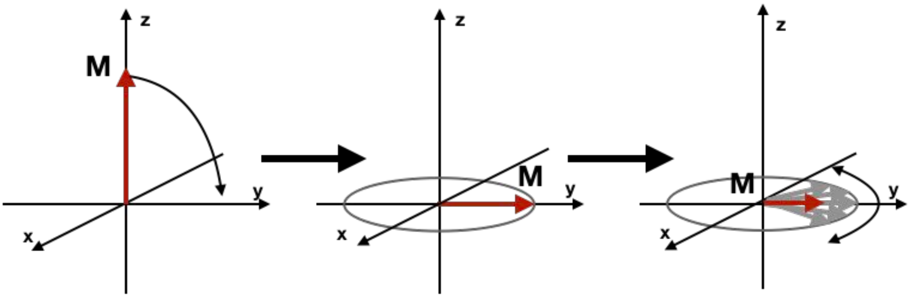

Figure 3. 17: Dephasing of spin after the application of the 90° pulse. The resultant magnetization decreases progressively as the system relaxes, restoring the equilibrium conditions

Actually, signal decay occurs with a characteristic time that may be different from T_2 and is generally indicted as T_2^*.

$$\frac{1}{\mathrm{T}_2^*} = \frac{1}{\mathrm{T}_2} + \gamma \frac{\Delta \mathrm{B}_0}{2}$$

where $\varDelta B_0$ includes inhomogeneity of the applied field B_0, and local variations of the system magnetic susceptibility.

MRI relies on the fact that proton of water molecules in different environment have different relaxation time, to reconstruct a map of the body. The natural contrast can be further enhanced by using exogenous substance, the so-called contrast agents (CAs). Indeed, the presence of magnetic centres dispersed in water creates local field inhomogeneity which modify the relaxation process of water protons. Either MNPs or paramagnetic metals can be used as CAs, as they are able to significantly shorten T_1 and T_2, respectively.

The efficacy of a CA to enhance the contrast is quantified by the relaxivity, defined as the increase of the nuclear relaxation rate of a solvent, water in our case, induced by a concentration $1\,mM$ of a magnetic centre dispersed in it. The relaxivity is expressed in $s^{-1}mM^{-1}$, and it is obtained by the formula:

$$\mathrm{r_i} = \frac{1}{\mathrm{c}}\left(\frac{1}{\mathrm{T_{i_{meas}}}} - \frac{1}{\mathrm{T_{i_{dia}}}}\right)$$

where $i = 1, 2$ indicates longitudinal relaxation or transverse relaxation, $T_{i_{meas}}$ is the relaxation time measured for the sample with the paramagnetic or superparamagnetic agents, $T_{i_{dia}}$ is the relaxation time of the diamagnetic host solution and c is the mM concentration of the magnetic centres.

3.2.2 Analysis of the relaxometric properties of the inorganic cores

The ability of MNP-3 and MNP-4 samples to increase the transverse and longitudinal relaxation of water protons was studied by measuring the Nuclear Magnetic Resonance Dispersion (^{1}H-NMRD). The measurements were performed in the frequency range $0.01\,MHz \leq f \leq 60\,MHz$. The iron concentration of the suspension was evaluated by ICP and found $0.4\,mM$ and $0.6\,mM$ for MNP-3 and MNP-4 respectively. For each measured frequency the samples were previously sonicated to disperse any aggregate eventually formed. The relaxation rates r_1 and r_2 of the two suspensions were normalized for the respective concentrations.

In Figure 3.18 are shown the longitudinal relaxivity ^{1}H-NMRD profiles of the two suspensions. In principle, several information can be extracted from these curves. In figure 3.19 it is shown a typical longitudinal ^{1}H-NMRD relaxation curve for an assembly of small (i.e. $d = 5\,nm$) superparamagnetic MNPs which is well described by the Roche model[9]. In general, the absence or the presence of a dispersion at low field provides information on the magnetic anisotropy of the system. If a low-field dispersion is present, the particle's anisotropy energy is low and therefore its magnetic moment is not blocked along the easy axis. Instead, if the anisotropy energy is much greater than thermal energy, the low field dispersion disappears. At very low field the relaxation rate is led by a zero magnetic field correlation time, which matches τ_N if is much lower than water diffusivity τ_D. At high magnetic fields M_S can obtained from the maximum of r_1. while the inflection point can be used to obtain the crystal size. The fitting to the Roche model of the NMRD profile thus provides an estimate of all the above mentioned parameters.

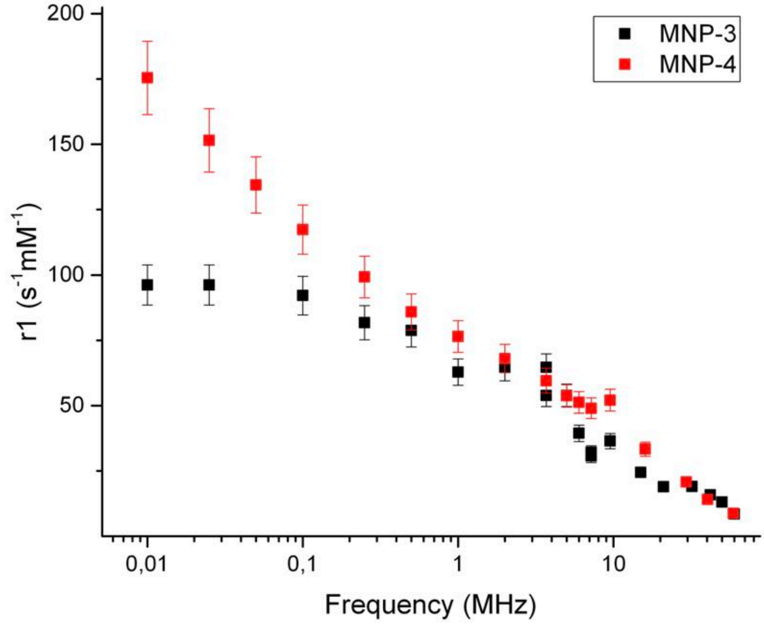

Figure 3. 18: Longitudinal relaxivity NMRD profiles of MNP-3 (black symbols) and MNP-4 (red symbols)

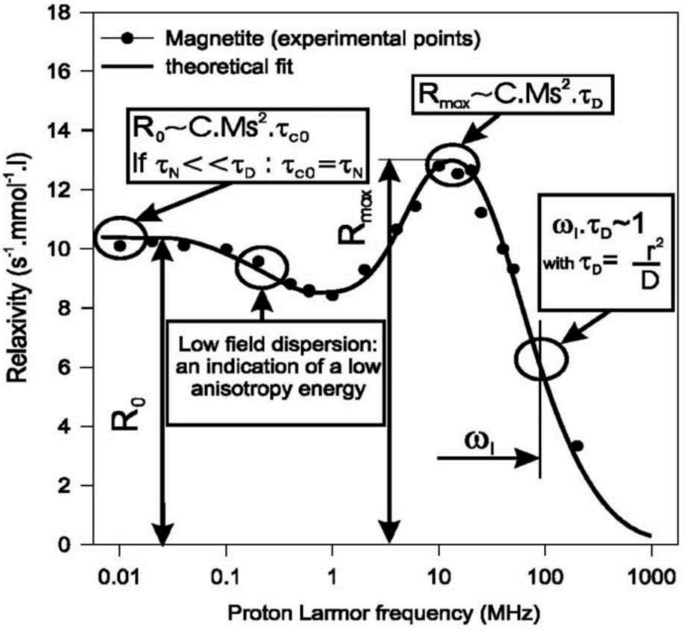

Figure 3. 19: NMRD Profile of longitudinal relaxivity for the proton water relaxation in a colloidal solution of magnetic nanoparticles, with the different parameters that can be derived by the fitting of the curve.

However, in our case neither the experimental ^{1}H-NMRD curve of MNP-3 nor that of MNP-4 follow the expected trend, preventing any attempt to fit the experimental data. This is mostly due to the increasing values of r_1 at low frequencies, which exceed the maximum curve so that only high-frequency dispersion can be seen. The origin of this unexpected behaviour requires a much more detailed investigation which is currently in progress.

The interpretation of the transverse relaxation profile is more complicated. Indeed, there are several and complex models describing the transversal ^{1}H-NMRD curve, whose validity is still under investigation. However, for the purpose of this work it is important to ascertain whether our MNPs have the ability to act as T_2-relaxing agents, that is a sufficiently high r_2 to be used, not only an high efficiency as therapeutic agents (Magnetic Fluid Hyperthermia, MFH), but also an high efficiency as diagnostic agents (Magnetic Resonance Imaging (MRI). To this aim we compared the r_2 values of our samples with those of a reference product, Endorem®, a commercial CAs based on iron-oxide MNPs with a diameter of $4 - 6\ nm$ coated with dextran[10]. The r_2 acquired at the characteristical frequencies used in MRI machine in hospitals are shown in figure 3.20, and for comparison is reported also the mean value measured for Endorem® at high frequency. The transversal relaxation times of both samples are almost 2 times faster than the commercial Endorem®.

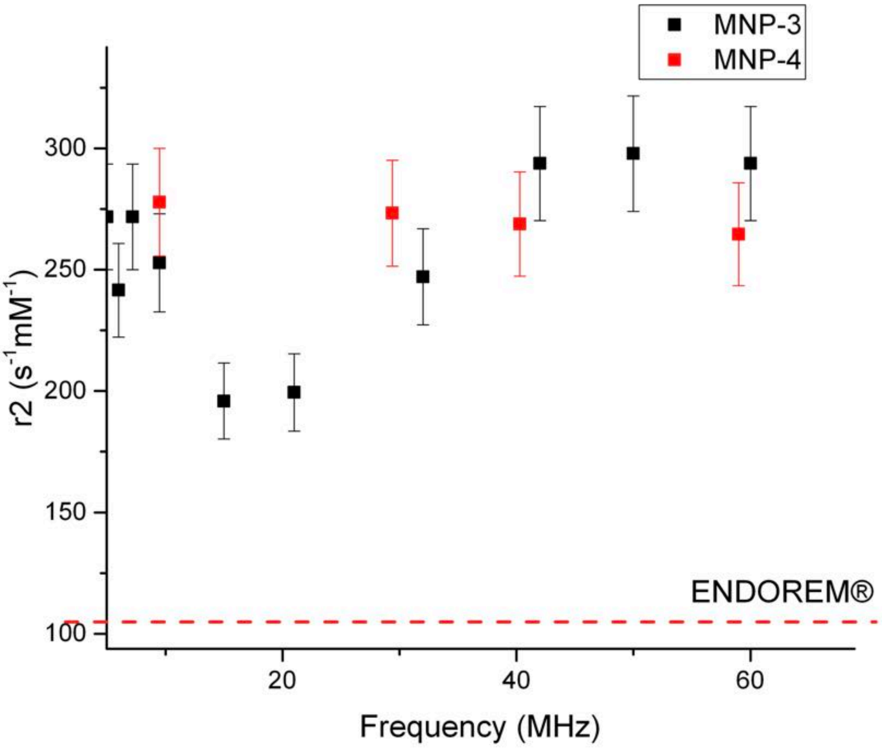

Figure 3. 20: Transverse relaxivity NMRD profiles of MNP-3 (black symbols) and MNP-4 (red symbols) samples. The red dashed line represents the transverse relaxivity mean value of Endorem® at high frequency.

The results obtained are very interesting as they show that our MNPs not only have the ability to increase the relaxivity of water protons, but, in terms of absolute magnitude, they have efficiency up to 2-3 times better than a commercial product such Endorem®. This result, together with the hyperthermia data shown above, demonstrates the possibility of using these MNPs as building block for the realization of theranostic nano-devices in medicine.

1. Cervadoro, A. *et al.* Design Maps for the Hyperthermic Treatment of Tumors with Superparamagnetic Nanoparticles. *PLoS One* **8,** e57332 (2013).

2. Reilly, P. J. *Applied Bioelectricity From Electrical Stimulation to Electropathology*. **28,** (1998).

3. Pankhurst, Q. a, Thanh, N. T. K., Jones, S. K. & Dobson, J. Progress in applications of magnetic nanoparticles in biomedicine. *J. Phys. D. Appl. Phys.* **42,** 224001 (2009).

4. Johansen, M. *et al.* Morbidity and quality of life during thermotherapy using magnetic nanoparticles in locally recurrent prostate cancer : Results of a prospective phase I trial. **23,** 315–323 (2007).

5. Thiesen, B. & Jordan, A. Clinical applications of magnetic nanoparticles for hyperthermia. *Int. J. Hyperth.* **24,** 467–474 (2008).

6. Branquinho, L. C. *et al.* Effect of magnetic dipolar interactions on nanoparticle heating efficiency: Implications for cancer hyperthermia. *Sci. Rep.* **4,** 3637 (2015).

7. Deatsch, A. E. & Evans, B. a. Heating efficiency in magnetic nanoparticle hyperthermia. *J. Magn. Magn. Mater.* **354,** 163–172 (2014).

8. Dutz, S. & Hergt, R. Magnetic particle hyperthermia—a promising tumour therapy? *Nanotechnology* **25,** 452001 (2014).

9. Lascialfari, A., Filibian, M., Sangregorio, C. & Carretta, P. In vivo biomedical applications of magnetic resonance and magnetic materials. *Riv. del nuovo Cim.* **36,** 211–271 (2013).

10. Casula, M. F. *et al.* Magnetic Resonance Imaging Contrast Agents based on Iron Oxide Superparamagnetic Ferrofluids. *Chem. Mater.* 1739–1748 (2010).

4. Assembling the MNP-HFn nano-system

In the previous chapters we have presented the synthesis and characterization of the magnetic cores and the study of their magnetic properties for the use in biomedical applications. In this chapter the synthetic strategy used to functionalize the selected samples with ferritin protein will be described together with the characterization of the chemical-physical properties of the nano-device, MNP-HFn.

The synthesis of the MNP-HFn system was carried out in collaboration with Dr. Pierpaolo Ceci and Dr. Elisabetta Falvo of IMBP-CNR of Rome, which provided us empty human ferritin (Fn) used for the functionalization.

4.1 The Human Ferritin

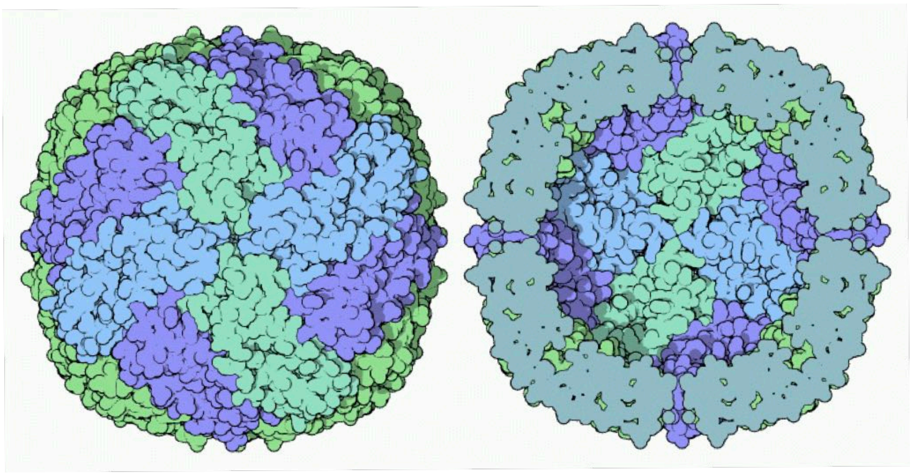

Figure 4. 1 Representation of the ferritin protein structure; different colours corresponds to the subunits assembled in spherical cage of 12 nm of external diameter and 8 nm internal diameter

Ferritin is a highly symmetrical multimeric protein. It consists of 24 subunits that self-assemble into a shell-like shape, with external and internal diameters of 12 and $8\ nm$, respectively, which encloses a hollow cavity deputed to iron storage.

This protein is involved in iron homeostasis, damping the deficiency and excess of iron in the body by a controlled release and accumulation of Fe contained therein. Moreover, ferritins play an important role in the elimination of potentially damaging metallic ions such as: Fe^{2+}, Be^{2+}, Zn^{2+}, Zn^{2+}, $Cd^{2+}$and Al^{3+} [1].

The subunits of ferritin are formed by 5 α-helices. There are two types of subunits with different molecular weight, called heavy (H, $21\,kDa$) and light (L, $19\,kDa$). The ratio between H and L is variable depending on the tissue of the organism considered. H subunits play a key role in detoxifying action. They are the only ones capable of iron oxidation from Fe^{2+}, toxic, to Fe^{3+}. On the surface of the protein shell, at the intersection of the subunits, there are channels that permit iron bio-mineralization. Ferritin cavity may contain a number of atoms ranging from 0 (apo-ferritin) to 4500 atoms per molecule, in the form of Fe oxi-hydroxide NPs. Depending on the tissue, ferritins have a different filling: spleen and liver contain on average 2000-3000 atoms of Fe, heart and brain $1000-2000$, while seldom they are totally filled. The NP of iron oxide stored inside the cavity has a structure that varies from monocrystalline to amorphous, and anti-ferromagnetic properties at low temperature[2].

Recombinant ferritins made of 24 heavy chains (HFn) are endowed with considerable potential for the targeted delivery of drugs and diagnostic agents to cancer cells[3–6] as they offer numerous advantageous, which include biosafety, water and blood solubility, amenability to multi-functionalization, and intrinsic ability to bind tumour cells in an effective and selective way. HFn has a remarkable capacity to entrap different types of molecules as CA for MRI and PET, organic molecules and drugs[7] Importantly, HFn is one of the few nanoparticles that are intrinsically able to effectively and selectively bind tumour cells thanks to its interaction with, and internalization via transferrin receptor 1 (TfR1)[8]. TfR1 is one of the most attractive cancer therapy targets, since it is up-regulated at the surface of many types of cancers. Tumours express up to 100 times higher levels of TfR1 than healthy cells, and actively internalize the

HFn:TfR1 ligand–receptor complex, to accumulate the large amounts of iron required for unrestrained cell growth[3]. This is therefore an attractive basis to selectively deliver HFn carrying toxic payloads to cancer lesions[9]. HFn has another notable feature: it has on the outer surface 72 lysine residues and 24 cysteine residuals, which can be used for chemical conjugation with many elements as antitumor drugs, targeting agents and polyethylene glycol, PEG[8].

4.2 Synthesis of MNP-HFn

The synthetic strategy followed for the MNP-HFn was based on the use of a bi-functional polyethylene glycol (PEG) as a linker to covalently bind on one side the amino groups present on the surface of the MNPs coated with APPA and, on the other side, the –SH thiols exposed on the outer surface of the HFn. As mentioned in the introduction, PEG has also proven to be able to screen activity from the immune system, allowing increased circulation times and *in vivo* stability[10].

The covalent junction between HFn and MNPs coated with APPA, MNPs@APPA was obtained by using the heterobifunctional crosslinker NHS-PEG-MAL, in which the N-hydroxysuccinimide (NHS) ester reacts specifically with free amino groups onto the MNPs side (Scheme 4.1a), and maleimide (MAL) group reacts specifically with the thiol group onto the HFn molecules (Scheme 4.1b). Succinimidyl-[(N-maleimidopropionamido)-dodecaethyleneglycol] ester, $SM(PEG)_{12}$ (Thermofischer), an amine-to-sulfhydryl crosslinkers with soluble polyethylene glycol (PEG) spacer arms, with a $7.5\ kDa$ polyethylene glycol (PEG) spacer was used to improve water solubility of the conjugate, and to minimize possible steric hindrance between MNPs@APPA and ferritin molecules during conjugation.

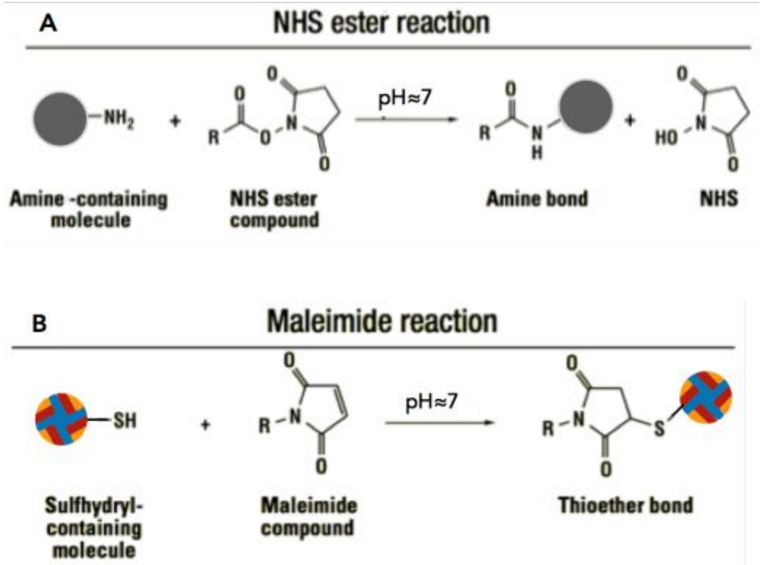

Scheme 4. 1: A) NHS nucleophilic substitution reaction with primary amine; B) scheme of the oxidation reaction of maleimide and thioether formation

Scheme 4.2 illustrates the two-step synthesis process used: first, MNPs@APPA ($0.1\ \mu M$ in amino groups) was reacted with 50-fold molar excess of the crosslinker in PBS (Phosphate Buffer Solution) suspension at pH 7.2 at room temperature, sonicating for 30 min. The unreacted reagent was removed by magnetic precipitation of the MNPs@PEG, which was washed twice with H_2O_{MilliQ}; Secondly, HFn was added ($0.25\ \mu M$) in PBS solution at pH 7.2, and sonicated for $60\ min$. at room temperature allowing the reaction with the MAL groups. The excess of HFn was removed by washing with PBS (10X), then MNP-HFn were magnetically precipitated and washed twice with H_2O_{MilliQ}. Figure 4.16 represents a sketch of MNP-HFn with the detail of the chemical bonds involved in the realization of the system. Thanks to the heat-resistance of ferritin, the so prepared product could be heated up to $50\ ^{\circ}C$ for $30\ min$ before being stored in the fridge at $5\ ^{\circ}C$, to ensure its sterility[11].

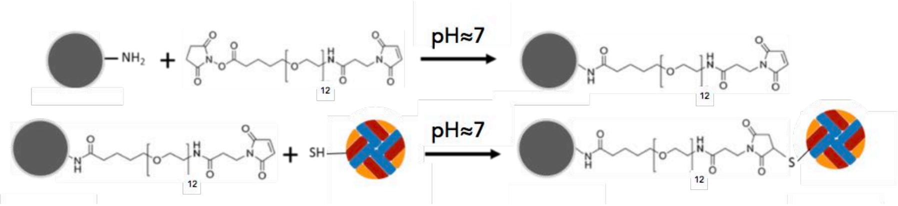

Scheme 4. 2: Scheme of the two - step synthesis: (up) formation of the amide on the surface of the MNP by nucleophilic substitution; (bottom) Ferritin is bound by thiol nucleophilic addition on maleimide

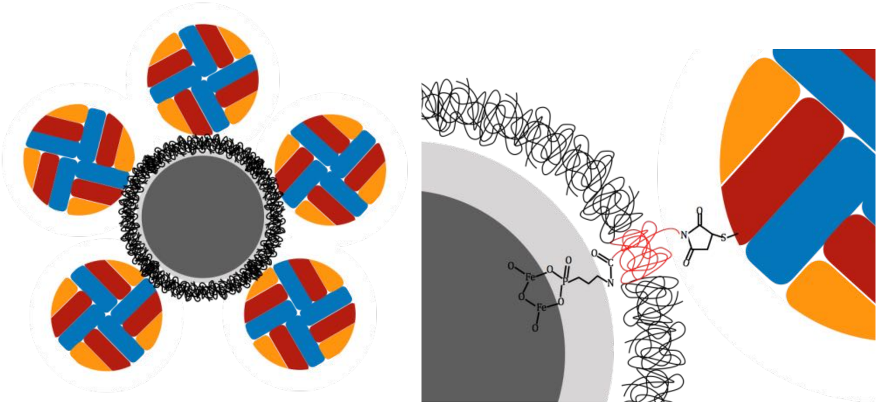

Figure 4. 2: Sketch of the MNP-HFn system and details of the linker between HFn and MNP.

A first control of MNP-HFn formation was performed by electrophoresis on agarose gel. HFn and the synthesis product were run for 2 h on a 1% agarose gel in tris (hydroxymethyl)amminomethane hydrochloride 0.4 M under the action of an 80 V constant electrical field. The gel is then coloured with Kumasi blue to stain the protein and verify the presence of HFn onto the MNPs. Figure 4.3 shows an image of the agarose gel. Reference HFns were free to run to the bottom of the gel, corresponding to the large blue spot, while the MNPs remained at the top of the gel. The blue colour of the MNPs spot confirm the presence of HFns on it, hence confirming the formation of MNP-HFn system.

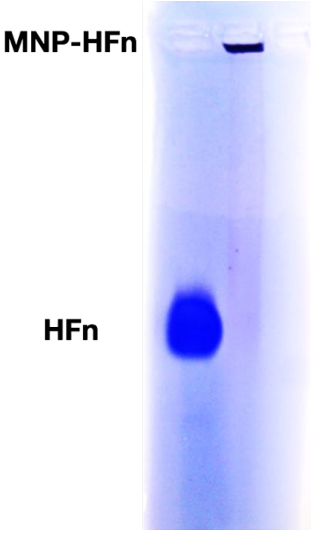

Figure 4. 3: Image of the agarose gel after the protein staining with kumasi blue. MNP-HFn remains at the top of the gel while HFn run down to the bottom.

Further demonstration of the functionalization of MNPs with HFn were given by CHN data (MNP-3-HFn) and ICP data (MNP-4-HFn). These data show that in MNP-3-HFn occurs ca. 30% of organic, while in MNP-4-HFn is ca. 40%. These values correspond approximately to a coverage of 4 and 6 HFn per MNP, respectively.

4.3 Colloidal stability of MNP-FHn

One of the crucial aspects for clinical use of MNPs is their colloidal stability in biological fluids and in cell culture media. Actually, to realize a stable dispersion of MNPs-HFn we had to found proper conditions since, although both MNP and MNP-HFn are perfectly stable in saline and aqueous physiological solutions, where they can be stored for period of time as long as 6 months, in PBS phosphate buffer and in culture media such as Dulbecco high modified medium (DMEM) both MNP and MNP-HFn lose their stability and precipitate in a few minutes. We initially tried to solve this problem by adding non-ionic biocompatible commercial surfactants such as pluronic127 and tween20 but in both cases with unsatisfactory results.

Significant improvement in the stability of the MNP-HFn system resulted from the use of the albumin (BSA) at $5\,\%\,w/w$ solution. The addition of this protein allowed us to greatly improve the stability of the system, extending the stability from a few minutes to several hours.

Using Dynamic Light Scattering (DLS), we estimated the hydrodynamic diameter of MNPs and MNP-HFn systems in water. Figure 4.4 shows the size distribution by volume of MNP-4 samples, while in Table 2.5 the data are summarized. The diameter increases from $24\,nm$ for the MNPs to 70nm for MNP-HFn, while after the addition of BSA, the diameter increase up to 80nm. All samples are characterized by a single distribution and no aggregates were found. These data first of all confirm the actual junction of HFn to MNPs (the diameter increase is in good agreement with that expected for a MNP of $14\,nm$ surrounded by a HFn shell.

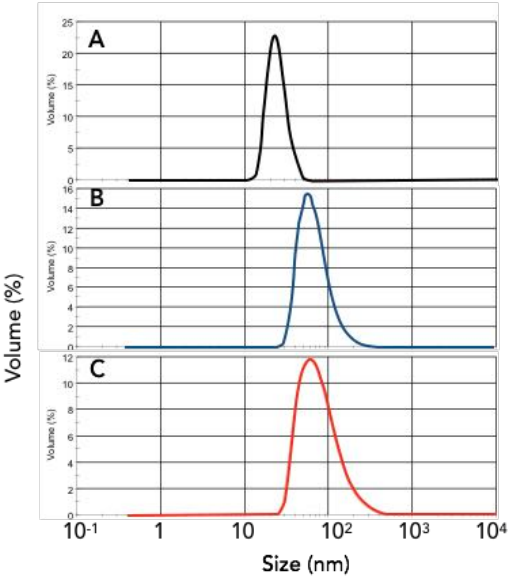

Figure 4. 4: DLS size distribution by volume of MNP-4 (black line), MNP-4-HFn (blue line), and MNP-4-HFn with BSA (red line).

In Table 2.4 are also reported the Z-potential data. No substantial variations for the different samples are observed. The Z-potential of MNPs@APPA and MNP-HFn with and without the BSA is less than $-20mV$.

Sample	d_H	PdI	Z_{pot}
$\boldsymbol{MNP@APPA}$	$24{,}6\ nm$	$0{,}274$	$-26{,}4mV$
$\boldsymbol{MNP-HFn}$	$70{,}4\ nm$	$0{,}168$	$-21{,}3mV$
$\boldsymbol{MNP-Hfn\ BSA\ 5\%}$	$80{,}0\ nm$	$0{,}186$	$-28{,}1mV$

Table 4. 1: DLS data of the water suspensions, d_H hydrodynamic radius; PdI, polydispersivity index; Z_{pot} Z-potential.

We expect that BSA interact with the surface of HFn providing an enhancement of colloidal stability in the culture media. The increased stability can be explained by considering an interaction between the two proteins, BSA and HFn, and with the macromolecular crowding effect. Macromolecular crowding is an effect that occurs in macromolecule suspensions, when the concentration is high enough to cause significant interaction effects, such is the case of protein agglomeration occurring inside the cell and in physiological solutions. Even if counterintuitive this interaction reduces the area of surface that interacts with the solvent, leading to an increase in stability[13,14].

4.4 Atomic force microscopy characterization of MNP-HFn

The formation of the MNP-HFn system was also investigated using atomic force microscopy, AFM[15]. AFM is a high resolution scanning probe microscopy, in which the imaging information is gathered by monitoring the local interaction between the surface of the sample and a tip mounted on deflecting cantilever: attractive (repulsive) interaction lead to a negative (positive) deflection that can be monitored by using a laser shining the back of the cantilever. A piezoelectric based motor guarantees the scan of the selected area of the sample and a feedback loop can be used to maintain constant the interaction by changing the local z position of the sample (this variation directly lead to the local evaluation of the sample height).

The analysis of the prepared samples was performed using the Solver P47-pro setup from NT-MDT, equipped with a silicon tip probe with resonance frequency $206{,}2\ \mathrm{kHz}$ (mod. NSG10 NT-MDT, Russia) operating in tapping mode[16]. In this mode a sinusoidal electrical potential is applied to an additional piezoelectric element directly mounted on the cantilever support in order to allow to excite the oscillation of the cantilever at a frequency corresponding to their resonance frequency. Initially, the tip and cantilever oscillate with a constant amplitude due to the free motion of this system. By approaching the cantilever to the sample, when the interaction between the tip and the sample starts to become relevant but before that the oscillation is completely stopped, an initial reduction in the oscillation amplitude can be detected and this corresponds to the tip "touching" the sample only at the minimum of its oscillation. Tapping mode is operated in these conditions.

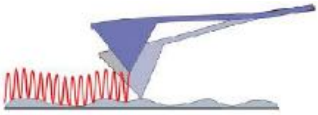

Figure 4. 5: Representation of the resonant AFM tip swing in tapping-mode.

In an ideal situation, from the feedback circuit of the instrument, the height at which the tip is located is measured, giving a direct information on the morphology of the sample. Furthermore, the phase variation in the oscillating motion of the tip, adaptable with this set-up, offers information on the local mechanical properties of the sample, which is related to differences in chemical composition or different stiffness of the material.

We anticipate however that, in the following characterization the AFM system has been used to investigate a highly heterogeneous sample containing different materials with strong differences in the local stiffness and viscosity. These differences cannot be efficiently corrected by the feedback circuitry, thus leading to a complication in the origin of the contrast in the images obtained in both the "height" channel and in the phase contrast that we tentatively attributed to these local alterations.

For the AFM characterization, a drop of an MNP-3-HFn suspension in water was deposited on a freshly exfoliated muscovite mica surface, then the solvent was evaporated under nitrogen flow and the as obtained sample was finally analysed with the AFM.

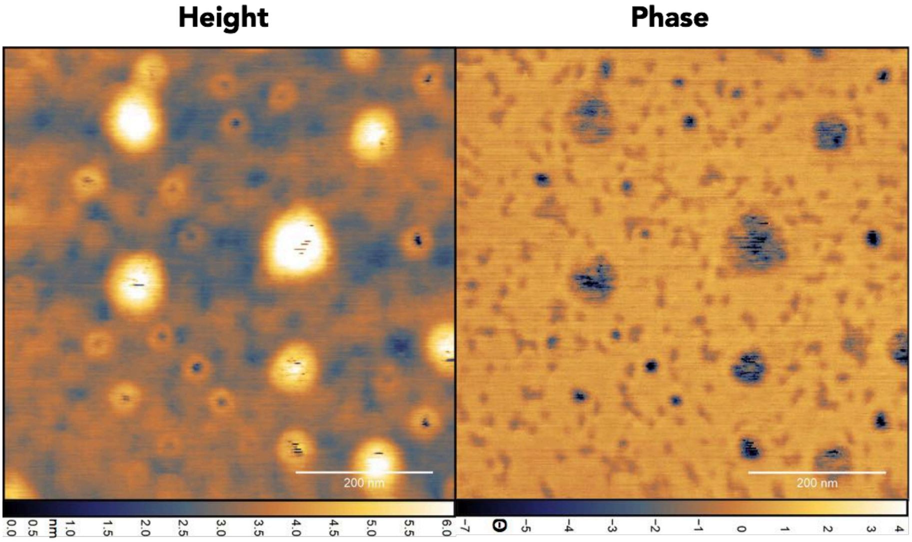

Figure 4. 6: AFM images recorded in tapping mode: on the left, image of the height of a portion of the sample; on the right, image of phase contrast of the sample.

In Figure 4.6 are reported both the “nominal” morphology of the sample and the phase contrast scan. The sample appears homogeneous and includes several spherical objects that could be associated to the MNP-3-HFn system. We notice, however, that the central part of these objects presents a lower height that cannot be easily attributed to a real variation of the sample height. Phase contrast evidences a similar trend: a phase contrast inversion occurs in correspondence of the inner part of the detected spheres.

In these images essentially all the observed MNP-3-HFn features a "donut" structure that can be better clarified by a further magnification and focusing on one of those structures (Figure 4.7) which confirmed that the detected features can be directly attributed to the core-shell structure of the MNP-HFn system.

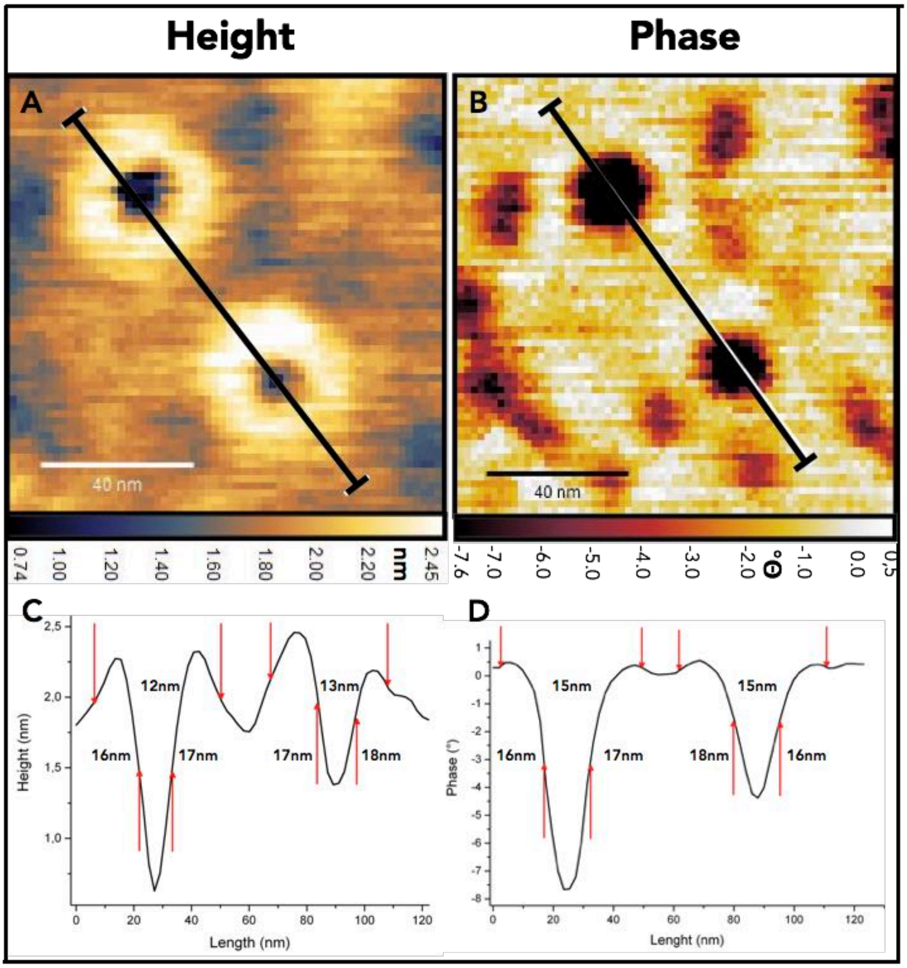

Figure 4. 7: AFM images recorded in tapping mode: A) image of height; B) image of phase contrast; C) lateral profile of a height image; D) lateral profile of a phase contrast image. The red arrows indicate the point used to measure the dimension of MNP core and HFn shell.

We notice that in the morphology (Figure 4.7a) the detected object features a height of $2 \pm 1\, nm$ that is lower than expected for the isolated MNP system. This can be attributed to the presence of an excess of surfactant in the deposited material. This hampers an accurate evaluation of the size of the particles as in an AFM analysis the z-direction is the most relevant since is less affected by problems due to the tip geometry. However, the longitudinal profiles in the morphology (Figure 4.7c) and in the phase scans (Figure 4.7d) are compatible with an inner MNPs of $\approx 15\, nm$ and an HFns external shell of $\approx$

$17\ nm$, in nice agreement, within the resolution limits of AFM, with the size of the inorganic core obtained from TEM investigations, and the value expected for a HFn ($\approx 12\ nm$) plus the PEG linker ($\approx 4\ nm$).

When the phase signal (Figure 4.7b) is studied, a complex situation is confirmed in which the two zones with different local chemical composition can be distinguished, even if with a lower resolution: the inorganic nucleus, detected as a negative dephasing with size of $\approx 15\ nm$ (Figure 4.7d), appears completely surrounded by a positive dephasing signal with size $\approx 17\ nm$. Hence, the high phase contrast, $> 8°$ between the inside and outside of the particle, and the donut structure highlighted in "height" gives us a confirmation on the formation of an outer HFn shell that covers the MNP.

The study of the height and phase profiles of the MNP-HFn system, was extended to several MNP-HFns, so as to make a statistical analysis. The mean values obtained for MNPs, HFns and MNP-HFn are reported in table 4.2. In figures 4.8 and 4.9 are shown the histograms of the data collected from the height image profiles and the phase image profiles, respectively. The size distribution of the MNPs and the shell are narrow and the values fall in the expected range, confirming that all the MNPs analysed were uniformly covered with a shell of PEG-HFn.

	$\boldsymbol{d_{core}\ MNP}$	$\boldsymbol{d_{shell}\ PEG-HFn}$	$\boldsymbol{d_{Tot}\mathrm{MNP}-\mathrm{HFn}}$
Height	$12{,}9 \pm 1{,}6\ nm$	$18{,}0 \pm 1{,}5\ nm$	$48{,}2 \pm 2{,}2\ nm$
Phase	$12{,}7 \pm 1{,}9\ nm$	$17{,}2 \pm 1{,}6\ nm$	$47{,}8 \pm 2{,}8\ nm$

Table 4. 2: Diameter measured from AFM image, averaging over 220 data for Hfn, 110 for MNP and MNP-HFn.

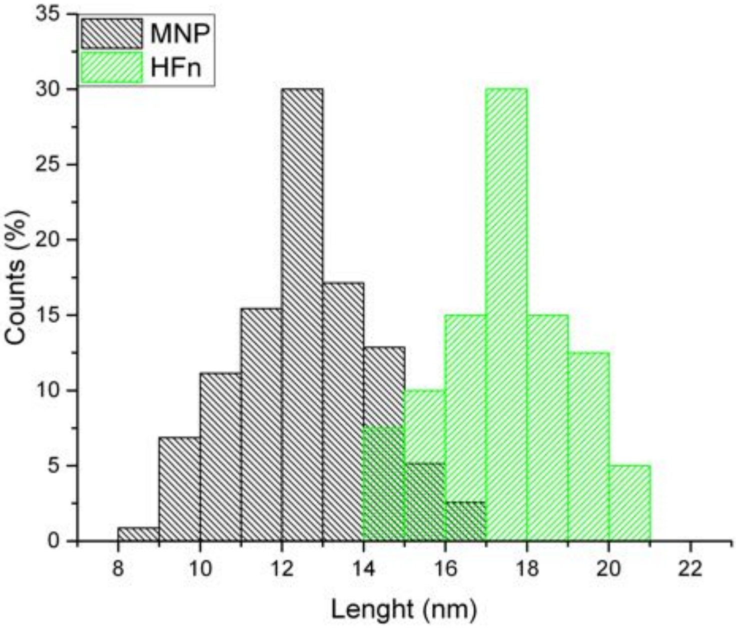

Figure 4. 8: Histogram of size distribution of MNP cores and HFn shells measured from "height" images

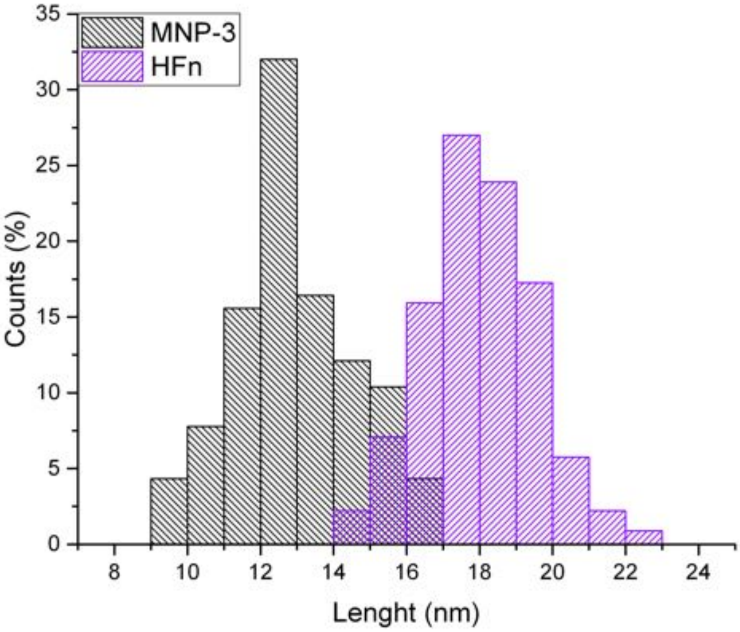

Figure 4. 9 histogram of size distribution of MNP core and HFn shell measured from "phase" images.

4.5 Magnetic behaviour of MNP-HFn

The magnetic properties of the inorganic core were again controlled after the functionalization with HFn, in order to verify that no changes occurred. In figure 4.10 are shown the hysteresis loop and a magnification of the low field region of MNP-3 and MNP-3-HFn samples. No significant changes were observed in the magnetic behaviour apart for decrease of M_S of about 25% after the functionalization due to the increased amount of organic material. This value is in agreement with CHN data.

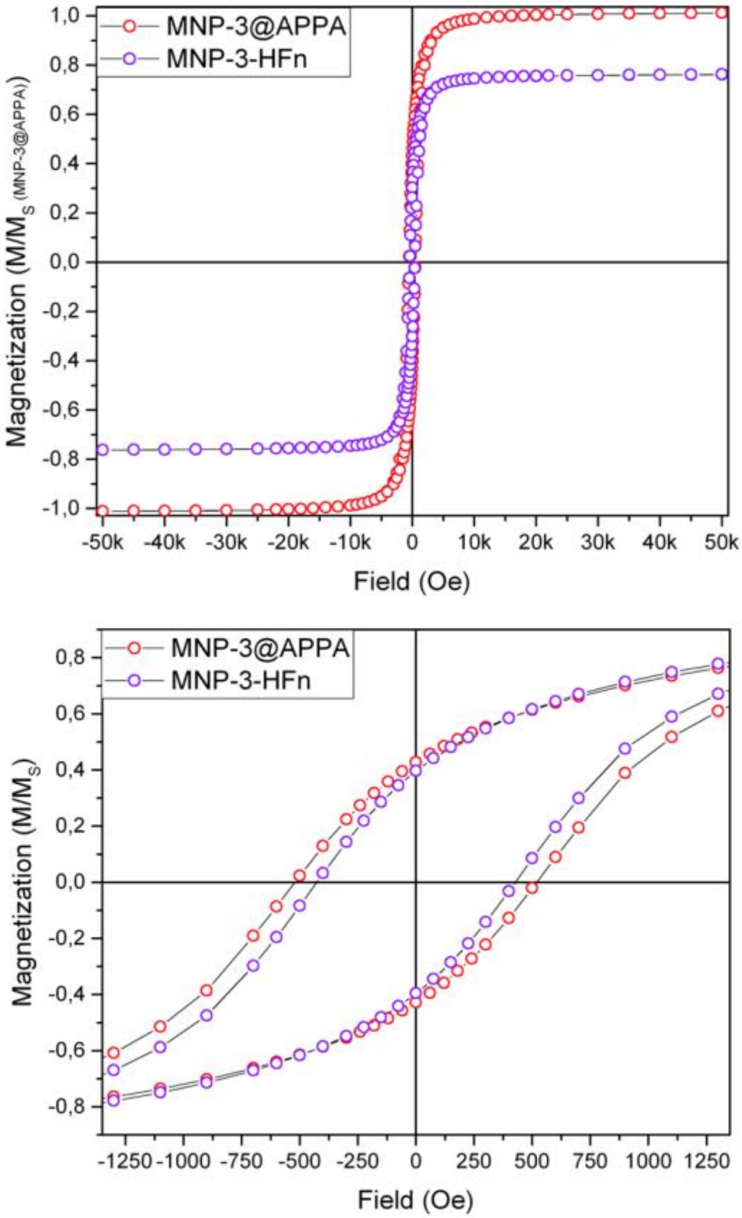

Figure 4. 10: Hysteresis loop recorded at low temperature (2,5 K): (Upper panel) Curve normalized to M_s of MNP-3@APPA; (lower panel) detail at low field normalized to M_s. MNP-3@APPA (red circles), MNP-3-HFn (purple circles).

A similar situation was observed for MNP-4-HFn: the hysteresis loop recorded at low temperature does not reveal significant change in the magnetic behaviour after functionalization. In this case the reduction in Ms confirms the amount of organic shell is ca. 40% in weight.

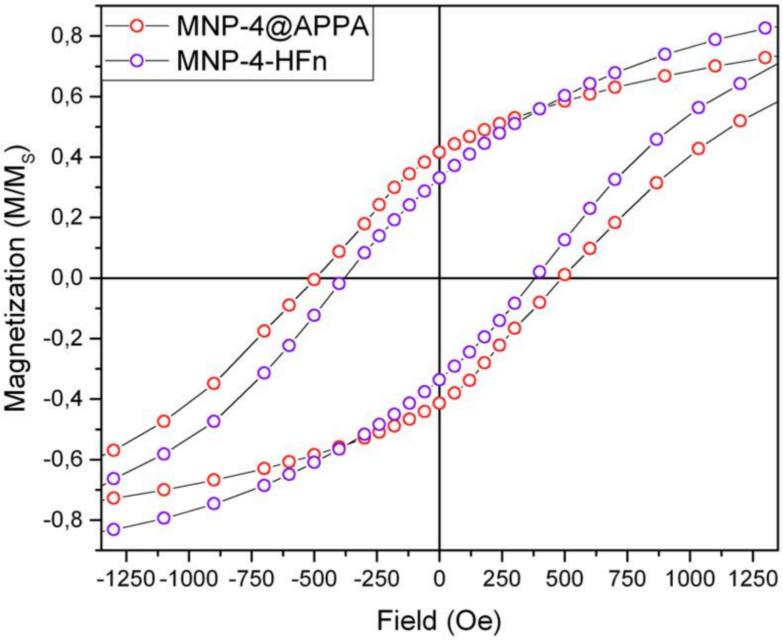

Figure 4. 11: Hysteresis loop recorded at low temperature (2,5 K), detail at low field normalized to M$_s$. MNP-4@APPA (red circles), MNP-4-HFn (purple circles).

4.6 Relaxometric behaviour of MNP-HFn

Finally, we checked the relaxation properties of MNP-3 and MNP-4 samples after the functionalization with HFn. In figures 4.12 and 4.13, are shown the 1H-NMRD r_1 profiles recorded for the two sets of samples.

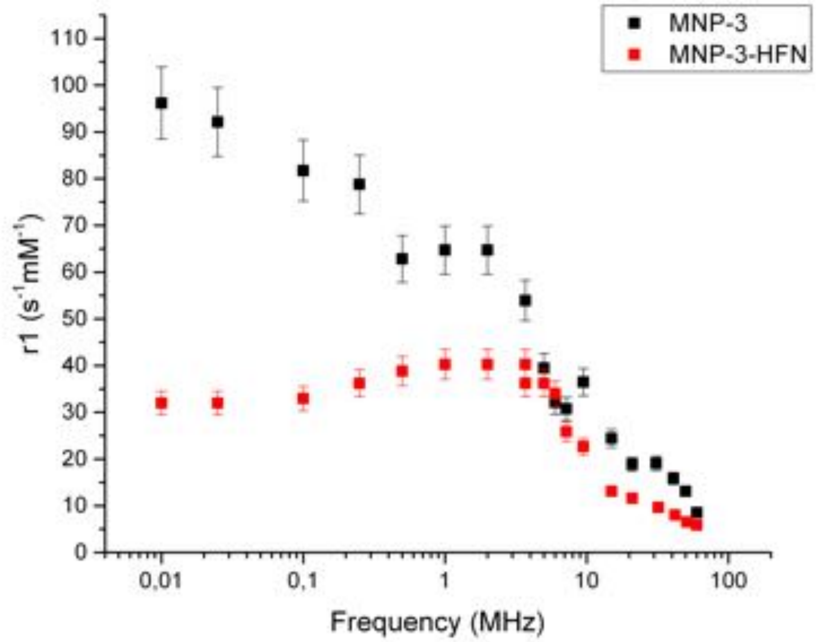

Figure 4. 12: : Longitudinal relaxivity, R, NMRD profiles of MNP-3 (black symbols) and MNP-3-HFn (red symbols)

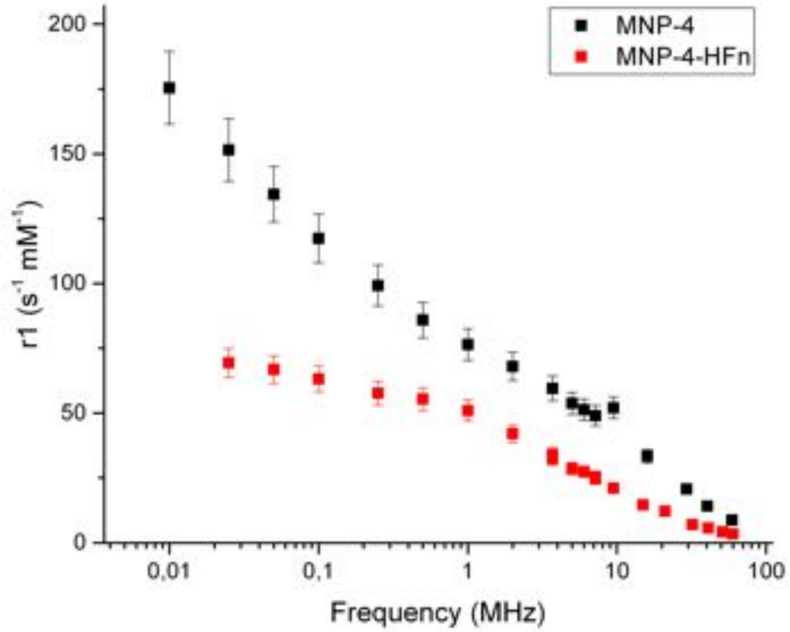

Figure 4. 13: : Longitudinal relaxivity, R, NMRD profiles of MNP-4 (black symbols) and MNP-4-HFn (red symbols)

Both sample display a similar behaviour. The conjugation with HFn reduces the longitudinal relaxivity at low frequency. In the case of MNP-3-HFn sample, the reduction is such that the dispersion is observed, as described in chapter 3.2.2. A decrease of r_1 values at low frequency is commonly related to a change in the anisotropy, but, in our case, the magnetic data do not reveal a change of anisotropy. Hence, the reduction of r_1 valuees at low frequency should be rather attributed to other causes, which are at present under investigation.

In Figures 4.14 and 4.15 are shown the H-NMRD relaxation r_2 profiles recorded for the two sets of samples and for comparison is reported also the mean value measured for Endorem® at high frequency.

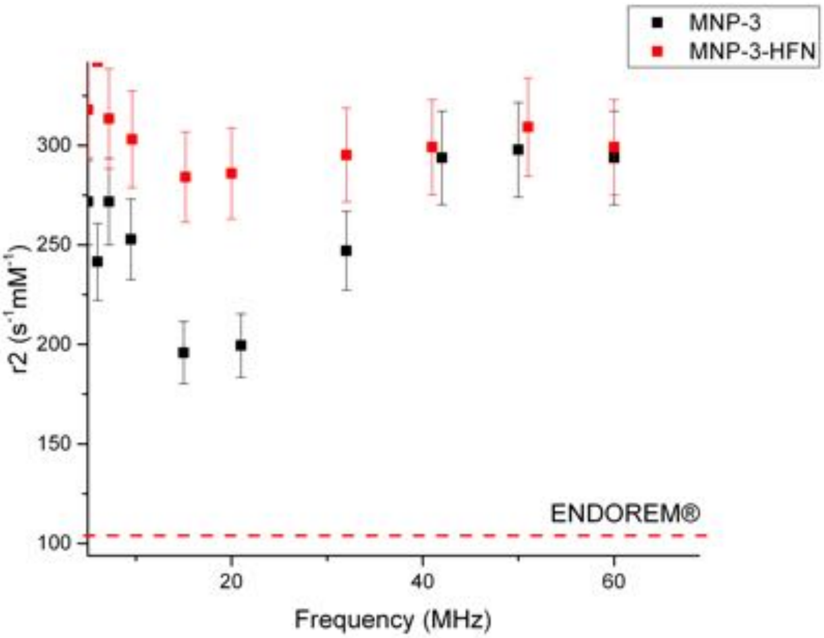

Figure 4. 14: Transverse relaxivity, R, NMRD profiles of MNP-3 (black symbols) and MNP-3-HFn (red symbols) samples. The red dashed line represents the transverse relaxivity mean value of Endorem® at high frequency.

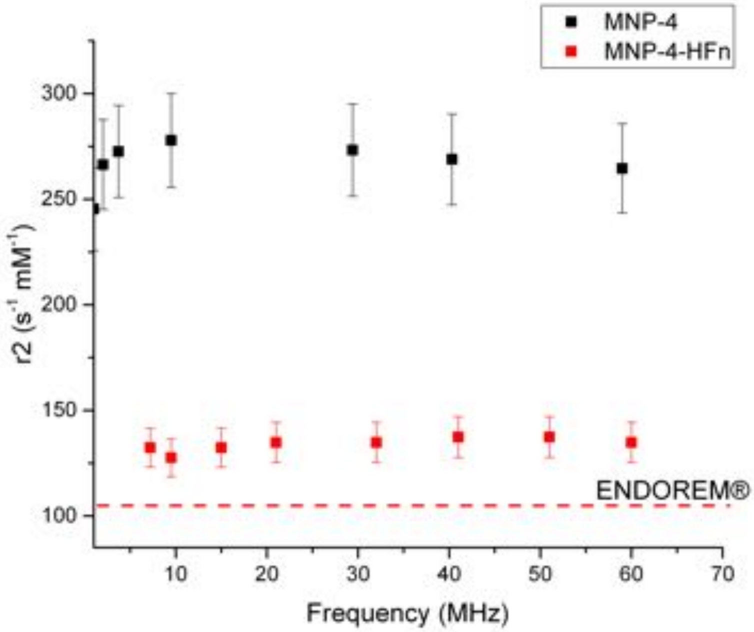

Figure 4. 15: Transverse relaxivity, R, NMRD profiles of MNP-4 (black symbols) and MNP-4-HFn (red symbols) samples. The red dashed line represents the transverse relaxivity mean value of Endorem® at high frequency.

In this case the two samples have a completely different behaviour. For MNP-3-HFn the relaxivity remains almost unchanged, around $300\ s^{-1}mM^{-1}$, while the MNP-4-Hfn r2 relaxivity decreases drastically from $280\ s^{-1}mM^{-1}$of MNP-4 to $130\ s^{-1}mM^{-1}$. To explain this different behaviour it should be emphasized that at high frequencies the value of r_2 is strictly dependent on the minimum approach distance. Even if the DLS data give hydrodynamic similar radii for the two samples magnetic measurements, ICP and CHN revealed that MNP-3-HFn is coated by ca. 4 HFn while MNP-4-by approximately 6 HFn. Since MNP-4-HFn is coated by a larger number of HFn water, on average remains at a higher distance from the magnetic core, producing a decrease of $r_2$values.

However, in terms of absolute transversal relaxivity, all samples are promising for biomedical application as T_2 CAs. Both set of samples in fact have a r_2 relaxivities larger than ENDOREM®, (3 times larger MNP-3-HFn and 1.5 times MNP-4-HFn).

In conclusions, the results obtained by the different techniques, gave a positive feedback about the realization of the desired product. The electrophoresis confirmed the presence of HFn linked to the MNP, DLS analysis demonstrated the colloidal stability of the water suspension and gave a hydrodynamic diameter compatible with the ones expected for the MNP-HFn system. Finally, by AFM analysis we obtained a topographic image of the MNP-HFn, providing a further proof of the success of the synthesis. We thus proceeded with the *in vitro* and *in vivo* test to verify the anti-tumour efficacy in MFH treatments, that will be described in Chapter 5.

1. Li, C. *et al.* A ferritin from Dendrorhynchus zhejiangensis with heavy metals detoxification activity. *PLoS One* **7,** e51428 (2012).
2. Mann, Webb, John. Williams, Robert J.P., S. in 257–341 (1989).
3. Falvo, E. *et al.* Antibody-drug conjugates: targeting melanoma with cisplatin encapsulated in protein-cage nanoparticles based on human ferritin. *Nanoscale* **5,** 12278–12285 (2013).
4. Blazkova, I., Nguyen, H. V., Dostalova, S., Kopel, P. & Stanisavljevic, M. Apoferritin Modified Magnetic Particles as Doxorubicin Carriers for Anticancer Drug Delivery. 13391–13402 (2013). doi:10.3390/ijms140713391
5. Vannucci, L. *et al.* Selective targeting of melanoma by PEG-masked protein-based multifunctional nanoparticles. *Int. J. Nanomedicine* **7,** 1489–509 (2012).
6. Zhang, L. *et al.* H-Chain Ferritin : A Natural Nuclei Targeting and Bioactive Delivery Nanovector. (2015). doi:10.1002/adhm.201500226
7. Falvo, E. *et al.* Improved Doxorubicin Encapsulation and Pharmacokinetics of Ferritin – Fusion Protein Nanocarriers Bearing Proline, Serine, and Alanine Elements. (2016). doi:10.1021/acs.biomac.5b01446
8. Fan, K. *et al.* Magnetoferritin nanoparticles for targeting and visualizing tumour tissues. *Nat. Nanotechnol.* **7,** 459–64 (2012).
9. Fracasso, G. *et al.* Selective delivery of doxorubicin by novel stimuli-sensitive nano-ferritins overcomes tumor refractoriness. **239,** 10–18 (2016).
10. Barreto, J. *et al.* Nanomaterials: applications in cancer imaging and therapy. *Adv. Mater.* **23,** H18–H40 (2011).

11. Fantechi, E. *et al.* A Smart Platform for Hyperthermia Application in Cancer Treatment : Cobalt-Doped Ferrite Nanoparticles Mineralized in Human Ferritin Cages. 4705–4719 (2014).

12. Armstrong, J. K., Wenby, R. B., Meiselman, H. J. & Fisher, T. C. The Hydrodynamic Radii of Macromolecules and Their Effect on Red Blood Cell Aggregation. *Biophys. J.* **87,** 4259–4270 (2004).

13. Ellis, R. J. & Ellis, R. J. Macromolecular crowding : obvious but underappreciated. **26,** 597–604 (2001).

14. Mittal, S., Chowhan, R. K. & Singh, L. R. Macromolecular crowding : Macromolecules friend or foe. *BBA - Gen. Subj.* **1850,** 1822–1831 (2015).

15. Binnig, G. & Quate, C. F. Atomic Force Microscope. *Phys. Rev. Lett.* **56,** 930–933 (1986).

16. Hoper, R., Gesang, T., Possart, W., Hen~emann, O.-D. & Boseck, S. Imaging elastic sample properties with an atomic force microscope operating the tapping mode. *Ultramicroscopy Elsevier Sci.* **60,** 17–24 (1995).

5. Investigation on theranostic efficacy of MNP-HFn

In the above chapters the criticalities related to the realization of a platform for theranostic application in the therapy of tumours based on the exploitation of superparamagnetic MNPs, have been discussed. Then, we have presented the synthesis and characterization of a hybrid system obtained through the functionalization of an iron oxide magnetic core with Human Ferritin. The results analysed so far have shown that the MNP-HFn system possesses the proper dimensional, chemical-physical, magnetic, hyperthermic and relaxometric properties, and also are stable in physiological media, which is a fundamental requirement for the application as heat mediator in MFH. In this chapter we present the results of an investigation aimed to test the antitumor efficacy of our product in MFH treatments, using a procedure based on the common specifications reported in the literature.

Thanks to the collaboration with two different research groups we have been able to test the efficacy of our product both *in vitro* and, preliminary, *in vivo* for the treatment of tumours by MFH. In the first paragraph of this chapter we will discuss the results obtained from *in vitro* MFH treatments on three human cancer cell lines, performed in collaboration with Prof. Carla Ghelardini, Dr. Lorenzo di Cesare Mannelli and Mr.s Barbara Tenci at the laboratory of Pharmacology and Toxicology, Dipartimento di Neuroscienze, psicologia, area del farmaco e della salute del bambino (NEUROFARBA). In the following paragraphs the preliminary results of *in vivo* treatments on cavies carrying breast tumours, performed in collaboration with Prof. Zulmira Lacava and Mr.s Danyelle A. Ferreira at the laboratory of Instituto de Ciências Biológicas of the University of Brasilia, will be presented.

5.1 *In vitro* MFH experiment

The experiments described in this chapter have been performed on human tumour cells, in particular on cell lines PC-3, prostate cancer and MDA-MB-231, breast cancer. There are several reasons behind the choice of these cell lines for our experiments. First of all, the selected cell lines are extremely relevant since they account for 25% of all cancer cases found annually, and in particular the PC-3 and MDA-MB231 are the tumours with the highest incidence on men and women, respectively[1]. Second, these cell lines are the typical model used for the xenografted study of the corresponding tumour tissues. Most importantly, all these cells have the ability to internalize human ferritin via the transferrin receptor, Tfr1, which is over-expressed by some types of cancer cells, including those selected in this work. A high degree of internalization is, in fact, a factor considered relevant in the mechanism of induction of apoptosis by magnetic hyperthermia[2].

All the cancer cell lines were provided by American Type Culture Collection (ATCC): PC-3 was initiated from bone metastasis of a grade IV prostate adenocarcinoma from a 62 years old male Caucasian, while MDA-MB-231 was mammary gland / breast adenocarcinoma derived from metastatic site collected from a 51 years old female patient[3].

5.1.1 Preliminary Analysis

Before performing MFH experiments, it is necessary to carry out some preliminary tests, to verify the selected cell lines are responsive to HFn and that they are able to internalize both HFn and MNP-HFn. Secondly, it is necessary to ensure that MNP-HFns are effectively biocompatible and do not significantly modify cell viability.

In Figures 5.1, and 5.2, are reported images of the two cell lines, taken at the fluorescence microscope, after 1h of incubation with HFn labelled with rhodamine (HFn-Rdh) provided by Dr. Ceci. Rhodamine is a fluorescent dye widely used as a tracer in biological applications since it can be easily detected by fluorescence microscopy ($\lambda_{ex} = 550\ nm; \lambda_{em} = 580\ nm$). The optical channel images were combined with the fluorescence ones, and at the fluorescence signal is assigned the red colour. In the images collected for MDA-MB-231 and for PC3, the presence into the cells of many fluorescent organelles is clearly observed, thus revealing that these two cell lines not only recognize HFn, but during the incubation they internalize large amount of apoferritins, which are probably confined into endosomes and lysosomes, as reported in the literature[4].

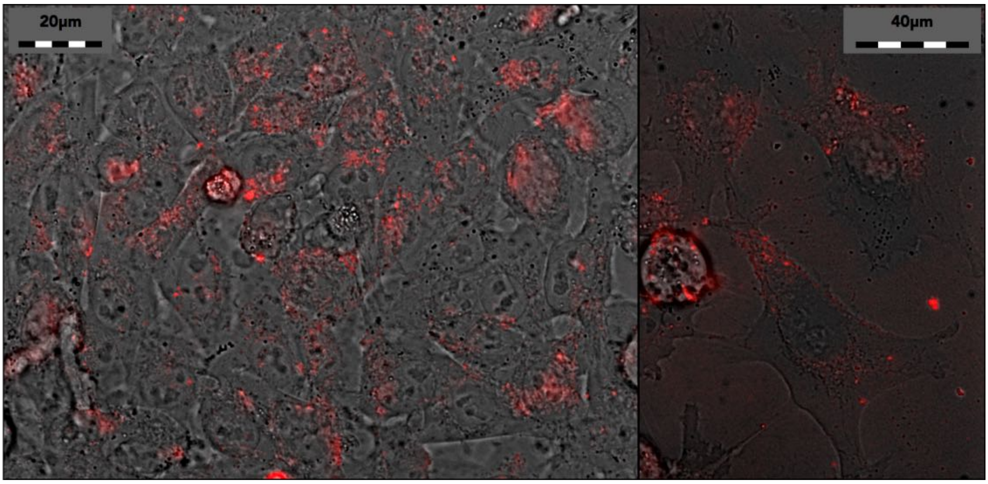

Figure 5.1: Fluorescence microscope images of MDA-MB-231 cancer cells after 1h of incubation with HFn-Rhd $1\ mg/ml$

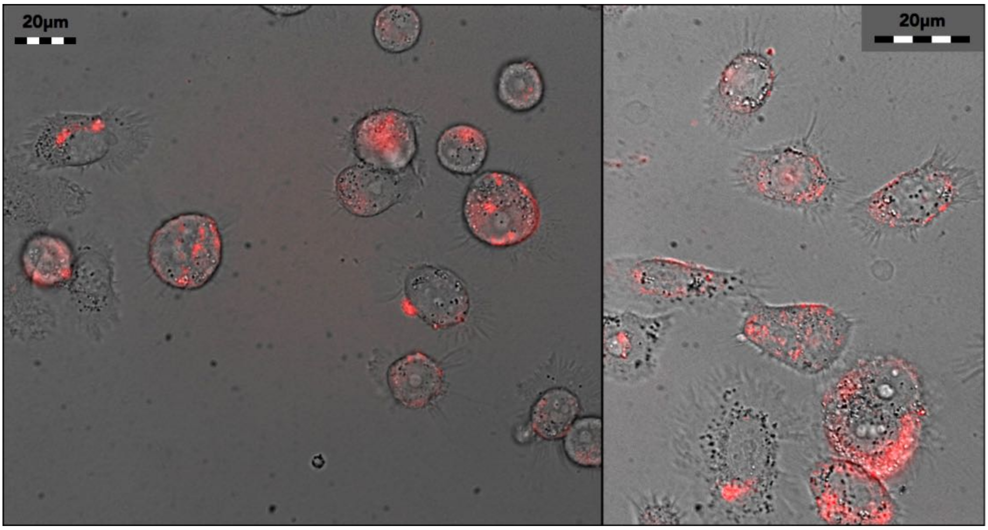

Figure 5.2: Fluorescence microscope images of PC-3 cancer cells after 1h of incubation with HFn-Rhd $1\ mg/ml$

The second preliminary characterization was to test the potential toxicity of MNP-HFn on the cells. To this aim the cell lines underwent the same procedure used for MFH *in vitro* experiment, which will be described in the next chapter, and the cell viability was investigated at two characteristic time steps: after 2h from the begin of the experiment, which corresponds to the time required for incubation plus that of exposure to AMF, and after $48\ h$ from the beginning of the experiment, that is the time required to verify the thermal damages suffered by the cells. The viability of cells treated with MNP-HFn was compared to control samples using two different essays: after $2\ h$ from the beginning of the procedure using the Trypan blue cell count, while at the end of the experiment with the MTT test. Figure 5.3 (up) shows the number of vital cells, as percentage of the control for the two cell lines, at the concentrations of $3\,mg/mL$ and $1\,mg/m$L after $2\,h$. For both cell lines and both concentrations we did not observe any mortality. This result was confirmed by MTT vitality test shown in Figure 5.3 (bottom), which shows how after $48\ h$ from the treatment, the cells possess a vitality comparable to the control samples. The biocompatibility of the MNP-HFn system proved by this data ensures the validity of the results obtained in the MFH experiments that will be shown later.

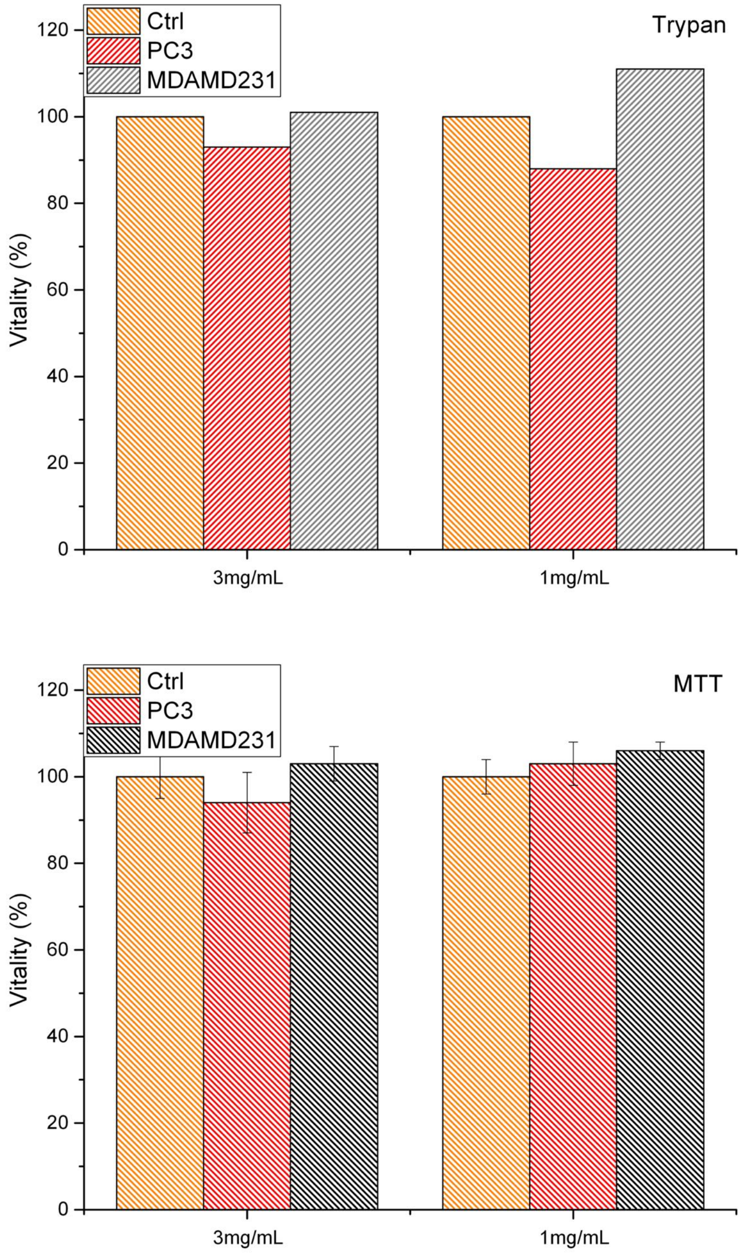

Figure 5.3: (upper panel) Number of living cells counted at Trypan blue assay for PC-3 and MDA-MB-231 cell samples, after the incubation with MNP-HFn. (lower panel) MTT cellular vitality values 48h after the incubation with MNP-HFn. Each value is normalized to the corresponding control sample.

5.1.2 Analysis of the internalization of PC-3 and MDA-MB-231 cell lines

We have proved that PC3 and MDA-MB-231 cell lines are able to internalize HFn and do not suffer in the presence of MNP-HFn. Now we have to verify the capability of the MNP-HFn system to be recognized and internalized by the tumour cells.

First, exploiting the free amino groups of lysine onto the HFn surface, MNP-HFn were labelled with a fluorescent dye, Rhodamine. We used 5,6-carboxymethyldamine N-hydroxysuccinimide ester (NHS-Rhodamine), exploiting the same reaction described in scheme 4.1A. The binding of rhodamine to the protein occurs by elimination of NHS by nucleophilic substitution of HFt free amine residues. In Figure 5.4 are reported the fluorimetric spectra of HFn-Rhd $5\mu M$ (violet line), MNPs (black line) and MNP-HFn-Rhd (red line), In the spectrum of MNP-HFn-Rhd it is clearly visible a low signal corresponding to rhodamine although significantly lower than that of the HFn-Rhd solution used as reference, whose concentration is the same as that expected if all the HFn reacted with Rhodamine. Such a reduction is due to a damping effect of the magnetite core as demonstrated in figure 5.5 where it is shown how the intensity of the Rhodamine signal of the solution HFn-Rhd $5\ \mu M$, used as reference, is 8 fold reduced in intensity after the addition of MNPs into the solution (blue line). Although this damping effect of the MNPs we estimate the presence of $\approx 3\ \mu M$ of rhodamine in MNP-HFn-Rhd at the concentration of $1 mg/mL$ of MNPs.

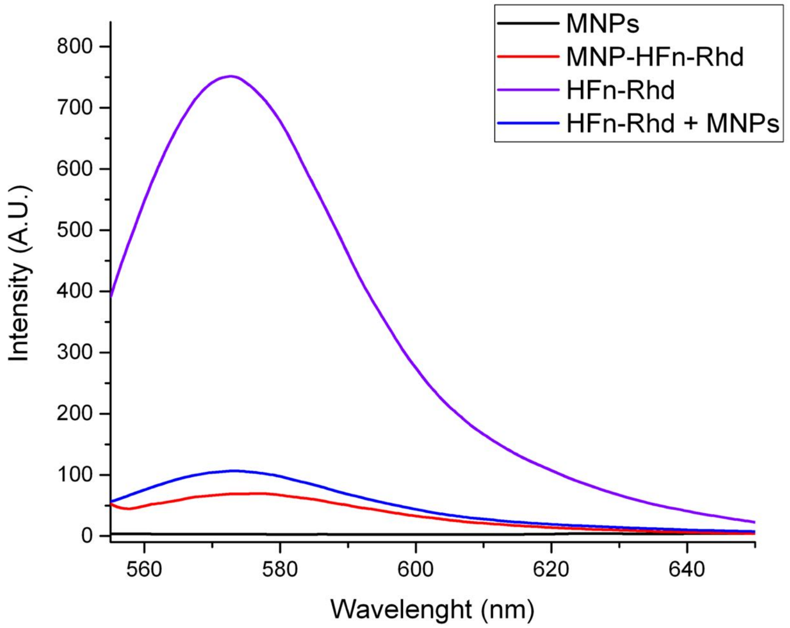

Figure 5.4: Fluorescence emission spectra of MNPs (black line), MNP-HFn-Rhd (red line), HFn-Rhd (violet line), and MNPs mixed with HFn-Rhd (Blue line).

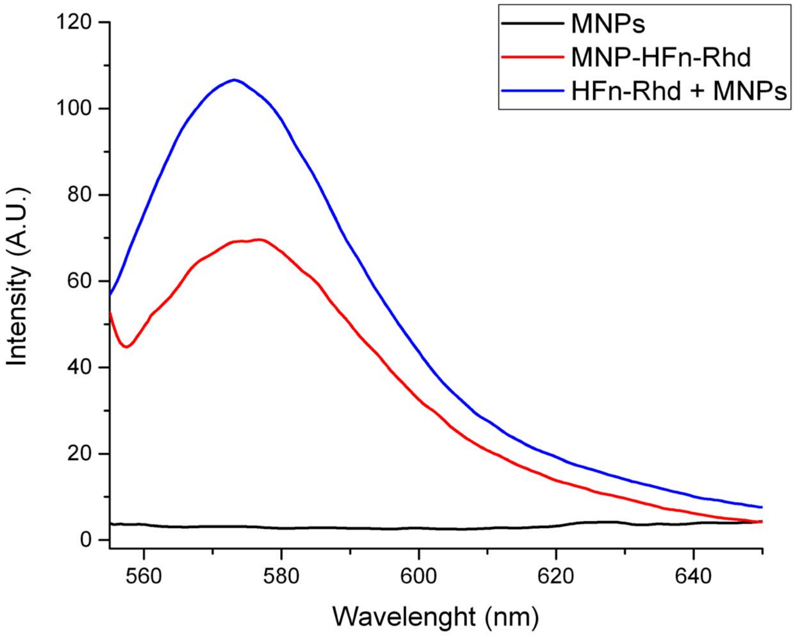

Figure 5.5: Fluorescence emission spectra of MNPs (black line), MNP-HFn-Rhd (red line), and MNPs mixed with HFn-Rhd (Blue line).

Thus, in order to verify the effective internalization of our product, cultures cells of PC3 and MDA-MB2-231were incubated for 1h with the culture medium, BSA 5% in the presence of MNP-HFn-Rhd at two concentrations $0{,}1$ and $0{,}3\ mg/mL$ (mg of MNP in solution). At the end of the incubation, the samples were washed with culture medium and observed through laser scanning confocal microscopy to detect the rhodamine fluorescence. From the collected images it was possible to verify for both concentrations the presence of MNP-HFn within the cellular environment, harvested in vesicles, as previously observed for the HFn alone. Using the confocal microscope, it was also possible to collect images at different focal planes, which allows us to dissect the cell at various heights and to highlight the actual fluorescence inside and outside the cell.

The sequence of images collected in Figure 5.6 shows a breast cancer cell from the level of the plate, towards the upper external surface of the cellular membrane. In all the intermediate images, it can be appreciated, the presence of many fluorescent vesicles scattered within the cell’s volume. Indeed, from these images it can be clearly distinguished the material deposited outside the cell, visible in the first images of the sequence (top left image in Figure 5.6), from the MNP-HFn that have crossed the cell’s membrane and accumulated inside.

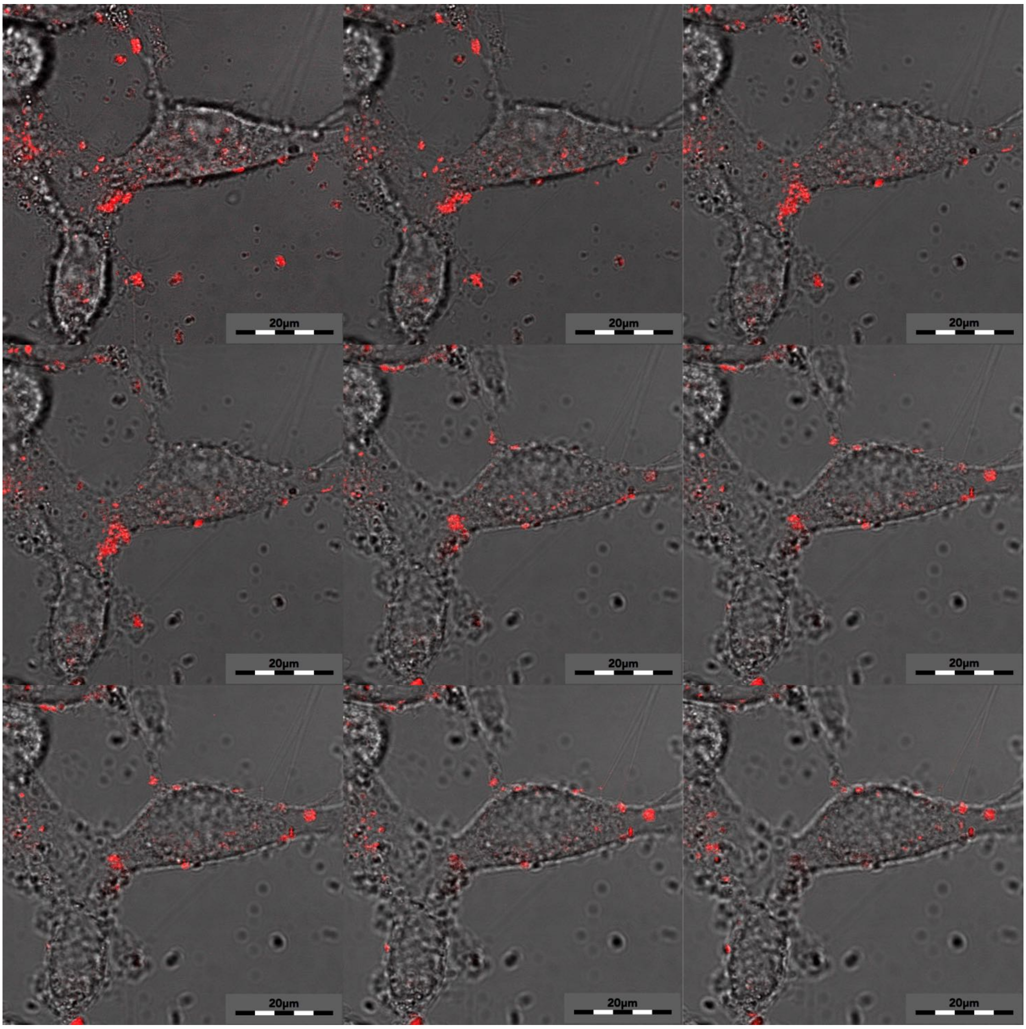

Figure 5.6: Confocal microscope images of a MDA-MB-231 cell incubated for 1h with 0,1 mg/mL of MNP-HFn-Rhd. From top left to bottom right images are equally spaced (0,8µm) at different focus moving upwards from the plane of the petri to the upper surface of cell membrane.

Same conclusions can be obtained by analysing the sequence of images reported in Figure 5.7 obtained on cancer prostate cells. Again, varying the focal plane, fluorescent vesicles were visible throughout the cell's internal volume, confirming the internalization of MNP-HFn.

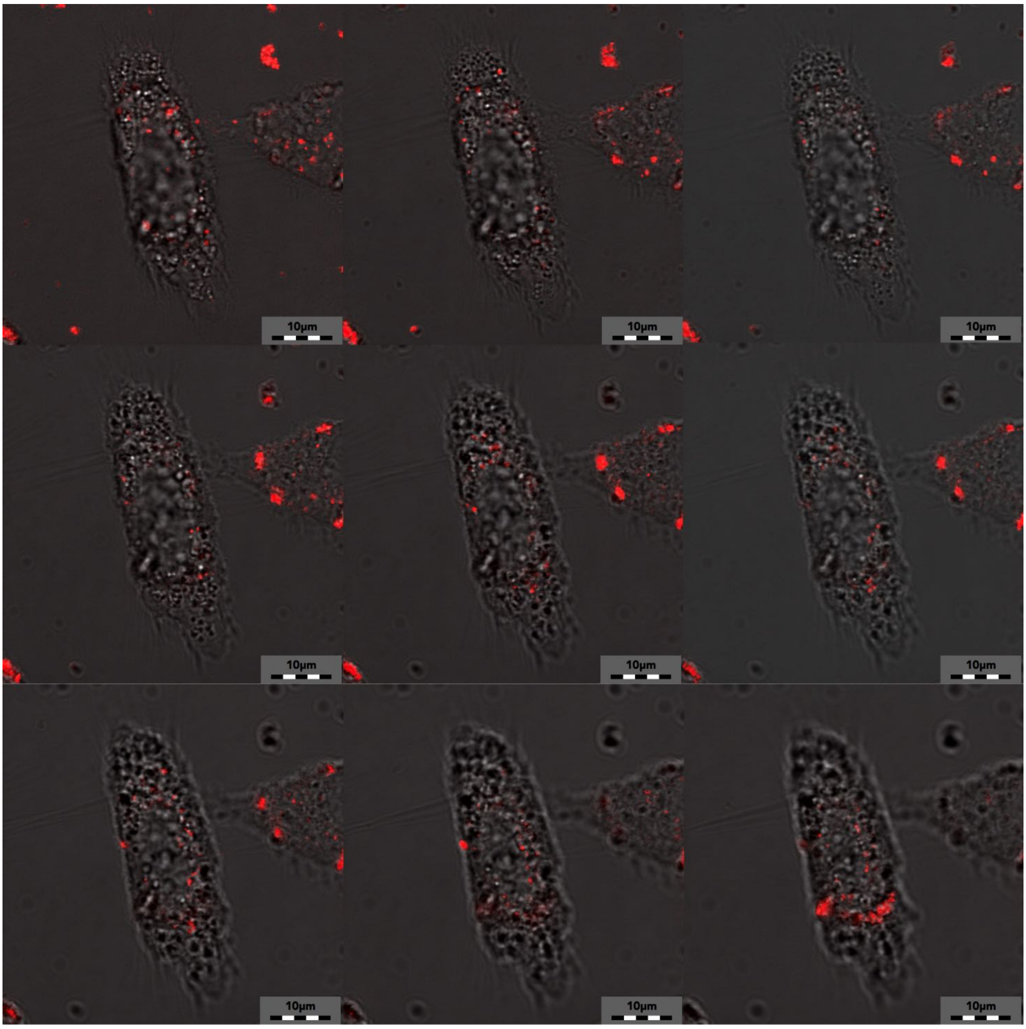

Figure 5.7: Confocal microscope images of a PC-3 cell incubated for 1h with 0,1 mg/mL of MNP-HFn-Rhd. From top left to bottom right images are equally spaced (0,8µm) at different focus moving upward from the plane of the petri to the upper surface of cell membrane.

We can therefore confirm that MNP-HFn is recognized by the TfR1 transferrin receptor and is effectively internalized within the MDA-MD-231 breast cancer and PC3 prostate cancer cells.

5.1.3 Samples preparation

The procedure followed for *in vitro* MFH experiments here described was planned to simulate as close as possible the operating conditions of MFH treatment used in clinical trials. We worked on sterile suspension of cells, which where incubated with MNP-HFn and then exposed to an AMF of frequency and amplitude similar to those used by Prof. Andreas Jordan's team for the treatment of glioblastoma multiforme on human patients: $100\ kHz$ of frequency and field of intensity from $4\ kAm^{-1}$up to $18kAm^{-1}$ [5–8].

All cell lines were cultured in adhesion in the presence of the culture cell medium (DMEM), and then, in order to perform *in vitro* test, were detached from the surface of the cultivation flask by a treatment known as "trypsinization", where the cells are treated with a trypsin solution with EDTA and subsequently neutralized with DMEM culture medium. Trypsin is a proteolytic enzyme that destroys cell adhesion proteins while the function of EDTA is to prevent calcium and magnesium ions from sticking to the bottom of the culture vessel. Prolonged exposure of the cells to these substances could cause their death, so as soon as they are detached from the flask, it is necessary to inhibit the action of the proteolytic enzyme by adding a suitable volume of DMEM containing an inhibitor serum (α-1 antitrypsina).

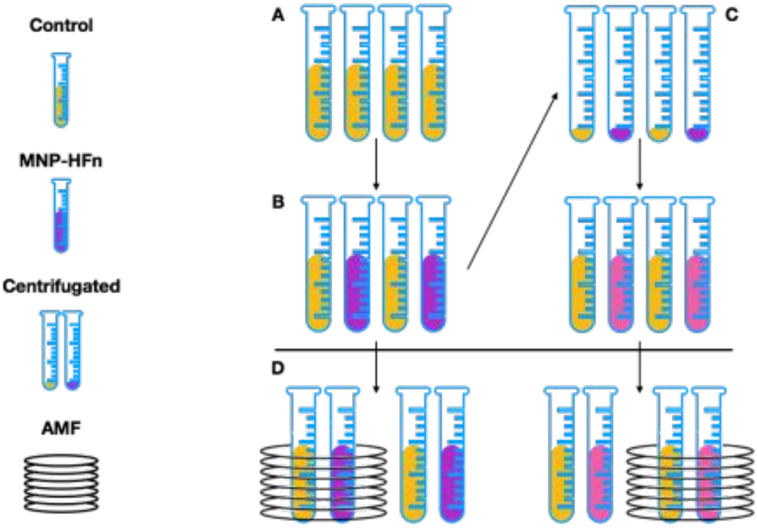

Scheme 5.1: Sketch of the procedure used to prepare the cell samples for MFH experiment. A) 400 k cells were suspended in 0,5 mL of1:1 mix of DMEM a physiological solution; B) two samples were incubated with the MNP-HFn for 1h, and D) one treated sample and one reference were exposed for 1h to the AMF while the other two were kept as reference. C) after incubation (step B)) 4 samples (two incubated and two control) were centrifuged and re-suspended in 0,5mL of mix and finally D) exposed to the AMF in the same manner.

The samples for the MFH experiments were then prepared according to the following steps, also resumed in scheme 5.1. A total of $400.000\,cells$ were suspended in $500\,mL$ of a 1:1 mix of DMEM and physiological solution containing $5\,\%$ BSA to obtain a homogeneous suspension, and incubated for 1h in the presence of MNP-HFn at the desired concentration of magnetic material. A control sample was also prepared following the same procedure but without incubating the cells with the solution of MNP-HFn.

In order to discriminate between the effect of extracellular global heating (i.e. the heating of the suspension produced by the totality of MNPs either internalized or not) and that of the internalized MNPs alone each sample was investigated both as described above and after centrifugation for $5\,min$ at $5000\,rpm$, (in the following labelled as ctrf) so as to remove all non-internalized MNP-HFn, and re-suspension in $500\,mL$ of 1:1 DMEM/physiology solution mix at $5\,\%$in BSA. It is known from the literature, indeed, that the local heating produced by internalized MNPs can trigger the apoptotic process even in the absence of any sizable temperature increase[2]. For each sample a control was also prepared which was not exposed to the AMF. The samples exposed to the AMF, were introduced in the middle of the induction coils inside a glass container, thermostated at $37\ °C$ by a flow of ethylene glycol to exclude thermal gradients due to coils heating and to the external environment. The field of $17\ kAm^{-1}$ intensity and frequency of $183\ kHz$ was left to operate on the system for 1h. At the end of the hyperthermic treatment the samples were centrifuged, cells were counted to the trypan blue test to check the direct effect of the treatment and then plated. After $48\ h$ we performed on the colony the MTT vitality test. This is the indicative test for effective cellular vitality as it gives a value that is directly proportional to cellular mitochondrial activity[9].

The adopted procedure allows a check of the effective efficacy of the hyperthermic treatment by comparison, for each tested concentration, of the control, of cells incubated with MNP-HFn, and of the action of the AMF.

5.1.4 *In vitro* MFH treatment

In this section, the outcomes of MFH *in vitro* tests will be discussed. Before the *in vitro* test on tumour cells, we measured the hyperthermic efficiency in a biocompatible buffer equal to that we will use in the *in vitro* test. Our purpose is to determine the concentration of the MNPs necessary to reach $42°C$ and then keep it for at least $30\ min$. We chose this threshold as temperature around $\approx 42°C$ were commonly reached in typical hyperthermia treatments[10]. In figure 5.8 and 5.9 are shown the kinetic curves for MNP-3-HFn and MNP-4-HFn, respectively, suspended in saline solution containing 1X PBS and $5\ \%$ of bovine serum albumin (BSA).

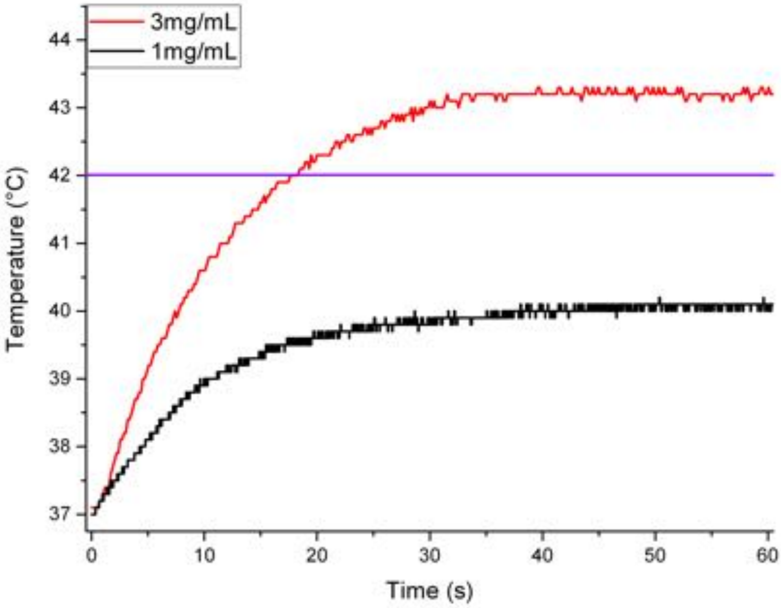

Figure 5.8: Kinetic evolution of temperature of MNP-3-HFn suspended in 0,5 mL mix 1:1of DMEM and physiological solution at different concentrations (1 and 3 mg/mL). The violet line indicates the 42°C threshold.

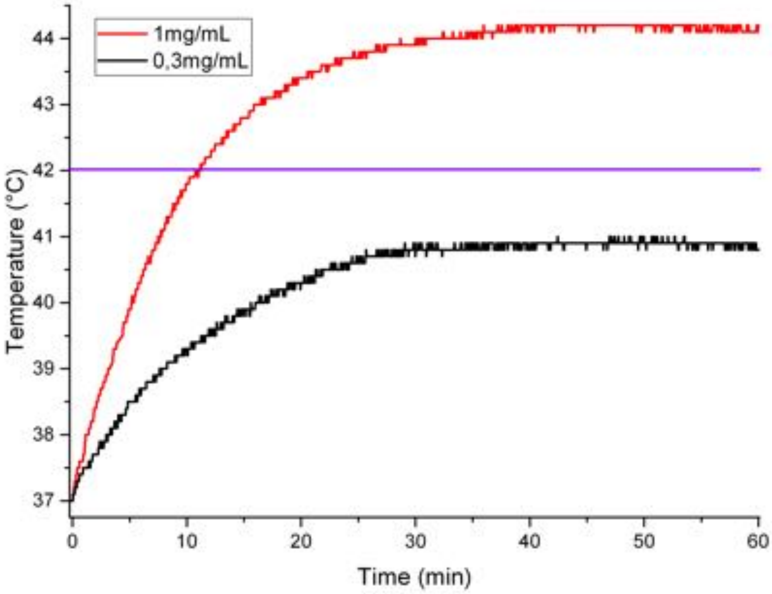

Figure 5.9: : Kinetic evolution of temperature of MNP-4-HFn suspended in 0,5 mL mix 1:1 of DMEM and physiological solution at different concentrations (0.1 and 0.33 mg/mL). The violet line indicates the 42°C threshold.

The conditions that meet the above requirements were $3\, mg/mL$ of magnetite for MNP-3-HFn and $1mg/mL$ of magnetite for MNP-4-HFn. Moreover, we found the concentration $1mg/mL$ and $0{,}3\, mg/mL$ for MNP-3-HFn and MNP-4-HFn, respectively, are appropriate to investigate the MFH treatment effectiveness at temperature slightly below the $42°C$ threshold. In fact, we also want to study the effectiveness of the MFH treatment when the temperature reached are lower than that threshold and verify if there is a non-thermal antitumoural effect due to the MNP internalized within the cells.

During the *in vitro* MFH treatment of tumour cell, it is not possible to directly control the T evolution, as the introduction of the temperature probe would cause bacterial contamination. The temperature was then measured with an external thermometer probe and then the real temperature was estimated through a calibration.

5.1.4.1 MFH on PC3

PC3 cell samples were treated with MNP-3-HFn ($1\ \mathrm{h}$) at the two concentrations identified in the experiments previously described, i.e. 1 and $3\ \mathrm{mg/mL}$. For each concentration, two samples were investigated, one centrifuged before being exposed to AMF and one not centrifuged. At the end of the application of the AMF ($1\ \mathrm{h}$), living cells were counted at the optical microscope after the stain with trypan blue.

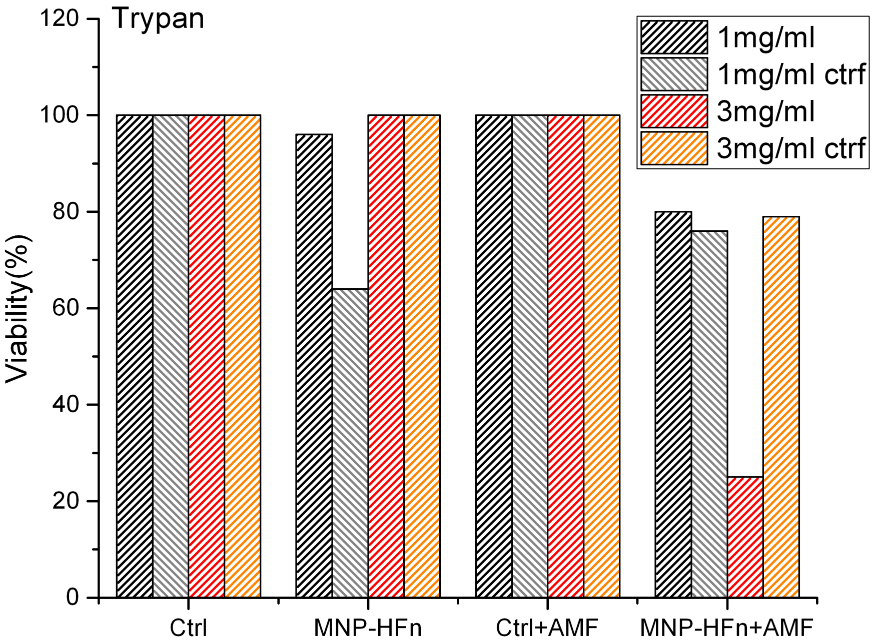

Figure 5.10: Number of PC3 living cells counted at Trypan blue assay. Each value is normalized to the corresponding control sample.

Figure 5.10 shows histograms of the percentage of living cells counted in the samples referred to the controls, taken as $100\ \%$. The data show an unusual behaviour: samples treated with MNP-HFn and exposed to AMF generally suffer a 20% reduction only, with the exception of the non-centrifuged sample at $3\ mg/mL$ of MNP-HFn which shows a significant reduction of $70\ \%$ of the number living cells. Samples incubated at $3\ mg/mL$but not exposed to the AMF did not suffer any change in cell viability. These results suggest that the significant reduction of living cells in the sample exposed to the AMF has been induced by a direct thermal damage due to a global temperature increase during the treatment. MTT data, obtained at $48\ h$ from AMF treatment, confirmed this result.

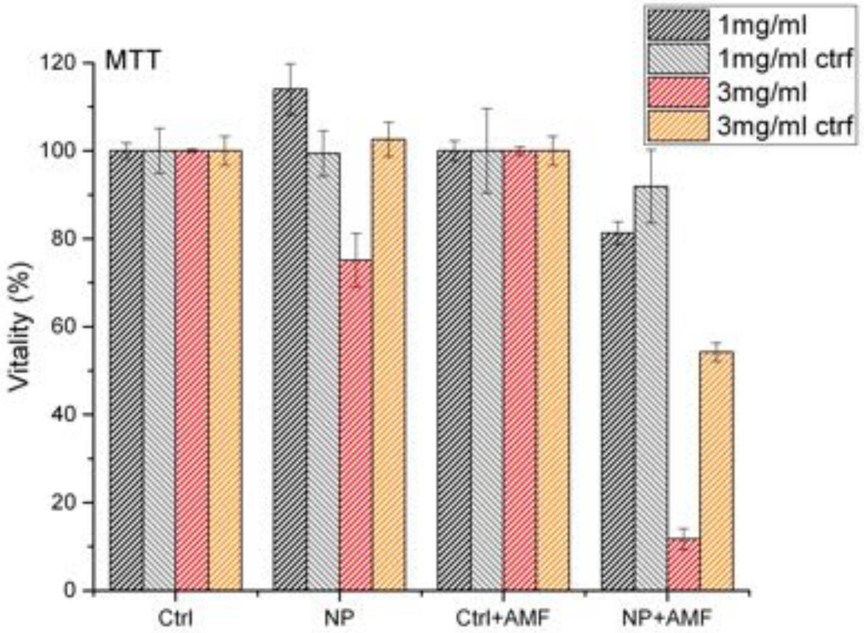

Figure 5.11: MTT cellular vitality assay on PC3 cell at 48h from the hyperthermic treatment. Each values are normalized to the corresponding control sample.

In the MTT vitality histogram, shown in Figure 5.11, a large reduction of the vitality of cells is observed for the $3\ mg/mL$ samples, equal to $50\ \%$ and $90\ \%$ for centrifuged and non-centrifuged one, respectively. The other samples show only slight variations in vitality, which are not adequate for an efficient anticancer treatment.

The kinetic evolution of external temperature recorded during the MFH treatment, are shown in figure 5.12. These curves reveal that, as expected, non-centrifuged samples reach an internal estimated temperature higher ($\approx 43\ °C$ for $3\ \frac{mg}{mL}$) and lower ($\approx 40\ °C$ for $1\ mg/mL$) than the $42\ °C$ threshold. Conversely, the estimated internal T of centrifuged $1\ mg/mL$ sample increases only up to $\approx 39°C$; while the centrifuged $3\ mg/mL$ sample reaches a greater temperature, slightly below $42°C$. The samples heated up to $T < 40\ °C$, were not affected by any thermal damages. Therefore, complete cell death was obtained only in the sample with the highest rise in temperature, corroborating the hypothesis that

MFH therapy is effective for those samples that reached or exceeded $42\,°C$ during the treatment thanks to the heating of the environment. No effects arising from local intracellular heating seems to be effective on our samples.

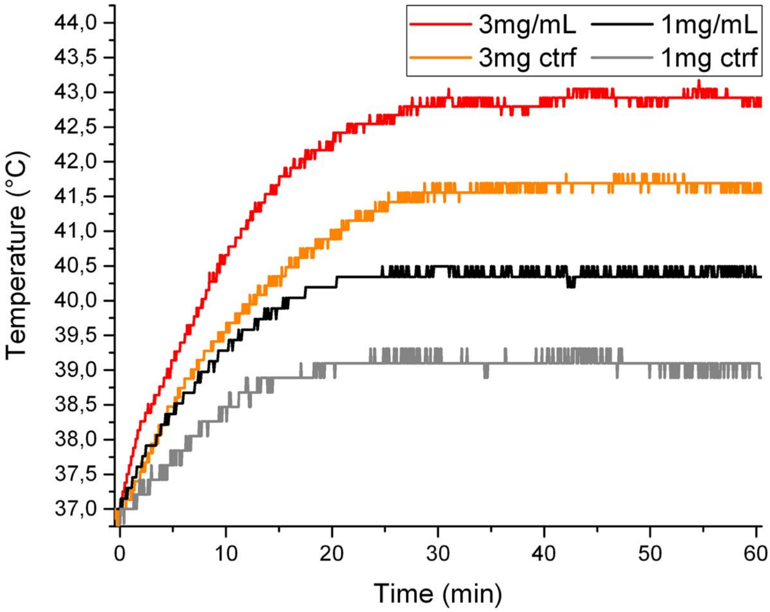

Figure 5.12: Temperature evolution during the MFH treatment, on PC3 cells incubated with MNP-3-HFn.

5.1.4.2 MFH on MDA-MD-231

MDA-MD-231 cell samples were treated with MNP-3-HFn and with MNP-4-HFn, respectively, using the concentrations identified as the best ones in the experiments described in section 3.1.3.4, i.e. $1-3\ \mathrm{mg/mL}$ for MNP-3-HFn, and $0{,}3-1\ \mathrm{mg/mL}$ for MNP-4-HFn. Also in this case the cell suspensions were exposed to the AMF both before and after centrifugation. In figure 5.13 are shown the histograms of the living cells counted with the trypan blue assay at the optical microscope after the treatment with AMF.

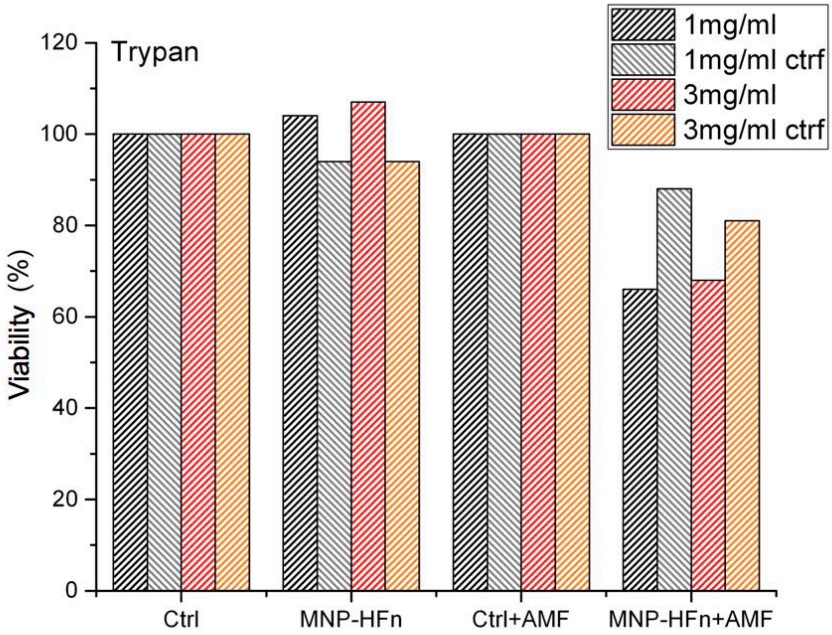

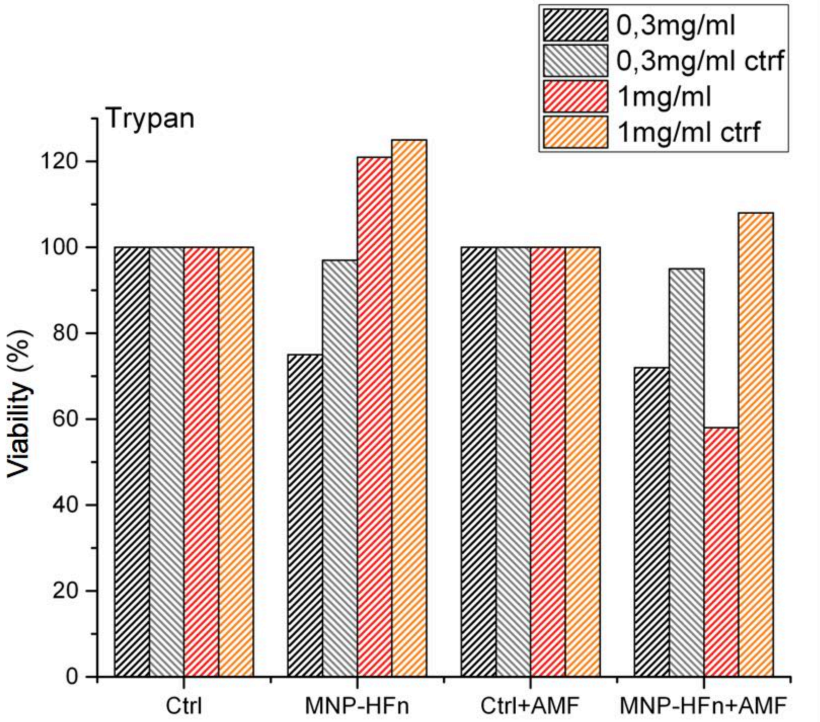

Figure 5.13: Number of living MDA-MB-231 cells counted at Trypan blue assay after the hyperthermic treatment. Each value is normalized to the corresponding control sample. MNP-3-HFn in the upper panel; MNP-4-HFn in the lower panel.

Unlike PC3, after the MFH treatment the number of living MDA-MB-231 cells for the non centrifuged samples ishigher, being $66\ \%$ and $68\ \%$ for MNP-3HFn at $1\ mg/mL$ and at $3\ mg/mL$, respectively, and $72\ \%$ and $52\ \%$ for MNP3-HFn at $0{,}3\ mg/mL$and $1\ mg/mL$, respectively. Similarly, also for the centrifuged samples the number of living cells is much larger than in the PC3 case, the effect of the AMF on the cell viability being almost negligible. Indeed, after the MFH treatment the cell viability was for MNP-3-HFn $88\ \%$ at $1\ mg/mL$ and $81\ \%$ at $3\ mg/mL$; and for MNP-4-HFn $95\ \%$ at $0{,}3\ mg/mL$ and $108\ \%$ at $1\ mg/mL$. This result suggests that all the non-centrifuged samples, have suffered direct thermal damage during the treatment, even if to a lower extent with respect to the previous experiment. No significant change in the number of living cells were seen for the treated cells not exposed to the AMF, as previously seenfor the PC3 samples.

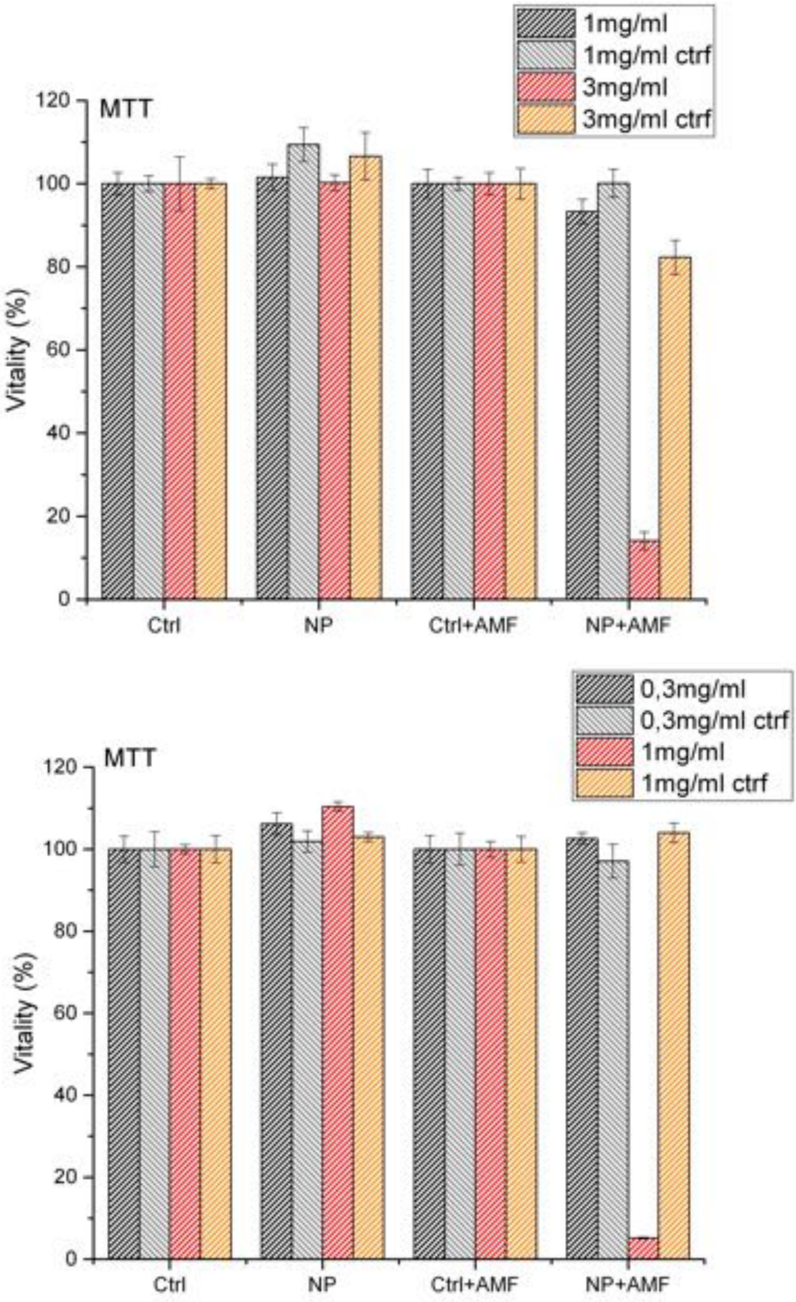

Figure 5.14: MTT cellular vitality of MDA-MB-231 cells at 48h from the hyperthermic treatment. Each value is normalized to the corresponding control sample. MNP-3-HFn is reported in the upper panel, MNP-4-HFn in the lower panel.

The MTT vitality histogram, shown in Figure 5.14, confirms the previous data. Indeed, the only significant variations in cell vitality are observed for the samples treated at the highest concentration of 3 mg / mL for MNP-3-HFn and 1mg/mL for MNP-4-HFn: all cells of these samples, indeed, seem to have been damaged by the external temperature which dramatically compromised their vital functions, rather than by an intracellular heating mechanism. All other samples did not show any significative decrease of cell vitality.

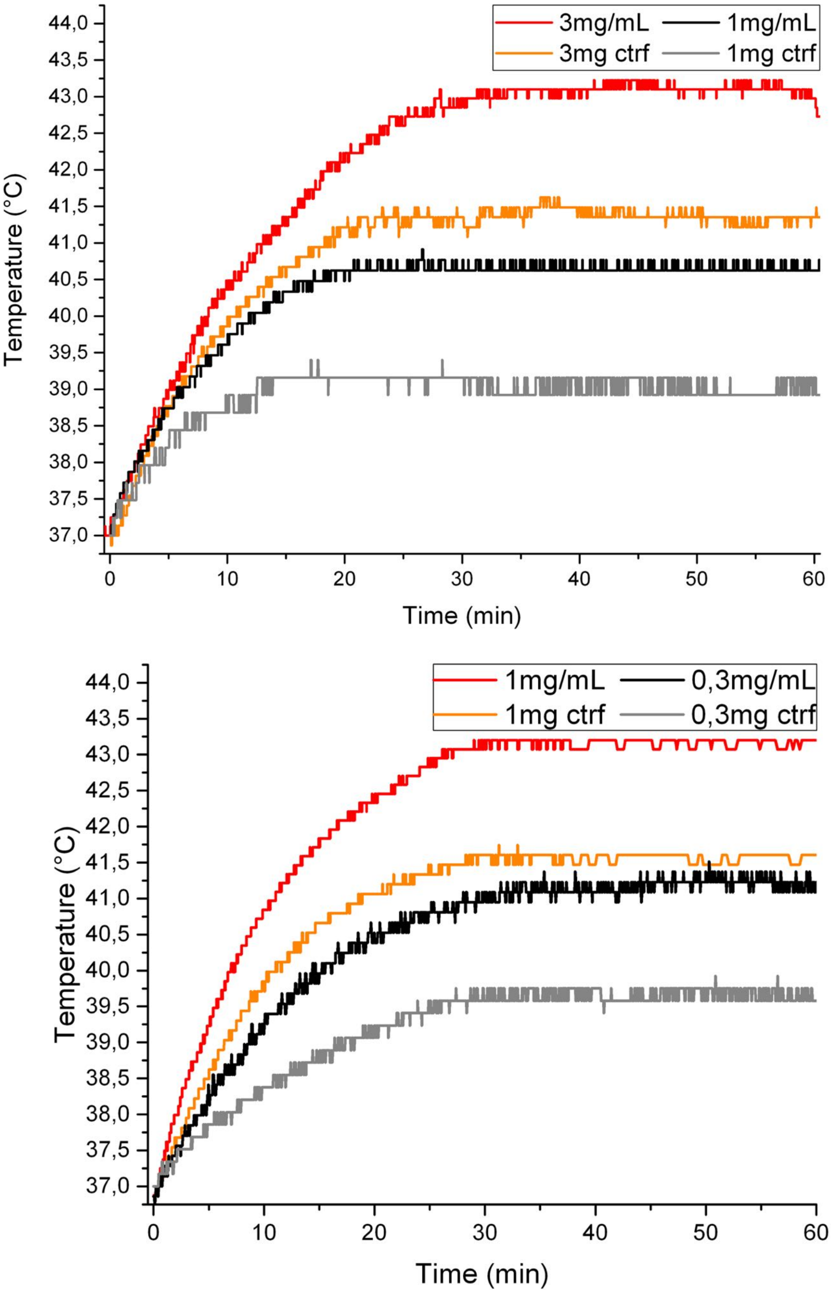

Figure 5.15: *Temperature evolution during the MFH treatment on MDA-MB-231 cells incubated with MNP-3-HFn (upper panel) and MNP-4-HFn (lower panel).*

As expected the evolution of temperature recorded during the MFH treatment, reported in figure 5.15, reveals that only samples at the higher concentration reaches $T \approx 43{,}3\ °C$, while all the others reach a temperature lower than $42\ °C$ during the treatment. The samples that do not overcome $42\ °C$ do not show any reduction in cell viability. Indeed, only samples that overcome $42\ °C$ show a total reduction of cell viability, as if the mechanism responsible of the cell death were only the thermal damages due to the temperature reached.

To verify these results we tested the effect of standard heating on cells, that is, some PC3 cells were prepared according to the same procedure used for the MFH *in vitro* test and immersed in a thermal bath for growing times at $44\ °C$ and $48\ °C$. Figure 5.16 shows the results of the trypan blue cell count after the thermal treatment. For both temperatures, a dose-dependent effect is visible: the samples heated at 44°C show a progressive reduction in the number of living cells of $15\ \%$ for $t = 10\ min$, $25\ \%$ for $t = 20\ min$, up to $50\ \%$ for $t = 30\ min$. The samples heated at $48\ °C$, instead display a reduction in viability of $50\ \%$ for $t = 10\ min$, $70\ \%$ for $t = 20\ min$, and $80\ \%$ for $t = 30\ min$.

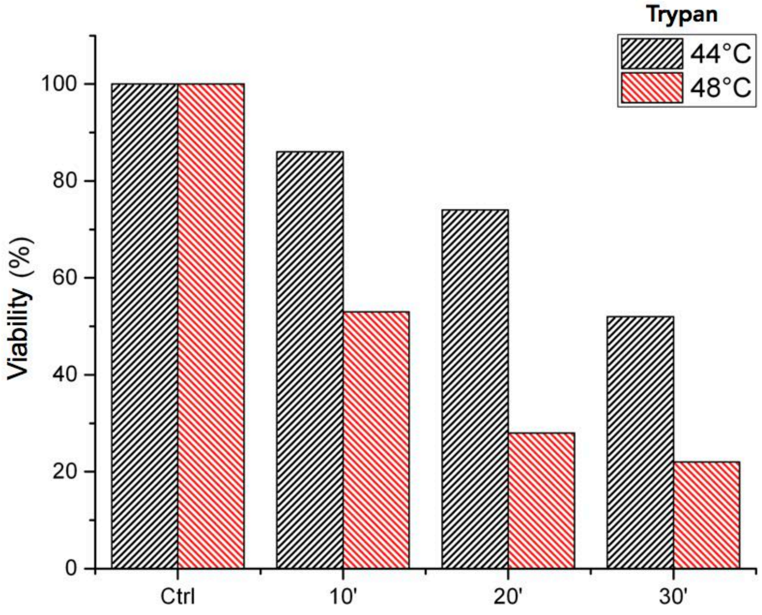

Figure 5.16: Number of PC3 living cells counted at Trypan blue assay after the thermal treatment. Each value is normalized to the corresponding control sample.

After $48\ \mathrm{h}$ (MTT analysis, figure 5.17) a more dramatic dependence on the time of immersion in the thermal bath is observed at $48\ °C$, since all the samples have suffered thermal damages. Conversely, for the samples heated at $44\ °C$ a gradual reduction in vitality is observed. We can thus conclude that heating for $30\ min$ at $44\ °C$ is not a thermal dose large enough to lead all cells to death. These data are in contradiction with our experimental results, as the hyperthermic treatment seems to induce critical damages for lower maximal temperature and time intervals.

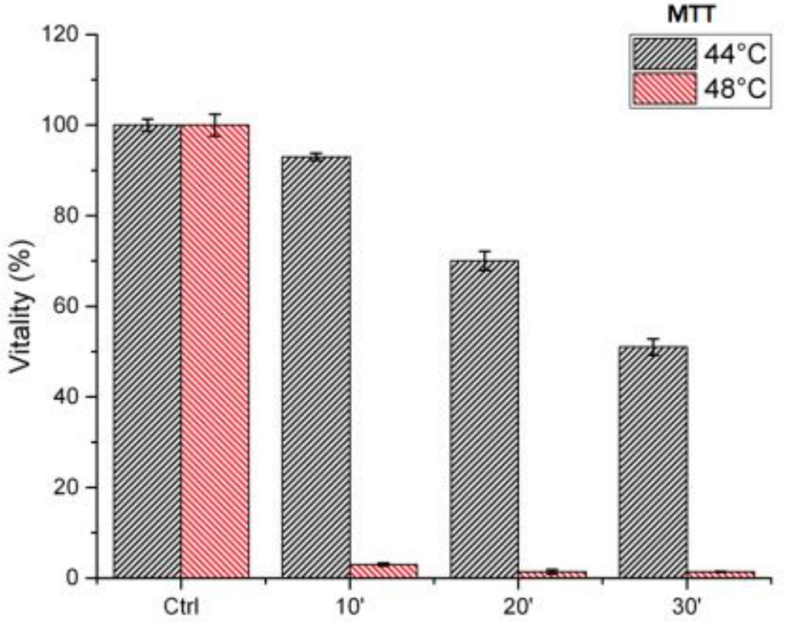

Figure 5.17: MTT vitality essay on PC-3 cells, at 48 h from the thermal treatment. Each value is normalized to the corresponding control sample.

In order to rationalize this result it can be helpful a comparison with literature data on resistance to hyperthermic treatments of *in vitro* cellular samples. Human cells generally have higher resistance to thermal treatments than other animal cells and therefore need higher thermal doses (TD), commonly defined as equivalent cumulative minutes of treatment at $43\ °C$[10]. However, the duration and temperature required to realize an efficient hyperthermic treatment are still under debate[11]. In general, a "breakpoint" at $43\ °C$ is observed in *in vitro* human cells[12]. Indeed, to obtain the same therapeutic effect of a hyperthermic treatment at $T = 43\ °C$ and time $t = t_{43}$ for a higher temperature, $T = 43 + n$ it is required $t = {t_{43}}/{2n}$; conversely, for lower temperature, $T = 43 - m$ it is needed $t = t_{43} \times 4m$[11]. Then, we can introduce the thermal isoeffective dose (TID) as the time in minutes at $43\ °C$ (EM43) which corresponds to the thermal dose administrated keeping a system at T_a for the time t_a. TID can be evaluated with the formula:

$$TID = EM43 = t_a \cdot R^{(43-T_a)}$$

where R is a conversion factor to compensate $1°C$ temperature change above or below the breakpoint. Human cells usually have $R \approx 0{,}25$ below the breakpoint and $R \approx 0{,}5$ over the breakpoint[11]. The dependence of the thermal dose on temperature and time of application of the AMF for the desired therapeutic effect is shown in Figure 5.18[12].

Our results are consistent with this model. However, if on the one hand the ineffectiveness of treatments that did not reach $43\ °C$ it is not unexpected, on the other the large mortality observed in MFH treatments performed at $43\ °C$ suggests that internalized MNPs can provide an additional contribution which enhances the efficacy of the treatment.

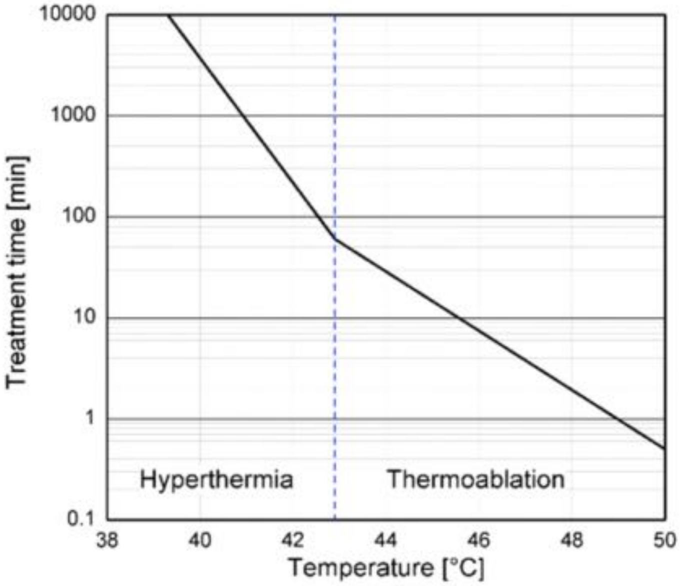

Figure 5.18: Isoeffect curve of the treatment time vs. treatment temperature for hyperthermia(taken from Dutz et Hergt[12]).

The MNP-HFn internalized into the cells may indeed play an adjuvant role providing a direct inner damage which, combined with the external increment of temperature, can lead to a stronger efficacy of the MFH treatment. This is an important indication that deserves further in-depth study in the next future. The knowledge of the mechanism of heating is in fact crucial also to establish the best way to deliver the magnetic material between active targeting, that permits to cross the cell membrane, or accumulation of MNPs in the extracellular matrix by the EPR effect only.

5.2 *In vivo* test of MNP-HFn

All the results obtained so far have shown the system MNP-HFn is a promising candidate to be used as theranostic agent in the therapy of tumours. Therefore, we decided to deepen the characterization of our nano-system by investigating the *in vivo* biodistribution, the toxicity and genotoxicity and the antitumor efficacy of MFH treatment with MNP-HFn. Most of these experiments are still in progress. Here, however, the preliminary results obtained by experiments carried out on female Swiss albino mice, bearing Ehrlich ascitic breast tumour, are described. These experiments were performed by Prof. Zulmira Lacava and Mr.s Danyelle A. Ferreira at the laboratory of Instituto de Ciências Biológicas of the University of Brasilia (Brazil).

5.2.1 Toxicity evaluation

Initially, the female Swiss albino mice were randomly distributed in treatment and control groups (5 groups; 6 mice/group), following the guidelines for the design and statistical analysis of experiments using laboratory animals for a pilot study[14]. Mice groups were intraperitoneal injected, with dose tuned according to their weight, during 8 consecutive days with three different concentrations of MNP-HFn suspensions, and compared to negative control (injected with PBS) and to a positive control which was injected with

MethylMethaneSulfonate (MMS). MMS is a mutagenic substance commonly used as positive control as described in the Organisation for Economic Co-operation and Development (OECD) guideline[15]. In scheme 5.2 are summarized the different treatments for the various groups selected.

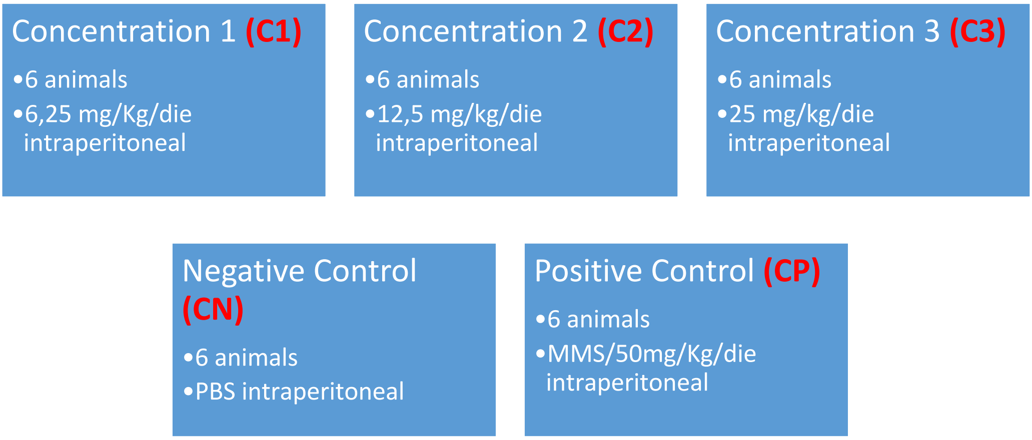

Concentration 1 (C1)
- 6 animals
- 6,25 mg/Kg/die intraperitoneal

Concentration 2 (C2)
- 6 animals
- 12,5 mg/kg/die intraperitoneal

Concentration 3 (C3)
- 6 animals
- 25 mg/kg/die intraperitoneal

Negative Control (CN)
- 6 animals
- PBS intraperitoneal

Positive Control (CP)
- 6 animals
- MMS/50mg/Kg/die intraperitoneal

Scheme 5.2: Diagram of the treatment received by each group of mice.

5.2.2 *In vivo* investigation of the potential toxicity of MNP-HFn

	CN	***CP***	***C1***	***C2***	***C3***
WBC 10^3/uL	3,1 ± 0,4	2,65 ± 1,0	4,86 ± 0,7	5,0 ± 0,6	3,8 ± 0,2
RBC 10^6/uL	8,3 ± 0,3	8,5 ± 0,2	7,98 ± 0,3	8,5 ± 0,4	8,2 ± 0,3
HGB g/dL	12,3 ± 0,3	12,1±0,4	11,65 ± 0,6	11,6 ± 0,6	11,6 ± 0,5
HCT %	31,2 ± 1,0	31,85 ± 0,9	30,2 ± 1,2	31,1 ± 1,8	30,5 ± 1,3
MCV fL	37,5 ± 0,5	37,6 ± 0,7	37,8 ± 0,3	36,6 ± 0,5	37,2 ± 0,4
MCH pg	14,8 ± 0,3*	14,3 ± 0,3	14,6 ± 0,2	13,7 ± 0,2*	14,1 ± 0,2
MCHC g/dL	39,6 ± 0,6*	38,0 ± 0,1	38,5 ± 0,5	37,3 ± 0,3*	37,9 ± 0,2
PLT 10^3/uL	1013,2 ± 145,5	893,33 ± 81,3	990,7 ± 140,3	1326,2 ± 175,0	1048,5 ± 63,9

Table 5.3:Haematological analysis performed 24h after the last treatment: WBC, white blood cells; RBC, red blood cells; HGB, haemoglobin; HCT, haematocrit; MCV, mean cell volume; MCH, mean cell haemoglobin; MCHC, mean cell haemoglobin concentration; PLT, platelet.

In vitro tests suggested that MNP-HFn is non-toxic. In order to confirm this result *in vivo*, the groups of animals underwent to different tests: haematological and biochemistry analysis, feed intake and weight of organs. Organs and blood for these exams were collected 24h after the last treatment. At first we performed the haematological analysis. The haemograms, reported in table 5.1 revealed no significant changes in the main haematological parameters of all the investigated animals. The biochemistry analysis, reported in table 5.2, also provided precious information on MNP-HFn biocompatibility. In fact, an increase in the value of glutamate-pyruvate transaminase (GPT), glutamate-oxalacetate transaminase (GOT) and alkaline phosphatise are indicative of liver damages, creatine a urea of kidney damages, while lactate dehydrogenase (LDH) is a signal of general tissue damages. In general all the parameters of the animals treated with MNP-HFn did not show any significant deviation. Indeed, only for the positive control a high value in glutamate-oxalacetate transaminase (GOT) was observed, indicating liver damages. This result is not surprising since liver is one of the target tissues of MMS (proof of these damages will be however obtained by histological analyses, under way). The absence of any statistical difference in all the other values have to be combined with the histological analysis, currently in progress, to assure that the MNP-HFn did not cause any damage to any organs.

	CN	CP	C1	C2	C3
GPT (ALT) -U/L	17±3,8	32,2±4,9	30,2±3,4	21,67±3,116	27,83±1,014
GOT (AST) -U/L	57±6,*	114,7±7,8*	94,3±14,9	70,83±9,6	105,3±22,65
CREATININE (mg/dL)	0,32±0,02	0,31±0,01	0,36±0,03	0,27±0,02	0,30±0,01
ALKALINE PHOSPHATASE (U/L)	11,33±1,89	9,16±0,91	9,00±0,81	10,67±1,60	5,83±2,18
IRON (µg/dL)	166,8±16,8	171,2±37,2	138,2±37,2	188,0±44,3	275,8±21,5
LDH mg/dL	703±242,1	1031±178,3	678,5±101,5	778,0±99,78	558,5±30,05
UREA (mg/dL)22	49,5±3,4*	50,7±6,6	45,3±4,08	34,0±1,1*	37,0±2,2

Table 5.4 Biochemical analysis 24 h after the last treatment: glutamate-pyruvate transaminase GPT(ALT); glutamate-oxalacetate transaminase GOT(AST); Creatinine; Alkaline phosphatase; Iron; Lactate dehydrogenase, LDH; Urea.

The body weight and feed intake of the 5 groups of mice were monitored during the experiment, and the results are shown in Figure 5.14. No statistical differences were found neither in the weight nor in the feed intake among the groups during the 9 days of treatment with the only exception of the positive control group, which exhibits higher values of feed intake. This result, therefore supports once more the biocompatibility of our sample.

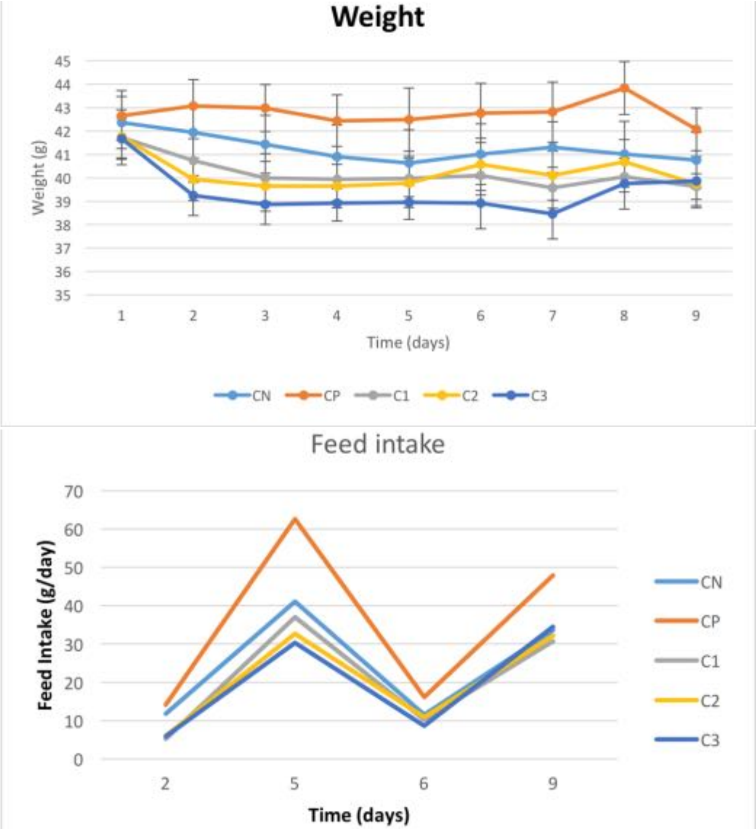

Figure 5.19: (upper panel) Mean weight chart of the mice groups during the experiment. (lower panel) Feed intake chart of the mice groups on day 3-5-6-9 of the experiment.

The weight of the liver and spleen after explanation at the end of the treatment was also determined and the obtained data are shown in Figure 5.15. In the groups treated with MNP-HFn a clear trend of the weight of the organs with the administered iron oxide dose per kg is observed. This behaviour is coherent with the progressive increase of iron administrated and fully consistent with literature data[16], thus confirming that no anomalies occurred when MNP-HFn was injected in mice.

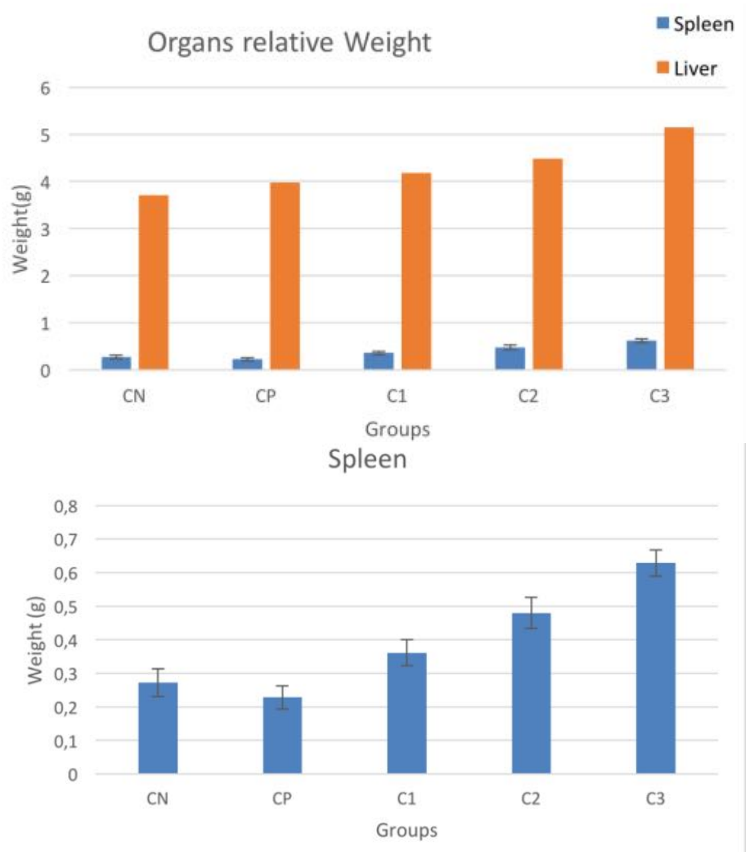

Figure 5.20: Mean weight of the mice group liver (upper panel) and spleen (lower panel) after the biocompatibility test.

In conclusion, all the analyses performed until now show no change in the vital parameter of the mice indicating that the non-toxicity of MNP-HFn is preserved *in vivo*. The results of histopathology and genotoxicity tests (comet assay, micronucleus, and DNA fragmentation) are currently under way, but data are not available yet.

5.2.3 *In vivo* validation of the MFH efficacy

After validation of the biocompatibility of our product we proceeded with the evaluation of its efficacy in in vivo treatment of tumour by MFH on mice. To this aim the female Swiss albino mice initially were randomly distributed among the treatment and control groups (7 groups; 6 mice/group), following the guidelines for the design and statistical analysis of experiments using laboratory animals for a pilot study[14].

The seven Swiss albino mice groups received the following treatment:

- M-Ctr, control group; no treatment;
- M-NP(EV), control group; mice injected intravenously with MNP-HFn,
- M-T-Ctr, control group; tumour bearing mice, no treatment;
- M-T-NP(IT), control group; tumour bearing mice, injected intratumour with MNP-HFn;
- M-T-AFM, tumour bearing mice exposed to AMF;
- M-T-NP(IT)-AFM, tumour bearing mice, injected intratumour with MNP-HFn and exposed to AMF;
- M-T-NP(EV)-AFM, tumour bearing mice, injected intravenously with MNP-HFn and exposed to AMF.

In Figure 5.14 the different treatment received by each group are schematically resumed:

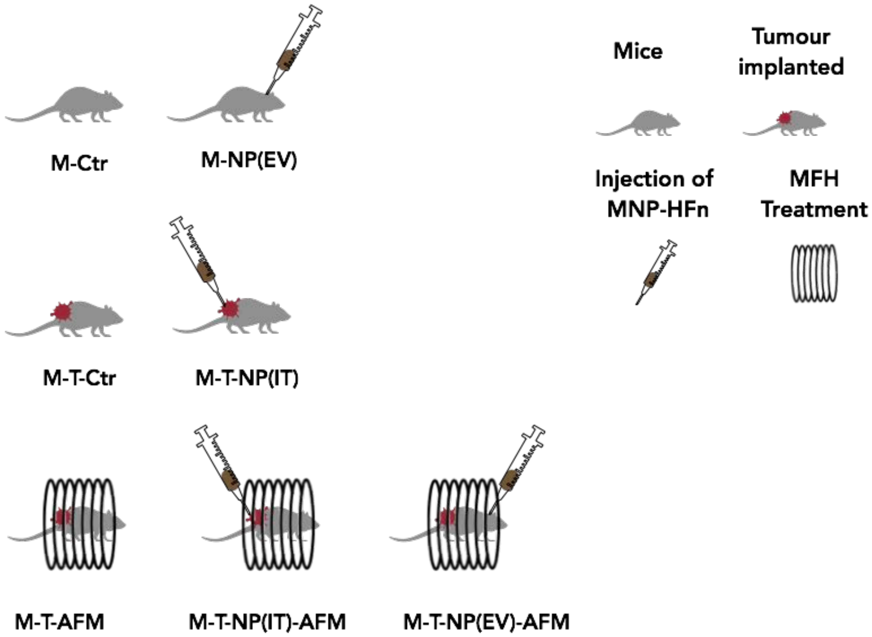

Figure 5.21: Schematic representation of the different treatments applied on seven groups of Swiss albino mice. On the top right side is the legend of the symbols used to differentiate among the various groups. MNP-HFn was injected either intravenously (EV) or directly in the tumour (IT). :

The mice groups received a 10 days treatment during which they were injected and/or exposed to the AMF. The protocol of the treatment for each group and the administered dose as reported in table 5.3.

Group	Day 1	Day 3	Day 5	Day 7	Day9
M-Ctr	Placebo	Placebo	Placebo	Placebo	Placebo
M-NP(EV)	$80\mu l$	$80\mu l$	$80\mu l$	$80\mu l$	$80\mu l$
M-T-Ctr	Placebo	Placebo	Placebo	Placebo	Placebo
M-T-NP(IT)	$100\mu l$	$80\mu l$	$60\mu l$	$80\mu l$	$60\mu l$
M-T-AFM	Placebo AFM	Placebo AFM	Placebo AFM	Placebo AFM	Placebo AFM
M-T-NP(IT)-AFM	$100\mu l$ AFM	$80\mu l$ AFM	$60\mu l$ AFM	$80\mu l$ AFM	$60\mu l$ AFM
M-T-NP(EV)-AFM	$80\mu l$ AFM	$80\mu l$ AFM	$80\mu l$ AFM	$80\mu l$ AFM	$80\mu l$ AFM

Table 5.5: Scheme of the MFH experiment; details of the injection and AMF treatment received.

Mice were injected with physiologic solution as placebo while the treated mice received the MNP-HFn with injection of $100 - 80 - 60\ \mu l$ at $10\ mg/mL$; mice injected intratumourly received different injection following a procedure identified by Lacava's group, while the mice injected intravenously received always the same amount due to difficulties found in administering larger dose intravenously.

The AMF equipment used for the experiments is shown in Figure 5.17 A and B. It is a in-house built radio frequency hyperthermia (RF-HT) portable apparatus developed by *Lacava's* research group, CMagMHG[17,18], The set-up is constituted by one cylindrical metallic rod of 10.7 mm diameter, closely wound by a coil of wire concentrating the alternating magnetic flux. The solenoid core is linked to a moveable support to apply the magnetic field in the targeted region[19].

Mice were exposed for 30 min to an AMF of $3{,}18\ kAm^{-1}$ field amplitude and $1\ MHz$ frequency.

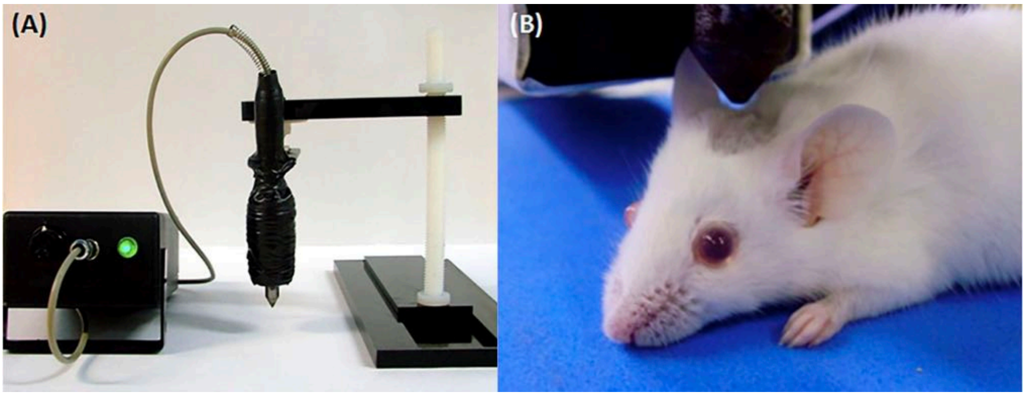

Figure 5.22:Images of the equipment employed to evaluate in vivo the efficiency of MNP-HF to reduce tumour growth by MFH (A) portable apparatus developed by Lacava's research group (CMagMHG); (B) Application of the AMF on the animal.

In order to evaluate separately the short-term and long term efficacy of the therapy, after the last treatment each group was separated in 2 subgroups (3 animal/group), and analysed after 2 and $10\ days$ respectively. Each subgroup is identified by the suffix -2 and -28, to identify the number of days spent before the analysis.

During all the experiment mice were weighted to check their health. Although the complete analysis is still in progress, here we briefly present the preliminary results obtained from comportamental behaviour, mice weight, tumour volume, spleen and liver weight and haematological and biochemistry analysis.

Figure 5.18 presents the animal weight evolution since the day of the beginning of treatments in tumour bearing animals until $2\ days$ after the end of the experiments, at day 12. Animals in fact received the NP-HFn injection on day $2, 4, 6, 8,$ and 10.

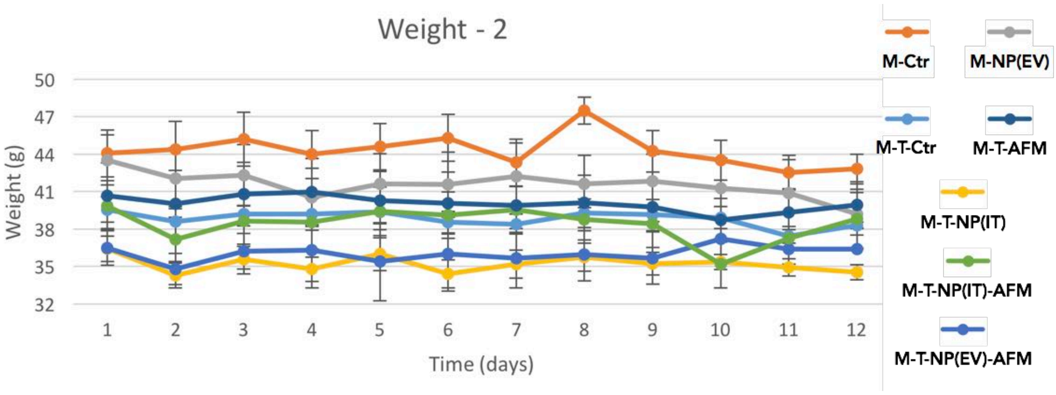

Figure 5.16: Mean weight chart of the mice groups from the beginning to 2 days after the end of the hyperthermia treatment.

Comparing control mice in group M-Ctrl and M-NP(EV), the injection of MNP-HFn had no significant effect on health animal weight. Conversely, tumour bearing mice display loss of weight during the investigate time range. This behaviour is indeed expected as the tumour itself causes severe alterations, which however appear to be partially relieved by the MFH treatment.

Figure 5.19 shows the animal weight evolution for $28\ days$ starting from the end of the treatment ($day\ 10$ of figure 5.18) in tumour bearing animals.

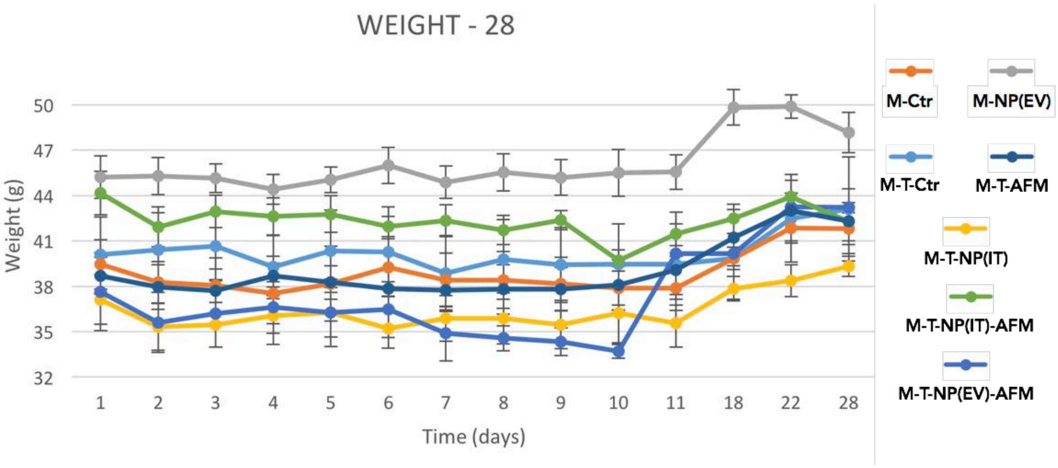

Figure 5.17: Mean weight chart of the mice groups during the 28 days after the end of the hyperthermia treatment.

These data confirm the result observed previously, that the intravenously injection of MNP-HFn did not cause alteration in the weight of healthy animals, and thus that MNP-HFn is non-toxic. If this would not be the case, indeed, we would expect some comportamental alterations which would result in a loss of weight. The uphill trend at the end of the graphics were due to the natural weight gain in the last three weeks.

The volume of tumours implanted in the mice was also monitored during the experiment. The upper panel of figure 5.20 shows the evolution of the tumour volume in the mice sacrificed two days after the last treatment and, lower panel, in mice sacrificied $28\ days$ after the ends of the treatment.

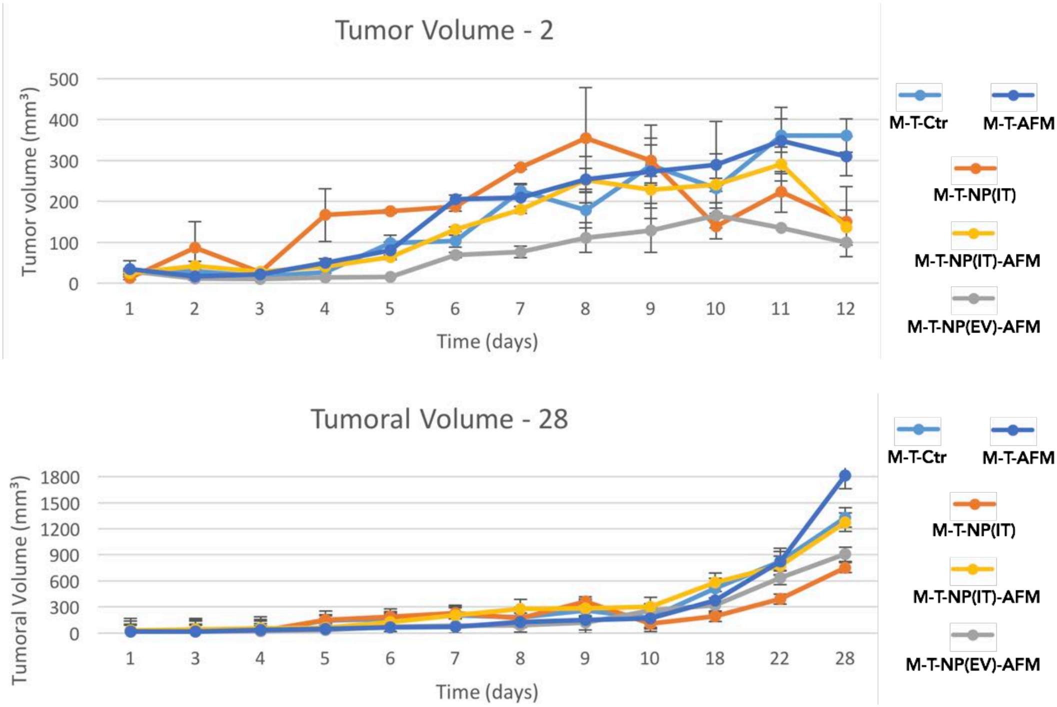

Figure 5.18: (Upper Panel) Charts of the tumour growth in mice groups from the beginning to 2 days after the end of the hyperthermia treatment. (Lower Panel) Chart of the tumour growth in mice groups 28 days after the end of the treatment.

The tumour volume steadily increases during the first part of the experiment ($days\ 1-8$) for all the groups, but in the last days of the experiment mice treated with MFH show a significant decrease in tumour size compared to the control group, the most relevant result being observed for the group treated with MFH after intravenous injection of MNP-HFn. Albeit lower, a decrease of the tumour size is also visible for M-T-NP(IT)-AFM and M-T-NP(IT). However, for longer time, after the end of the treatment, all the groups presented an increase of tumour volume. Even if the statistical set of these preliminary data is still small and there are same anomalies a clear trend emerges: treated mice present a decrease in tumour volume during the treatment and a lower increase in the regrowth after the end of the treatment. Furthermore, intravenous treatment shows a better efficacy compared to the intratumour one.

These very promising results need to be confirmed by other analyses currently in progress. Indeed, after being sacrificed the spleen, liver, brain, lung, kidney, lymph nodes, health breast and bone marrow cells and tumours were collected, for the following analysis:

- histological analysis coupled to ICP analysis, to search for possible metastasis, histological abnormalities and to reveal the biodistribution of nanoparticles;
- biochemistry and haematological blood analysis: to observe toxicity effects, such as liver, kidney and other tissue damages;
- genotoxicity and cytotoxicity analysis: to evaluate the DNA and cell damages;
- microtomography analysis to follow tumour growth evolution.

In conclusion, although preliminary, in vivo investigation has clearly shown that the administration of MNP-HFn, even when systemic (EV application) did not cause any adverse effect on mice in terms of biochemistry and haematological alteration. Most importantly, the application of an AMF even of very low amplitude, induced a partial tumour regression. These results made the nanosystem synthesized in this work an extremely appealing platform for the therapy of selected tumours such as breast cancer.

1. Fitzmaurice, C. *et al.* Global, Regional, and National Cancer Incidence, Mortality, Years of Life Lost, Years Lived With Disability, and Disability-Adjusted Life-years for 32 Cancer Groups, 1990 to 2015. *JAMA Oncol.* **3,** 524 (2017).
2. Fantechi, E. *et al.* A Smart Platform for Hyperthermia Application in Cancer Treatment : Cobalt-Doped Ferrite Nanoparticles Mineralized in Human Ferritin Cages. 4705–4719 (2014).
3. American Type Culture Collection. Available at: https://www.lgcstandards-atcc.org/.
4. Li, L. *et al.* Binding and uptake of H-ferritin are mediated by human transferrin receptor-1. *Proc. Natl. Acad. Sci.* **107,** 3505–3510 (2010).
5. Maier-Hauff, K. *et al.* Efficacy and safety of intratumoral thermotherapy using magnetic iron-oxide nanoparticles combined with external beam radiotherapy on patients with recurrent glioblastoma multiforme. *J. Neurooncol.* **103,** 317–324 (2010).
6. Thiesen, B. & Jordan, A. Clinical applications of magnetic nanoparticles for hyperthermia. *Int. J. Hyperth.* **24,** 467–474 (2008).
7. Johannsen, M. *et al.* Thermotherapy of Prostate Cancer Using Magnetic Nanoparticles: Feasibility, Imaging, and Three-Dimensional Temperature Distribution. *Eur. Urol.* **52,** 1653–1662 (2007).
8. Reilly, P. J. *Applied Bioelectricity From Electrical Stimulation to Electropathology*. **28,** (1998).
9. Abel, S. D. A. & Baird, S. K. Honey is cytotoxic towards prostate cancer cells but interacts with the MTT reagent: Considerations for the choice of cell viability assay. *Food Chem.* **241,** 70–78 (2017).
10. Behrouzkia, Z., Joveini, Z., Keshavarzi, B., Eyvazzadeh, N. & Aghdam, R. Z. Hyperthermia: How can it be used? *Oman Med. J.* **31,** 89–97 (2016).
11. Dewhirst, M. W., Viglianti, B. L., Lora-Michiels, M., Hanson, M. & Hoopes, P. J. Basic principles of thermal dosimetry and thermal thresholds for tissue damage from hyperthermia. *Int. J. Hyperth.* **19,** 267–294 (2003).
12. Dutz, S. & Hergt, R. Magnetic particle hyperthermia—a promising tumour therapy? *Nanotechnology* **25,** 452001 (2014).
13. Dewey, W. C. Arrhenius relationships from the molecule and cell to the clinic. *Int. J. Hyperth.* **25,** 3–20 (2009).
14. Festing MF, A. D. Guidelines for the design and statistical analysis of experiments using laboratory animals. *ILAR J* 244–258 (2002).

15. (OECD) guideline 474. Available at: http://www.oecd.org/daf/inv/mne/48004323.pdf.

16. Lacava, L. *et al.* Long-term retention of dextran-coated magnetite nanoparticles in the liver and spleen. *J. Magn. Magn. Mater.* **272,** 2434–2435 (2004).

17. MHA, G. *et al.* Proposal of amagnetohyperthermia system: preliminary biological tests. *J. Magn. Magn. Mater.* 2406–7 (2004).

18. Guedes MHA, Lacava ZGM, Guedes MEA, da Silva MF, M. P. Portable radio-frequency electromagnetic field generator. PI0204433-1 (2002).

19. KP, T. *et al.* Radio frequency radiation-induced hyperthermia using Si nanoparticle- based sensitizers for mild cancer therapy. *Sci. Rep.* 7034

6. The MNP-HFn as Drug Delivery system

We have demonstrated that the MNP-HFn system has a good antitumoural activity both *in vitro* and *in vivo*, when used as heat mediator in the MFH treatment. On the basis of these promising results, we attempted to imprve the cytotoxic efficiency of this platform by adding a further functionality. In particular, we exploited the capability of the internal cavity of HFn to host moderately hydro-soluble molecules, to load MNP-HFn with a chemotherapic drug, doxorubicin (DOXO), and to use it as a carrier for *in situ* delivery.

In this chapter we will describe the synthesis and characterization of this novel hybrid nano-device, MNP-HFn(DOXO) with multifold functionalities for antitumoral treatment. This system exploits on one hand the proteic component HFn(DOXO) to target cancer cells and to carry DOXO directly at the tumour site, and on the other the capability of the inorganic core to release heat upon application of an AMF and act as CA for MRI. Such a platform combines in a single system three main functionalities for the enhanced treatment of tumours, early diagnosis, drug delivery and hyperthermia therapy, constituting an ideal and powerful candidate for the theranostic approach in the tumour treatment.

6.1 Doxorubicin and Ferritin

The anthracycline antibiotic doxorubicin (Adriamycin), whose formula is sketched in Figure 6.1, was originally isolated from the fungus Streptomyces peucetius[1]. It is a chemotherapeutic drug acting as intercalating agent by inhibiting duplication of DNA and mitotic cell. DOXO has a strong activity against a wide range of human malignant neoplasms, including acute leukaemia, non-Hodgkin lymphomas, breast cancer, Hodgkin's disease and sarcomas[2]. Apart from side-effects that are common to many cancer chemotherapeutics, i.e. hematopoietic suppression, nausea and vomiting, and alopecia, the clinical usefulness of doxorubicin is largely limited by a cumulative dose-related cardiomyopathy that manifests itself as congestive heart failure[3].

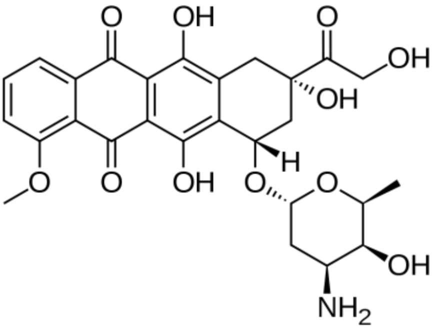

Figure 6. 1: Doxorubicin structure.

The implementation of a drug delivery system capable of an effective *in situ* release of DOXO by reducing side effects is widely discussed in the literature[4–6]. An interesting result in this sense has been recently proposed by P. Ceci *et al*. who patented an innovative encapsulation system for doxorubicin using a genetically modified HFn[7]. The HFn was genetically modified by enriching each subunit with a proline/alanine/serine (PAS) polypeptide, resulting in an enhanced capability to encapsulate DOXO with respect to wild ferritin and offering the additional benefits of higher half-life in plasma and stability[8].

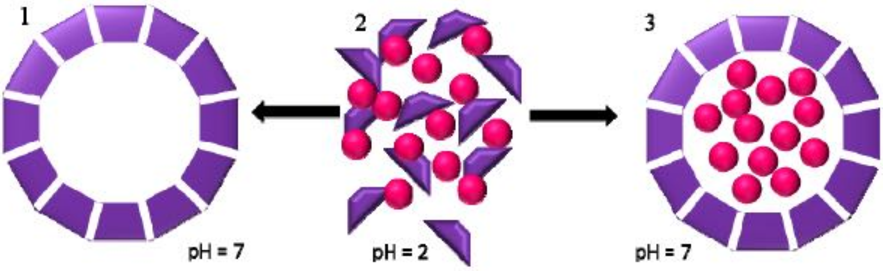

Figure 6. 2 Schematic representation of the DOXO encapsulation process. Protein in its native folding was denaturated at low pH in the presence of DOXO, then at neutral pH it recovers its folding with the cavity filled of DOXO.

DOXO was encapsulated within the protein cavity of the HFns by exploiting the protein deassembling-assembling process as a function of the pH, schematized in Figure 6.2. In physiological conditions, HFn is assembled in 24 subunits, but when the pH decreases to less than 2, the protein unfolds. If the pH is increased again up to neutrality, the protein folds back and the DOXO in the environment remains trapped within the macromolecule[9–12]. The inner surface of ferritin is charged negatively while the DOXO molecules are protonated at physiological pH, the electrostatic interaction thus favors the adsorption of the drug. Usually wild HFn can store ≈ 30 DOXO per molecules, however, when modified with PAS polypeptide, the number can increase up to 60 – 90[10]. Indeed, these disordered peptides are known to increase the stability of a number of biopharmaceutical[10].

The DOXO filled, genetically modified HFns were prepared by Dr. Pierpaolo Ceci and Dr. Elisabetta Falvo following the procedure reported in their patent7. The DOXO encapsulation in HFn cavity was also confirmed by the change of colour of the suspension (Figure 6.3).

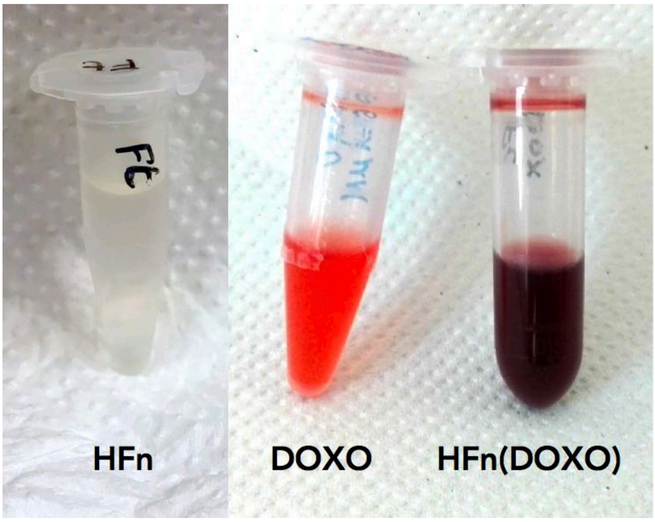

Figure 6. 3: Solutions of HFn (a) and DOXO(b) and HFn(DOXO) (c) are differently coloured (colourless, magenta and amarant respectively.

An evaluation of the amount of DOXO loaded on the HFn was obtained exploiting the optical properties of the drug. DOXO, indeed, has an absorption peak at $500\,nm$, as shown in Figure 6.4, where the UV-Vis spectrum of HFn(DOXO)disrupted in (HCl$1\,M$):(isopropyl alcool) 1:1, is reported. The amount of DOXO was then determined measuring the absorption at $485\,nm$ using a calibration curve obtained with DOXO standard solutions. We found a DOXO concentration of $2\,mM$ corresponding to 60 DOXO in each HFn, as expected.

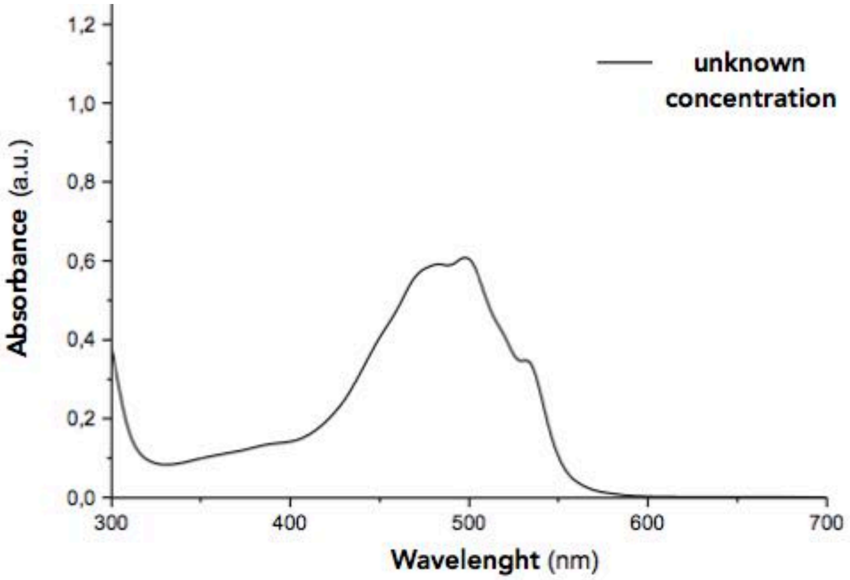

Figure 6. 4: Absorption spectrum of HFn(DOXO) solution after the denaturation.

6.2 Synthesis of MNP-HFn(DOXO)

The synthesis of MNP-HFn(DOXO) was performed following the same steps used for MNP-HFn and described in chapter2.1. In the next paragraphs are briefly described the characterization of the MNPs, the synthesis and characterization of MNP-HFn(DOXO) and the preliminary *in vitro* analysis of its antitumoral activity.

6.2.1 Synthesis and characterization of MNP-HFn(DOXO)

The MNPs were synthesized by thermal decomposition of $Fe(acac)_3$using the same conditions described in Chapter 2.1. In a 3 neck flask $8\,mmol$ of $Fe(acac)_3$, $8\,mmol$ of oleic acid (OA) and $8\,mmol$ of oleylamine (OAm), were dissolved in $110\,mL$ of benzylether and the reaction mix was heated under a flux of nitrogen up to $200\,°C$ in $15\,min$, kept at this temperature for$30\,min$, and finally heated to reflux and kept there for $1\,h$. The MNPs powder, named in the following MNP-6, was washed 3 times with isopropyl alcohol, dried and analysed by XRD. The XRD diffraction pattern of MNP-6, shown in figure 6.5, matches that of bulk magnetite. The Pawley analysis of the pattern gives a lattice parameter $a = 8{,}403$ Å and crystal size $d = 15{,}6\,nm$.

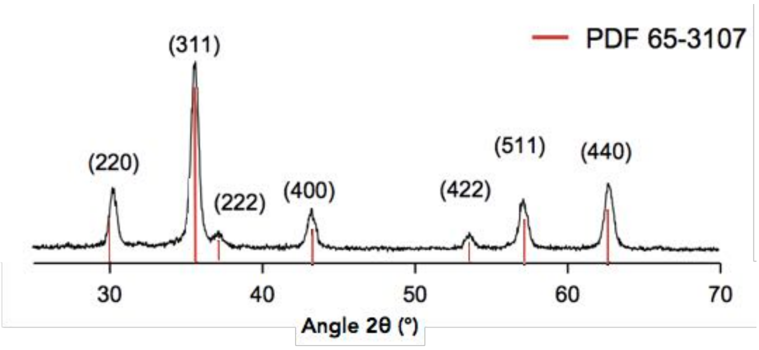

Figure 6. 5: XRD Patterns of samples MNP-6. The red bars correspond to the reference pattern of magnetite (PDF 65-3107)

The statistical analysis of diameter performed on TEM micrographs, gave the size distribution shown in figure 6.6. MNP-6 has a broad distribution centred at $d_{TEM} = 13{,}8 \pm 2{,}1\,nm$ and the MNP shape is faceted. The fitting of the distribution with a Log Normal function gave a mean size $d_{LN} = 13{,}6 \pm 0{,}1nm$

with standard deviation$\sigma_{LN} = 0{,}13 \pm 0{,}01$. Data obtained from the XRD and TEM analysis are reported in Table 7.1.

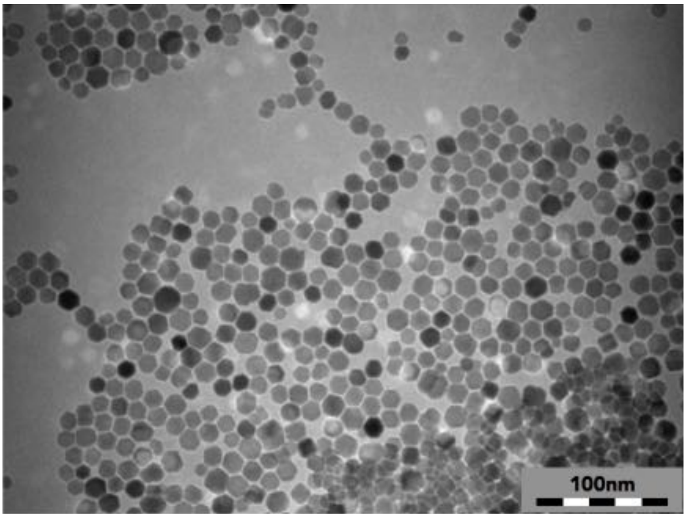

Figure 6. 6: A selected TEM micrograph of MNP-6, and the corresponding size distribution of diameter obtained by a statistic over several images; the average diameter is $d_{TEM} = 13{,}6 \pm 2{,}1\ nm$;the black thick line is the fitting to a log normal function with $d_{LN} = 13{,}7 \pm 1{,}8\ nm$

Sample	**Crystal size (nm)**	**Lattice Parameter Å**	d_{TEM} **(nm)**	d_{LN} **(nm)**	σ_{LN}
MNP-6	$15{,}6$	$8{,}403(1)$	$13{,}6 \pm 2{,}1$	$13{,}7 \pm 1{,}8$	$0{,}130$

Table 6. 1: Crystal size and lattice parameter obtained from the XDR patter fit with the Pawley method using T.O.P.A.S.® software, for MNP-6. d_{TEM} is the mean diameter obtained from statistical analysis of the size measured on TEM micrograph; $\boldsymbol{d}_{LN}$ the mean diameter and σ_{LN}, standard deviation from the fit to a Log Normal distribution.

As previously discussed high crystalline MNPs of this size are optimal candidate for nano-medical application. MNP-6 was coated with APPA by ligand exchange, and dispersed in water. The magnetic properties of MNP-6@APPA were investigated using a SQUID magnetometer, by recording the dependence of magnetization on temperature (ZFC-FC), and on the applied field at room temperature and $2{,}5$ K.

The ZFC-FC, reported in Figure 6.7a, showed the typical behaviour expected for a MNPs system blocked at room temperature. Conversely, the hysteresis loop recorded at room temperature, (Figure 6.7 b), displays no magnetic irreversibility, indicating the MNP-6are superparamagnetic at room temperature on this time scale.

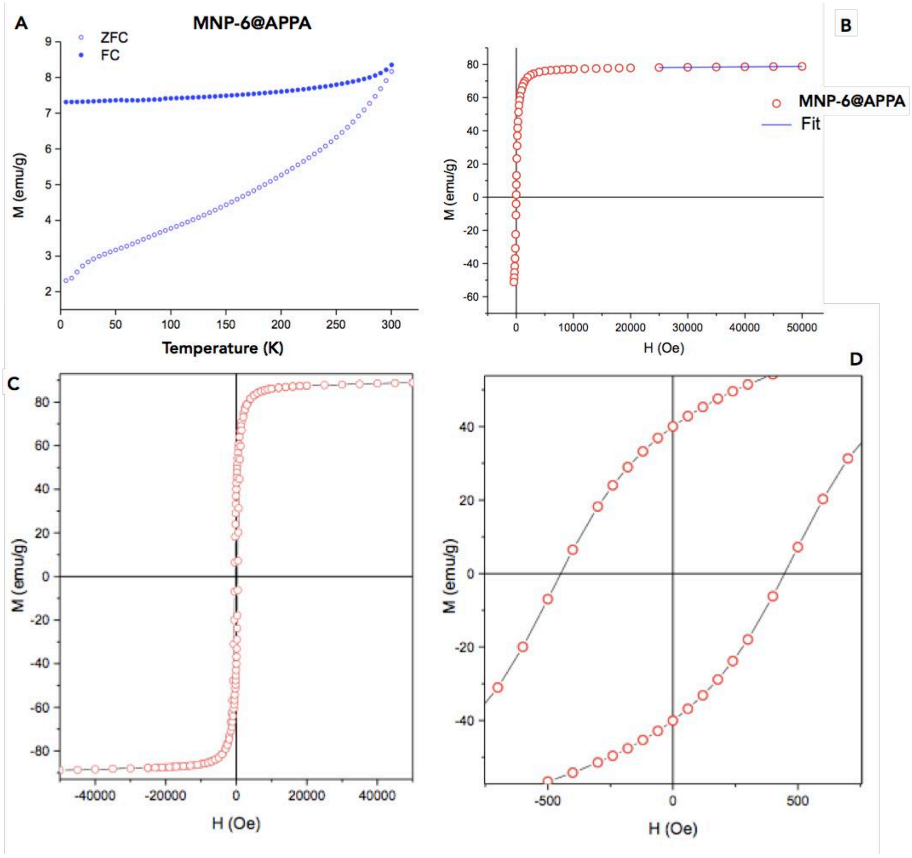

Figure 6. 7: Magnetic properties of MNP-6: A) Temperature dependence of the ZFC-FC magnetizations, (empty and full symbols refer to ZFC and FC magnetizations, respectively); B) Magnetization recorded at room temperature; C) Hysteresis loop recorded at$2,5\ K$*; D) Details of the hysteresis loop in the low field region.*

Figures 6.7 c and d, show the hysteresis loop recorded at low temperature and the low field detail, respectively, while the parameters extracted from the loop (saturation and remnant magnetisations and coercive field) are reported in table 6.2. The MNPs saturate rapidly, reaching a high value both at low and high temperature, $86\,emu/g$ and $80\,emu/g$, respectively. Overall, MNP-6 showed notable magnetic properties for the desired applications, especially a high M_S. The coercive field of MNP-6 is similar to those previously recorded for MNPs coated with APPA.

Sample	$\mathbf{M_S\,300K\,(emu/g)}$	$\mathbf{M_S 2,5K\,(emu/g)}$	$\mathbf{H_C\,(Oe)}$	$\mathbf{M_{0T}/M_{5T}}$
MNP-6	80,0	86,4	448	0,45

Table 6. 2: Magnetic saturation, M_S extrapolated from magnetization curves at room temperature (300 K) and low temperature(2,5 K); Coercive Field, H_C, and remnant magnetizationM_{0T}/M_{5T} obtained fromthe hysteresis loop. M_S is given as emu per g of magnetc material.

The hyperthermic properties of aMNP-6water suspension, $5\,mg/mL$, were investigated by recording the kinetic curve during the application of an AMF ($17\,kAm$, $183\,kHz$) as shown in Figure 6.8. The SAR value calculate with equation 8 chapter 3.1 was $124{,}0 \pm 2{,}0\,Wg^{-1}$, a heat power good enough for MFH treatments.

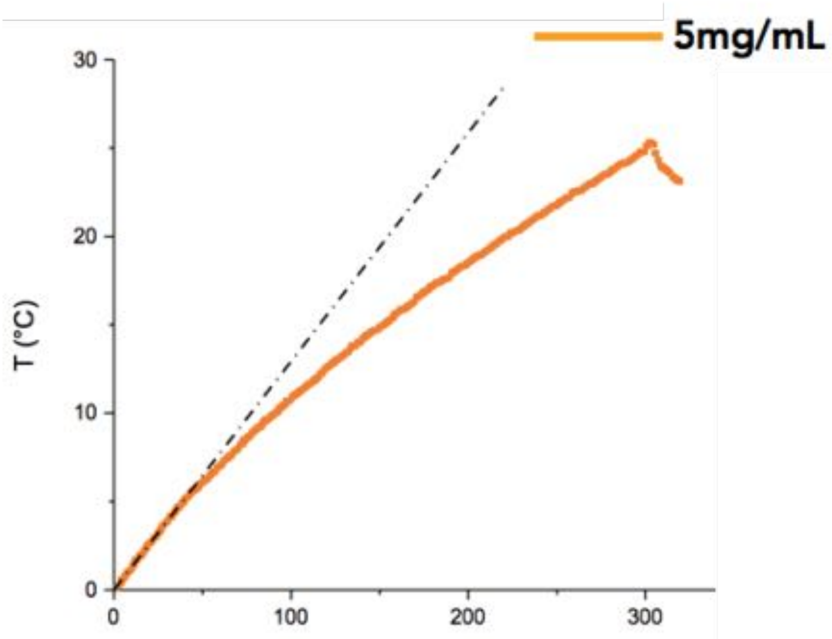

Figure 6. 8: : Temperature evolution of a MNP-6 water suspension (concentration $5\ mg/mL$*)*

After verifying good magnetic characteristics and the hyperthermic efficiency of MNP-6 we proceeded with the functionalization with HFn(DOXO), following the same steps described in chapter 4.2.

First, MNPs@APPA was reacted with the crosslinker in PBS suspension at pH 7.2. After $30\ min$ the unreacted reagent was removed by magnetic precipitation of the MNPs@PEG, which was washed twice with H_2O_{MilliQ}. Then, HFn(DOXO) was added ($0{,}50\ \mu M$) in PBS solution at pH 7.2 and after $60\ min$ the excess of HFn(DOXO) was removed by washing with PBS(10X). MNP-HFn(DOXO) was magnetically precipitated and washed twice with H_2O_{MilliQ}.

The functionalization yield in number of HFn(DOXO) for MNPs, evaluated by IPC analysis of Fe, was 3:1. The measurement of the magnetic properties indirectly confirms this result, M_S being reduced by 20% both at $300\ K$ and $2.5\ K$ (from $79{,}8\ emu/g$ to $63{,}8\ emu/g$ at $300\ K$ and from $90{,}7\ emu/g$ to $73{,}7\ em/g$ at $2{,}5\ K$, Figure 6.10).

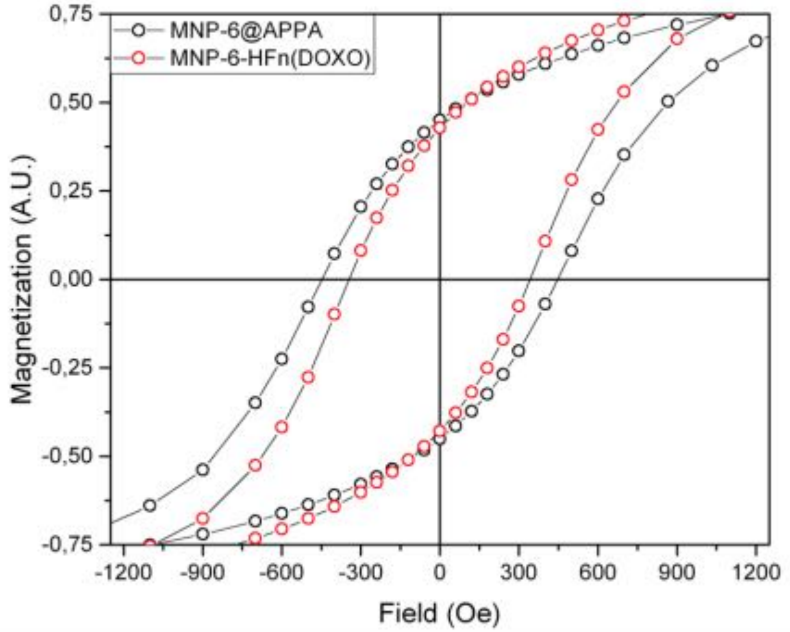

Figure 6. 9: Low field detail of the hysteresis loop recorded at $2{,}5\ K$*, for MNP-6@APPA (black circles) and MNP-6-HFn(DOXO)(red circles).*

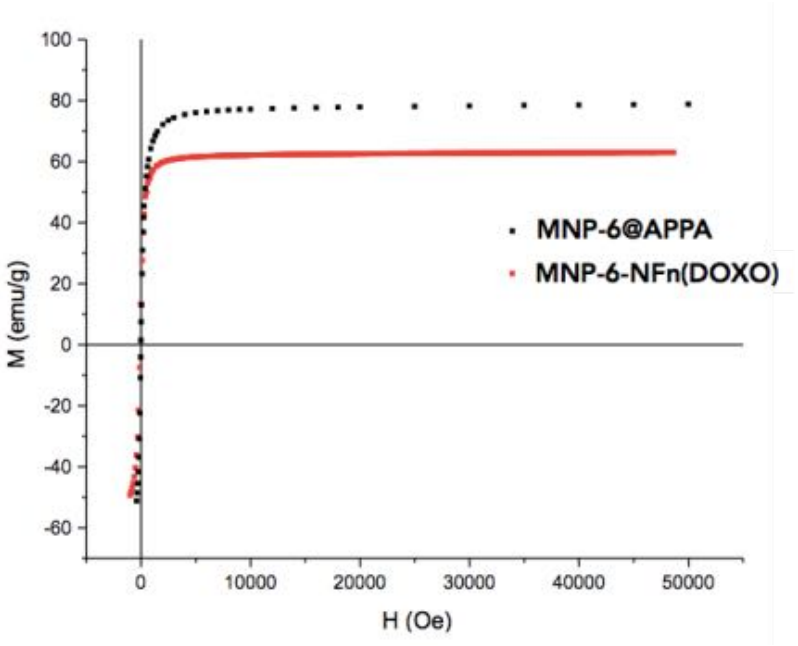

Figure 6. 10: Magnetization recorded at room temperature for MNP-6@APPA (black circles) and MNP-6-HFn(DOXO) (red line).

6.2.2 Stability of the MNP-6-HFn(DOXO)

Before performing the *in vitro* study, it is necessary to accurately verify the amount of DOXO actually carried per unit of system. This analysis is required to check the stability of DOXO into the HFn during the synthetic procedure. In addition, we wish to verify the behaviour of the MNP-HFn(DOXO) when exposed to the AMF, and particularly to detect if DOXO is partially released during the MFH treatment as result of protein denaturation due to heat.

The quantity of DOXO loaded in the nano-system was evaluated by optical absorption measurements. Since, absorption of the magnetite in the $350-650\ nm\ \lambda$ range (Figure 6.11) is so intense that does not allow an easy evaluation of the absorbance of the anthracycline molecule, the inorganic component was removed by protein denaturation with hydrochloric-isopropylic solution and magnetic separation.

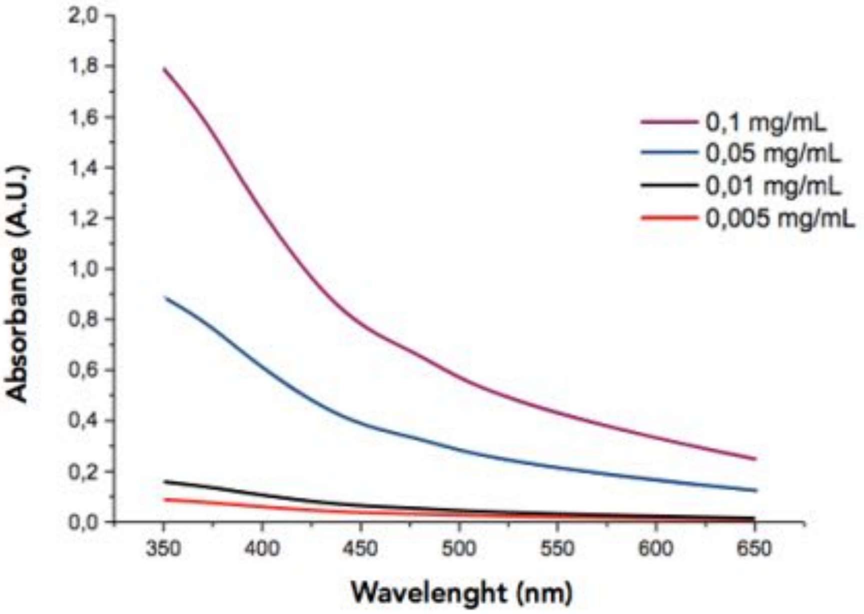

Figure 6. 11: MNP suspensions absorption spectra, conc. $100-50-10-5\ \mu g/mL$.

From the absorbance at $532\ nm$ we evaluated a concentration of DOXO $12\ \mu M$, which, considering there are 3 HFn per MNP, corresponds to 60 molecules of DOXO per HFn. Thus, this data confirms the stability of the HFt (DOXO) during the functionalization process and over the time as reported by *Falvo et al*.[10] (Figure 6.12).

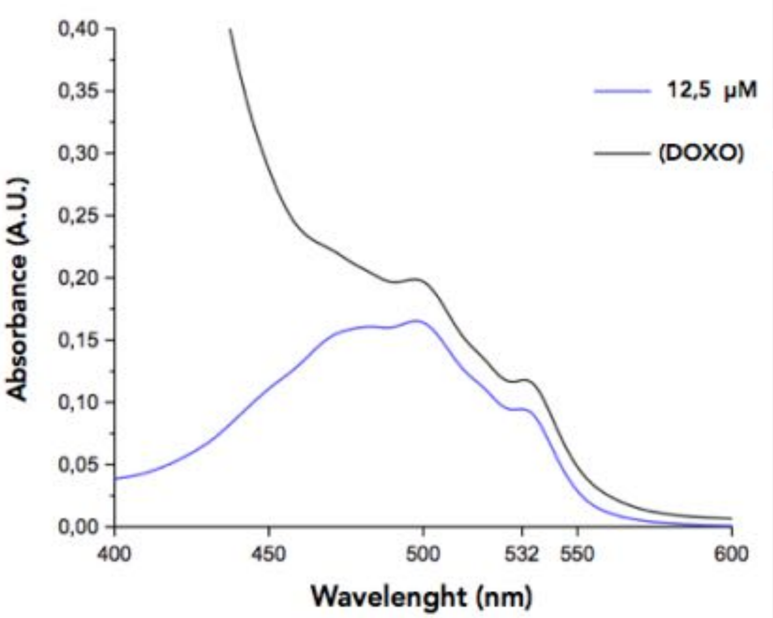

Figure 6. 12: Acid solution of denatured protein absorption spectra compared to DOXO $12{,}5\ \mu M$ *solution. It is well evident the interference of. MNP impurity. In order to reduce the interference, we choose the* $532\ nm$ *peak.*

The drug release tests under the AMF action was performed as follows: 1 mL of MNP-HFn(DOXO) suspension at concentration of 1 mg/mL was exposed to an AMF of $183\ kHz$ frequency and $17\ kAm^{-1}$ amplitude at body temperature ($37\ °C$). The evolution of temperature is shown in figure 6.13.

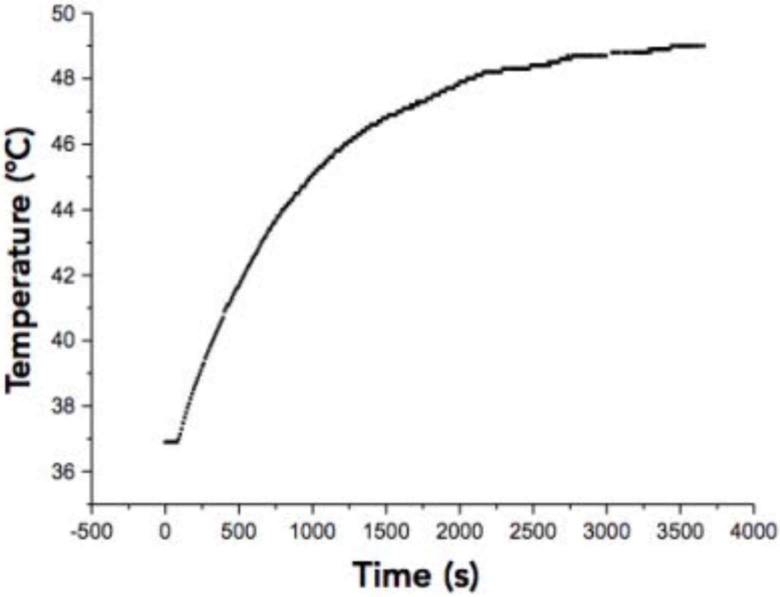

Figure 6. 13: : Temperature evolution of a MNP-HFn(DOXO) water suspension under the application of an AMF.

After 1h the temperature reached almost 49°C, a remarkable value well above the cell resistance. The magnetic material was then magnetically separated from the surnatant. The optical spectrum of the surnatant is shown in figure 6.14.

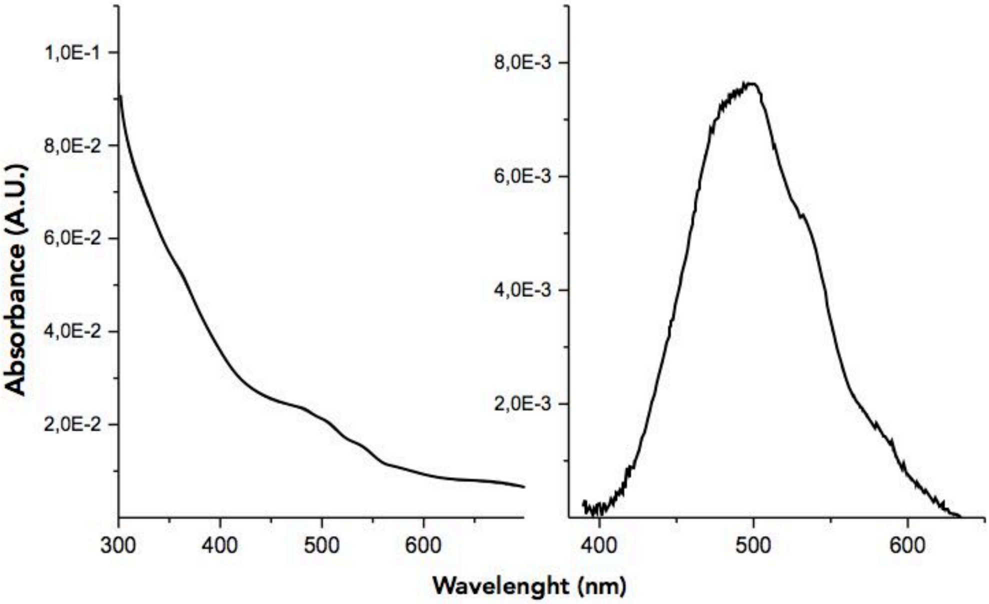

Figure 6. 14: a) Absorption spectrum of surnatant; b) Doxo signal after the subctraction of the MNPs component.

After subtraction of the signal of residuals MNPs, realized by spline interpolation of the bottom line, (Fityk 0.9.8 software), we determined that the drug released during hyperthermic treatments was equal to $4\ \mu M$, which is $\approx 10\ \%$ of the DOXO contained within ferritins. Hyperthermic treatment seems therefore unable to promote full protein denaturation, particularly in view of the lower temperatures reached in the treatment. However, this does not represent a problem as, once internalized, the digestive action of cellular enzymes can cause the full release of the drug. Moreover, as previously pointed out, HFn are very heat-resistant[13,14] but easily denaturise when the pH decreases.

6.2.3 In vitro test: internalization and antitumoural efficacy of the drug loaded nano-system

The tests performed so far on MNP-HFn(DOXO) have shown chemical-physical and magnetic properties, stability, functionalization level, and hyperthermic efficiency comparable to those of the drug-free analogous. Thus, we proceeded with *in vitro* tests, which were performed on MDA-MB-231 breast cancer cells, following the same protocol described in scheme 5.1, These tests were performed in collaboration with Barbara Tenci and Dr. Lorenzo Di Cesare Mannelli at the laboratory of Farmacologia e Tossicologia Dip. Di Neuroscienze, Psicologia, Area del Farmaco e Salute del bambino (NEUROFARBA) dell'Università di Firenze.

At first we performed the viability test by treating cells with increasing concentrations of MNP-HFn(DOXO) in order to find the best concentration of heat mediators which produces an hyperthermic effect without masking the possible synergy with the drug action. $400\ K$ cancer cells were trypsinizated and detached from the cultivation flask, and then suspended in $0{,}5\ mL$ of 1:1 mix of DMEM and physiological solution containing 5% BSA. Samples were incubated with 1 or $0{,}3\ mg/mL$ MNP-HFn(DOXO), that correspond to $171,\ 57{,}1$ or $17{,}1\ \mu M$ of free DOXO for the other samples. After $3\ h$ of treatment, which corresponded to the time that would be required in a MFH experiment for incubation, field application, plus one hour of further incubation to increase the efficacy of DOXO, the samples were washed from the treatment and incubated for the viability test. As a control the test was also carried on cells incubated with the same concentration of HFn(DOXO), MNP-HFn and free DOXO.

In figure 6.14, are shown the results of the MTT viability test performed after $48\ h$.

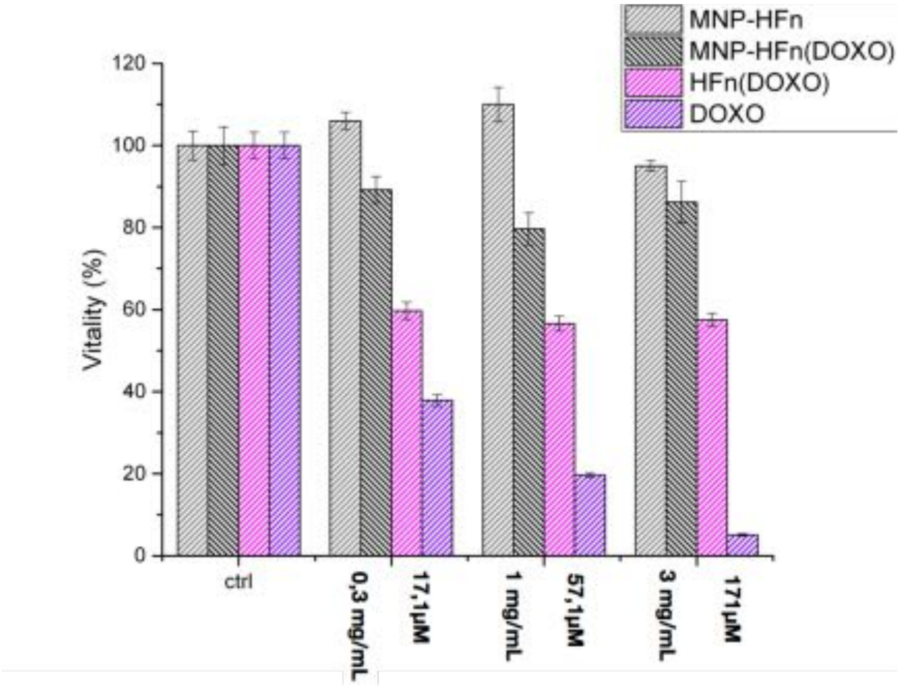

Figure 6. 15: MTT MDA-MD-231 cells viability test 48h after the incubation with MNP-HFn (light grey bar); MNP-HFn(DOXO) (dark grey bar); HFn(DOXO) (magenta bar); DOXO (purple bar). Each value is normalized to the corresponding control sample.

Cells treated with MNP-HFn show no significant mortality, giving proof that, even after modification with PAS, MNP-HFn is biocompatibile. The culture incubated with DOXO alone show a dose dependent decrease in cell viability ($38 - 20 - 5\ \%$), which is explained by the systemic action of the drug in direct contact with the cells. The viability of cells treated with HFn (DOXO), instead, does not depend on the amount of drug, as it decreases for all samples of about 40%. That effect is justified by the release of the drug due to the internalized ferritin disruption. The absence of a dose-dependent is consistent with the internalization mechanism of HFn, within the $3\ h$ of incubation. Indeed, during this time the turnover of the receptors on the membrane is saturated, so that the amount of HFn(DOXO) internalized is the same. This result indirectly confirms that, as expected, only the HFn(DOXO) internalized into the cell release the drug payload. Finally, no effect was detected in cultures incubated with

MNP-HFn(DOXO). This can be attributed to a low degree of internalization of the nano-device. Indeed, when we verified the degree of internalization of MNP-HFn by fluorescence microscopy we did not observe any relevant amount of MNP-HFn(DOXO) into the tumour cell.

This unpredicted result may be justified considering the lower number of HFn attached at the MNP surface with respect to the unloaded counterpart. The presence of PAS in the HFn used to increase the DOXO load may have modified the capability of the protein to be grafted onto the MNPs, as the ratio HFn(DOXO):MNP ($3:1$) is lower compared to HFn:MNP ($4:1$ or $6:1$). The lower number of ferritin and the presence of PAS then could also affect the interaction between the TfR1 receptor and the nano-system, making its internalization more difficult.

As a matter of fact, the lack of internalization on one hand, and the low dose of DOXO released during the hyperthermia treatment, hamper at present the in vitro validation of this nano-device as a multifunctional agent for the therapy of tumour.

Future studies need to be focused on optimizing the synthesis of MNP-HFn(DOXO) to increase the number of HFn and then the degree of internalization. Possibly strategies will be to select a HFn(DOXO) with different degree of enrichment of PAS or to use HFn(DOXO) genetically or chemically modified to provide them with a specific targeting agent for the selected cell line.

1. ARCAMONE, F., CASSINELLI, G. & FRANCESCHI, G. Structure and physicochemical properties of adriamycin (doxorubicin). *Int. Syrup. Adriamycin* 9–22 (1972).
2. YOUNG, R. C., OZOLS, R. F. & MYERS, C. E. The anthracycline antineoplastic drugs. *New Engl. J. Med.***305,** 139–153 (1981).
3. Keizer, H. G., PINEDO, H. M., SCHUURHUIS, G. J. & JOENJE, H. DOXORUBICIN (ADRIAMYCIN): A CRITICAL REVIEW OF FREE RADICAL-DEPENDENT MECHANISMS OF CYTOTOXICITY. **47,** 219–231 (1990).
4. Shen, J., Wolfram, J., Ferrari, M. & Shen, H. Taking the vehicle out of drug delivery. *Mater. Today***20,** 95–97 (2017).
5. Lehner, R., Wang, X., Marsch, S. & Hunziker, P. Intelligent nanomaterials for medicine: Carrier platforms and targeting strategies in the context of clinical application. *Nanomedicine Nanotechnology, Biol. Med.***9,** 742–757 (2013).
6. Falvo, E. *et al.* Antibody-drug conjugates: targeting melanoma with cisplatin encapsulated in protein-cage nanoparticles based on human ferritin. *Nanoscale***5,** 12278–12285 (2013).
7. Ceci, P. & Falvo, E. A FUSION PROTEIN, A NANOPARTICLE COMPOSED BY A PLURALITY OF MONOMERS OF SAID FUSION PROTEIN, AND USES THEREOF. (2016).
8. Vannucci, L., Falvo, E. & Ceci, P. Multifunctional Protein-Based Nanoparticles for Cancer Theranosis. **7,** 231–253 (2014).
9. Vannucci, L. *et al.* In Vivo Targeting of Cutaneous Melanoma Using an Melanoma Stimulating Hormone-Engineered Human Protein Cage with Fluorophore and Magnetic Resonance Imaging Tracers. **10,** 1–12 (2014).
10. Falvo, E. *et al.* Improved Doxorubicin Encapsulation and Pharmacokinetics of Ferritin – Fusion Protein Nanocarriers Bearing Proline, Serine, and Alanine Elements. (2016). doi:10.1021/acs.biomac.5b01446
11. Bellini, M. *et al.* Protein nanocages for self-triggered nuclear delivery of DNA-targeted chemotherapeutics in Cancer Cells. **196,** 184–196 (2014).
12. Fracasso, G. *et al.* Selective delivery of doxorubicin by novel stimuli-sensitive nano-ferritins overcomes tumor refractoriness. **239,** 10–18 (2016).
13. Fan, K. *et al.* Magnetoferritin nanoparticles for targeting and visualizing tumour tissues. *Nat. Nanotechnol.***7,** 459–64 (2012).
14. Uchida, M. *et al.* Targeting of Cancer Cells with Ferrimagnetic Ferritin Cage Nanoparticles. **312,** 16626–16633 (2006).

7. Conclusion and Perspective

The aim of this research was the synthesis of a multifunctional device based on MNPs functionalized with ferritins, capable to target tumours and to act both for early diagnosis by MRI, and therapy of tumours by magnetic fluid hyperthermia. The originality of this work is the use of ferritin, that makes the final nano-device biocompatible, capable of being selectively internalized in the tumour cells and able to circulate for a long time in the bloodstream. Finally, a further advantage is provided by the possibility of exploiting the ferritin cavity as a container for the delivery of antitumoral drugs.

To achieve this goal, we synthesized iron oxide MNPs by thermal decomposition of metalorganic precursors in high boiling solvent, namely, iron acetylacetonate in benzylether. This technique allowed us to produce quasi-monodisperse, high-crystalline magnetite MNPs of controlled size, which are key features for the clinical application of MNPs. Moreover, we investigated the role of the different synthetic parameter in order to find the best condition to obtain inorganic core suited for the biomedical application. The high quality of the MNPs, such as the high magnetic saturation at room temperature were confirmed by magnetometric measurements, which also allowed us to describe the superparamagnetic behaviour of the samples.

Functionalization of MNP surface was carried out exploiting a phosphonate ligand with a free amino group, which has a great affinity toward iron oxide, and gives both hydrophilicity and a binding site for the further functionalization with ferritin. The MNPs chosen as magnetic cores selected for the functionalization with ferritin are those which have showed the greatest hyperthermic capability in magnetic hyperthermia experiments and a better efficiency in increasing image contrast in MRI in comparison to commercial contrast agents, such as Endorem®. Furthermore, it is particularly relevant that the chosen MNPs maintain the high hyperthermic efficiency even in a strongly viscous environment, as demonstrated by tests performed on agarose gel suspensions. This is a crucial result, indeed, since in the physiological environment like intracellular fluid and extracellular matrix, i.e. the final target of the nano-device, no mechanical rotation is allowed.

Ferritins were then bound to the MNPs thanks to a heterobifunctional PEG ligand that selectively reacts with the amino groups on the surface of the MNP and the thiol groups onto the ferritin. The success of the MNP-HFn conjugation was confirmed by using different techniques as electrophoresis on agarose gel, DLS, AFM, ICP, CHN and magnetometric measurements. In particular, DLS data showed that the hydrodynamic radius of the MNP-HFn is lower than 100 nm, ideal for the colloidal stability of the water suspension and for a long circulating half-life, as confirmed by *in vitro* and *in vivo* experiments.

The MNP-HFn system was tested both *in vitro* and *in vivo* to verify its antitumoural efficiency. *In vitro* tests were carried out on prostate and breast cancer cell lines, two tumours that represent almost the 25% of all cancer cases and that overexpress the transferrin receptors TfR1, able to internalize the ferritin into the cytosol. The internalization capability of our system was confirmed by confocal microscopy of cells incubated with rhodamine-labelled MNP-HFn sample. Then, the cells samples were exposed to AMF of intensity and frequency and for exposure times similar to those used in clinical trials. We found that MNP-HFn was able to efficiently kill cancer cells only when its concentration allowed reaching and maintaining the temperature of the cell culture at 43°. To better understand this behaviour, we verified the thermal damages suffered by cells when heated at different temperature without the application of an AMF. We found that the damages produced when the cells are heated up to 44° are lower than those observed in MFH treatments and thus, we cannot exclude that internalized MNPs provide an additional contribution to cell death by producing a direct inner damage, which enhances the effect of the treatment. This is an important indication that deserves further in-depth study. The knowledge of the mechanism of cell death is also pivotal to establish the best strategy to follow for the administration of the nano-device. If internalization is fundamental to enhance the treatment efficiency, then an active targeting that permits to cross the cell membrane has to be preferred, while it becomes less relevant the nano-device accumulation in the extracellular matrix obtained by EPR effect.

Finally, we present the results of the preliminary *in vivo* investigation realized on mice inoculated with Enrilch tumour cells, a mice cancer type of mammary origin. MNP-HFn were injected via intravenous or intratumoural administration in mice, which were then exposed to an AMF every two days for ten days. The tumours size was checked along the following months together with mice general clinical conditions. This investigation has clearly shown that the administration of MNP-HFn, even when systemic (intravenous application), did not cause any adverse effect on mice in terms of biochemistry and haematological alteration. Most importantly, the application of an AMF even of very low amplitude, induced a partial tumour regression, at last during the first days after the treatments. These promising preliminary results must be confirmed by further analysis: histological analysis, genotoxicity analysis, cytotoxicity analysis and microtomography analysis are currently in progress and will also give us information on the fate of the nano-device providing the biodistribution in the mice. Even if partial, the obtained results made the nano-system synthesized in this work an extremely appealing platform for the therapy of tumours such as breast cancer.

The final part of this work is dedicated to the “step further” of the ferritin capabilities exploiting, which consists in enhancing the antitumoral activity of the MNP-HFn system using HFn, PAS enriched, filled with a chemotherapic drug, doxorubicin. Following a procedure similar to that described for MNP-HFn, we successfully synthesized the drug loaded analogue, MNP-HFn(DOXO).

We proved that this system releases DOXO in an acid environment, such that of lysosome, while it is extremely stable during the hyperthermia application. Unfortunately, this new system, unlike the previous one, was not efficiently internalized by the cancer cells, preventing us from proceeding with the *in vitro* evaluation of the combined antitumoural activity. We hypothesize that the lower number of ferritin and the different HFn structure could affect the interaction between the cell membrane and the nano-system, making its internalization more difficult. Different strategies must be investigated in the future in order to improve the internalization of MNP-HFn(DOXO). For example we plan to use a HFn(DOXO) with different degree of enrichment of PAS or a HFn(DOXO) genetically or chemically modified which exposes a specific targeting agent for the selected cell line.

In conclusion, in this thesis we have presented a novel hybrid magnetic nano-device for theranostic application in biomedicine. Although we have demonstrated the great potential of this system, there are still many aspects which deserve further investigation. In particular, further studies will be dedicated to the damages suffered by the cells under MFH application and to distinguish the thermal effect from the contribution from internalized magnetic cores. On the other hand, a deep analysis of the result of *in vivo* tests will allow clarifying the actual potentialities and possible issues related to the use of MNP-HFn, with a special attention to the biodistribution and genotoxicity. Finally, we will investigate the drawbacks encountered during the functionalization of the MNPs with HFn(DOXO), revising the synthesis and, once improved the internalization degree, we will assess its antitumoural activity.

8. Materials and methods

8.1. Materials

All chemicals were of analytical quality purchased from Sigma-Aldrich Co.. Water was deionized and filtered with a Milli-Q System (Merck Millipore Co., Germany). Except for SM(PEG)$_{12}$ Crosslinker purchased from ThermoFisher Scientific.

8.2. Methods

8.2.1 Preparation of Fe_3O_4 MNPs

The iron oxide MNPs were synthesized by thermal decomposition of metal-organic precursors in high boiling solvents, in the presence of surfactant. In a typical reaction, Iron(III) acetylacetonate ($2{,}83\ g,\ 8{,}0\ mmol$), Oleylamina ($10{,}72\ g, 40\ mmol$) and Oleic Acid ($11{,}23\ g,\ 8{,}0\ mmol$) were dissolved in Benzilether ($100 - 110mL$) stirred and purged under nitrogen flow for $15\ min$ at r.t.; the mixture was heated at $200\ °C$ for $30\ min$ and then to $300\ °C$ for a period of time sufficient to produce nanoparticle of the desired size. Indeed, at $200\ °C$ we have the production of the monomer and the making of crystal seeds (nucleation phase), while at $300\ °C$ the dimension of the seeds increases due to the supersaturation of the monomer (growth phase). The mixture was cooled down to r.t., the black MNPs precipitate was magnetically separated, cleaned three times with ethanol and suspended in Toluene.

8.2.2 Coating exchange of Fe_3O_4 MNPs

A coating exchange was performed using 3-AminoPropylPhosphonic Acid (APPA) a ligand that permit both a firm covalent bond between the MNPs and the ligand itself and give a free amino group for the further functionalization.

Typically, $4mL$ of Toluene suspension of MNPs ($10\ mg/mL\ Fe_3O_4$) were mixed with $4mL$ of dichloromethane solution of APPA ($10\ mg/mL$) and Tetramethylammonium hydroxide (TMAOH, $10\ mg/mL$) and sonicated for one hour. Then MNPs were magnetically separated, cleaned with ethanol and suspended in water.

8.2.3 Functionalization of Fe_3O_4 MNPs with HFn

The covalent junction between HFt and MNPs@APPA were obtained by using a heterobifunctional crosslinker $SM(PEG)_{12}$ (Thermofischer NHS-PEG-MAL) in witch N-hydroxysuccinimide (NHS) ester react specifically with free amino groups onto MNPs side while maleimide (MAL) group react specifically with the thiol group onto the HFt molecules. The two reactive group were separated with a $7{,}5\ kDa$ polyethylene glycol (PEG) spacer was used to improve water solubility of the conjugate, and to minimize possible steric hindrance between APPA MNPs and ferritin molecules during conjugation. MNP-HFt conjugates were prepared by a two-step reaction scheme. First, MNPs@APPA ($0{,}1\ \mu M$ in amino groups) was reacted with $50-fold$ molar excess of the crosslinker in PBS suspension at pH 7.4 at room temperature sonicating for 30 min. The excess (non reacted) reagent was removed by magnetically precipitating the MNPs@PEG and cleaned with H_2O_{MilliQ} twice. Second, cysteine-containing HFt was added ($0{,}25\ \mu M$, final concentration) in PBS solution at pH 7.4, and sonicated for 60 min at room temperature allowing to react with the MAL groups present on the modified APPA NPs molecules. The excess (non reacted) of HFt was removed by washing the MNP-HFt with PBS magnetically precipitating the MNP-HFt and cleaned with H_2O_{MilliQ} twice. The MNP-HFt samples were maintained sterile heating at $60\ °C$ for $20\ min$.

8.2.4 Functionalization MNP-HFn with rhodamine

Exploiting the free amino groups of lysine onto the HFt surface, MNP-HFt were been labelled with NHS-Rhodamine to be used as fluorescent dye and verify the capability of the sample to be internalized by the cell. MNP-HFt-Rhd were been prepared by adding NHS-Rhodamine DMSO solution ($20\, mM$, final concentration) to a MNP-HFt $0{,}5\, mg/mL$ PBS suspension and sonicating for $30\, min$. The excess (non reacted) dye was removed by magnetically precipitating the MNP-HFt-Rhd and cleaned with H_2O_{MilliQ} four times.

8.3 Characterization methods

X-Ray Diffraction

Powder X-ray diffraction (XRD) measurements were carried out using a Bruker D8 Advance diffractometer equipped with Cu Kα ($1{,}54178\, Å$) radiation and operating in $\theta - 2\theta$ Bragg–Brentano geometry at $40\, kV$ and $40\, mA$. Lattice parameters were evaluated on averaging over (400), (511) and (440) peaks. The determination of the mean crystallite diameter, *d*, was performed using the Scherrer equation,$d = (0.9\lambda)/(\beta\, cos\theta)$, where λ is the wavelength of the incident X-ray ($1{,}54178\, Å$), θ the diffraction angle, and β the full-width at half-maximum. The quantification of the phase percentage was obtained analyzing the diffraction pattern by the Rietveld method with TOPAS software.

TEM

The average diameter and size distribution of MNPs were determined from Transmission Electron Microscopy (TEM) images recorded using a CM12 PHILIPS transmission electron microscope operating at $100\, kV$ using a LaF_6 source. Samples were prepared by drop drying a dilute toluene solution of

MNPs onto 200 mesh carbon-coated copper grids. The recorded micrographs were processed by means of the iTEM TEM Imaging Platform software (Olympus), and were further analysed with the FIJI open software. The mean diameter and size distribution of the sample was obtained from a statistical analysis over 800 MNPs.

Electrophoresis

The bond between MNPs and HFt were obtained by using agarose gel electrophoresis experiments. In order to resolve the MNP-HFt complexes, electrophoresis was carried out on $1\,\%$ agarose gels in $0{,}04\,M$ Tris-acetate buffers at a constant voltage of $80\,V$ at r.t.. The gels were unstained or stained with Coomassie blue to visualize MNPs and protein band relative contributions.

Atomic Force Microscopy

Atomic Force Microscopy (AFM) measurements were carried out using a NT-MDT Solver P47 PRO; samples were drop-casted on a fresh prepared mica surface and studied with a AFM *noncoated Si goldbackcoated 10* (NSG10) probe in tapping mode. Images were elaborated with WSxM software.

Dynamic Light Scattering

Dynamic Light Scattering (DLS, Malvern Zetasizer ZS, Malvern Instruments Ltd., UK) measurement, Z-pot analysis and size distribution, were carried out on $0{,}5\,mg/ml$ suspension of the samples.

Fluorescence spectroscopy

The presence of Rhodamine were been verify by recording in $555 - 655\,nm$ interval the UV spectra ($\lambda^* = 550\,nm$ exciter) of MNP-HFt-Rhd diluted solution (LS55 Luminescence Spectrometer, Perkin Elmer, Massachusetts U.S.).

UV-Vis Absorbance spectroscopy

The absorbance analysis were been performed with a V-670 JASCO spectrophotometer, with a quartz vial ($l = 1\,cm$), recording the signal in the range $300 - 700\,nm$.

ICP-AES

The quantitative analysis of iron content was carried out with an atomic emission spectrometer coupled with a inductively coupled plasma torch (ICP-AES, Varian 720-ES) at the Department of Analytical Chemistry of the University of Florence from the group research by Prof. R. Udisti. To analyse iron content, powder samples were digested with $1\,mL$ of HNO_3, $1\,mL$ of HCl and $1\,mL$ of H_2O_2 and the solution is diluted to $20\,mL$ with the addition of Ge ($1\,ppm$) as an internal standard. The calibration standard was prepared for serial dilution of a commercial standard solution of Fe $1000\,mg/mL$. The wavelength used for the determination of Fe is $238{,}204\,nm$ while the line Ge was used at $209{,}426\,nm$. The operating conditions were optimized to obtain maximum signal strength.

8.4 Magnetic Characterization and SAR evaluation

Magnetic measurements were performed using a Quantum Design MPMS SQUID magnetometer operating in the $1{,}8\text{–}\,350\,K$ temperature range and with an applied field up to $50\,kOe$. Measurements were performed on pressed powder of SPION sample. All data were corrected for the diamagnetic contribution of the sample holder, and were normalized to the amount of magnetic material as evaluated from elemental analysis. Zero Field Cooled–Field Cooled (ZFC/FC) curves were obtained by measuring the temperature dependence of the magnetization applying a probe magnetic field ($50\ Oe$), after cooling the sample in the absence (ZFC) or in the presence (FC) of the field. A rough estimate of T_B value accuracy is given by the half interval between the temperatures of two subsequent acquisition points, *i.e.*, $2{,}5\ K$. The field dependence of the magnetic moment (*M vs. H*) was measured cycling the field between $\pm 50\ kOe$ at $2{,}5\ K$ and $300\ K$. The accuracy of H_C, M_R and M_S evaluation can be estimated as low as $3\ \%$.

The evaluation of Specific Absorption Rate (SAR) was performed through calorimetric measurements by recording temperature kinetics of samples exposed to an alternating magnetic field. SAR was evaluated both for water suspension of MNPs and MNP-HTt, than for agarose gel dispersion of MNPs in order to simulate the human tissue environment. Measurements were performed adapting a commercial setup, composed by a 6 kW Fives Celes power supply, a water-cooled induction coil and a series of variable capacitors ($420\ nF$ to $4{,}8\ \mu F$) for setting the required frequency. Such resonant RLC circuit is able to produce an alternating magnetic field in the range of $50\text{–}\ 400\ kHz$ and with amplitude up to $19{,}1\ kAm^{-1}$. The frequency and field amplitude values used in this work ($183\ kHz$, $17\ kAm^{-1}$) were chosen in order to operate under the physiological limit, $H\nu < 5 \cdot 10^9 A\, m^{-1} s^{-1}$, beyond which deleterious responses of living tissues are observed (Figure 8.1). The sample was placed in the middle of the induction coil, inside a polystyrene sample holder placed in a glass Dewar connected to a glycol thermal bath in order to isolate the sample bath from the thermal gradient of the coils and from the environment (Figure 8.2). The real amplitude of the magnetic field was determined by a AMF Life Systems high frequency probe. Measurements of the sample temperature were performed by an optical fiber thermometer connected to a digital temperature recorder (Fotemp). The SAR values were calculated using the equation $SAR = \frac{\Sigma_i m_i c_i}{m_{np}} \cdot \frac{\Delta T}{\Delta t}$, where ΔT is the temperature increase in the interval of time Δt, m_{np} is the total mass of Fe_3O_4, m_i is the mass in grams of the i-species and c_i is its specific heat. The sum is extended to all the i species involved in the heat exchange. Since the measurements are carried in non adiabatic conditions, the $\Delta T/\Delta t$ values were extrapolated for $t \approx 0$ from temperature kinetic curves, by considering the initial slope.

Figure 8.1: Power supply MP6-400 6kW®, Fives Celes Inc. and FoTemp optical fiber thermometer.

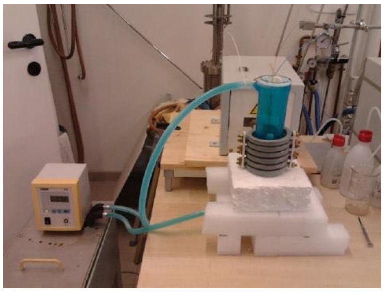

Figure 8.2: Detail of the Ethylene glycol thermostated system.

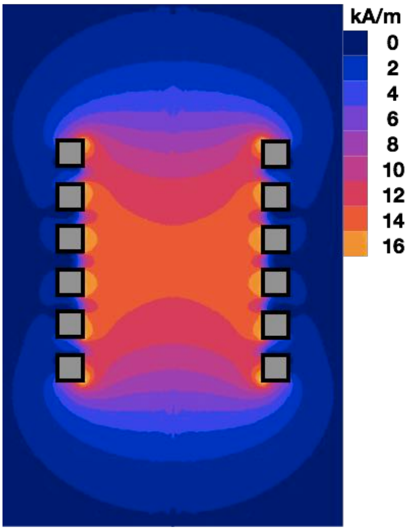

Figure 8.3: Field simulation output for the 6 windings coil, at 183 kHz of frequency and 16 kA/m of intensity.

8.5 *In vitro* biocompatibility and magnetic fluid hyperthermia experiments

In vitro tests to evaluate the biocompatibility of the MNP-HFt and the efficiency of the magnetic hyperthermic treatment were carried on Prostate cancer cell (PC3) and Breast cancer cell (MDA-MB-231), obtained from the American Type Culture Collection (Rockville, MD). The experimental design was based on previously published investigations analysing the in vitro hyperthermic efficacy of magnetic colloids[1], cells were cultured in high glucose Dulbecco's modified Eagle's medium (DMEM) supplemented with $10\,\%$ fetal bovine serum (FBS; Gibco, Invitrogen, Italy) in a $5\,\%$ CO_2 atmosphere at $37\,°C$. Medium contained $2\,mM$ L-glutamine, $100\,\frac{IU}{mL}$ penicillin, and $100\,\frac{\mu g}{mL}$streptomycin (Sigma, Germany). Cells were trypsinized with Tripsin-EDTA solution 1 for $5\,\mathrm{min}$ and then neutralized with culture medium. A total of $4 \cdot 10^5$ cells were suspended in $400\,\mu L$ of saline solution plus $5\,\%$ bovine serum albumine (BSA) to favour a homogeneous suspension and incubated for $60\,min$ at $37°C$ in the presence or in the absence of MNP-HFt $3 - 1 - 0{,}3\, mg/mL$. An oscillating magnetic field of $17{,}0\, kAm^{-1}$ and $183\, kHz$ was applied to the cell suspension for $1\, hour$. Alternatively, cell suspensions were centrifuged at $1400\, rpm$ for $5\, min$ to separate cells from the unbound MNP-HFt. Then cell pellets were re-suspended in $400\, \mu L$ of saline solution plus $5\, \%\, BSA$ and subjected to the oscillating magnetic field. For this purpose, cell samples were placed in the middle of the induction coil, inside a polystyrene sample holder placed in a glass Dewar connected to a glycol thermal bath in order to keep the system at $37\, °C$ and avoid thermal gradient of the coils and from the environment surroundings. After the exposure to the magnetic field, cells were centrifuged at $1400\, rpm$ for $5\, min$. Cells were washed twice in saline solution and suspended in $400\, \mu L$ of culture medium. A volume of $40\, \mu L$ of the cells suspension was used to perform Trypan Blue assay. Thirty microliters of the cells suspension was plated into $96\, wells$ culture plates and the sample was incubated in $5\, \%\, CO_2$ atmosphere at $37\, °C$; $48\, h$ after, MTT assay was performed.

Trypan Blue

Trypan Blue Assay, PC3 and MDAMB231 cells were diluted with $0{,}4\, \%$ trypan blue (Sigma-Aldrich, Italy), pipetted onto a Burker chamber and counted under a microscope at 40 magnifications. Live cells excluded the dye, whereas dead cells admitted the dye and consequently stained intensely with trypan blue. The number of viable cells for each experimental condition was counted.

MTT

MTT Assay. Cell viability was evaluated by the reduction of 3-(4,5-dimethylthiozol-2-yl)-2,5-diphenyltetrazolium bromide (MTT; Sigma-Aldrich, Italy). A total of $1\, mg/mL$ of MTT was added into each well and the samples were incubated for $30\ min$ at $37\ °C$. After washing, the formazan crystals were dissolved in $100\ \mu L$ of dimethyl sulfoxide. The absorbance was measured at $550\ nm$.

Fluorescence microscopy

Cell were incubated for $1\ h$ in DMEM in presence of HFn-Rhd in a petri plate, after removing the culture media congaing the fluorescent substance and replaced with fresh DMEM cell were analysed. The fluorescence microscope used was a Widefield: Leica AM6000, equipped with filter set N3 or N21 (for the rhodamine signal) and a Leica DFC350FX camera.

Confocal microscopy

Cell were incubated for 1 h in DMEM in presence of MNP-HFn-Rhd in a petri plate, after removing the culture media congaing the fluorescent substance and replaced with fresh DMEM celle were analysed. The confocal microscope used was a Leica SP2-AOBS, using a LASER exciter at $\lambda^* = 561\ nm$, taking images at different focal plane.

1. Fantechi, E. *et al.* A Smart Platform for Hyperthermia Application in Cancer Treatment : Cobalt-Doped Ferrite Nanoparticles Mineralized in Human Ferritin Cages. 4705–4719 (2014).

9. Acknowledgements

Devo ringraziare così tante persone che quasi non so da dove partire.
La prima persona che voglio ringraziare è il Dr. Claudio Sangregorio, che mi ha dato la possibilità di intraprendere questo cammino nel nano-mondo, senza il suo aiuto ed i suoi insegnamenti questa tesi non sarebbe mai potuta essere svolta. A seguire non posso che essere estremamente riconoscente e ringraziare tutti quei ricercatori che mi hanno aiutato fornendo il loro supporto, il loro tempo e i materiali per la realizzazione di questo lavoro: il Dr. Pierpalo Ceci e la Dr. Elisabetta Falvo dell'università la Sapienza di Roma, che mi hanno fornito le proteine; la Dr. Barbara Tenci e il Dr. Lorenzo di Cesare Mannelli dell'università degli Studi di Firenze, per l'enorme lavoro svolto, solo grazie alla loro disponibilità è stato possibile effettuare la sperimentazione *in vitro*; la Prof.ssa Zulmira Lacava e la Dr. Danyelle Ferreira che hanno realizzato la sperimentazione *in vivo*.
Voglio quindi ringraziare i compagni che mi sono stati vicino in questi 4 anni di laboratorio: Martin, Michele e Claudia, il confronto con voi è stato prezioso per la mia crescita, anche personale, sentirò enormemente la mancanza della vostra amicizia. Un grazie speciale al Dr. Matteo Mannini che mi ha insegnato molto più di quanto non mi sarei aspettato, e al Prof. Andrea Caneschi che mi ha spronato al momento giusto. Un grazie anche a tutti gli altri componenti del LAMM: la Prof.ssa Roberta Sessoli, il Prof. Lorenzo Sorace, Il Prof. Federico Totti, Pine, Pone, Beppe, Poggio, Giulia, Marie-Emmanuelle, Irene, Brunetto, Matteo B., Matteo A., Donata, Pamela e Beatrice.

Ringrazio poi i miei genitori e la mia sorellina *in primis*, e il resto della mia grande Famiglia TUTTA che mi è sempre stata vicina e mi ha supportato sempre e comunque, senza il loro sostegno mi sarei perso combinando poco o nulla.

Un grazie anche ai miei amici di una vita, con i quali ho condiviso tanti momenti preziosi e che mi hanno aiutato a crescere: Checco, Leo, Lore, Marco, il Don, il Gentili, Faggio, Beppe la SFL-HateSquad, gli ex SCOUT e anche a tutti coloro che ho imparato a conoscere più di recente, B-team annessi e connessi.

Ultima ma solo perché la più importante voglio ringraziare la mia futura moglie: Diletta. Grazie per essermi stata sempre vicina, per il tuo costante supporto e amore che ha allietato anche i giorni più duri quando tutto sembrava non avere un senso, come potrei essere arrivato dove sono senza di te?